Bachelor's thesis in physics

Faculty of Mathematics, Computer Science and Natural Sciences at RWTH Aachen University

A study of hadronic tau lepton decays in Model Unspecific Search in CMS

submitted by

Patrick Hartmut Horst Kersten

in October 2023

written at
Physics Institute III A

1st Examiner:	Univ.-Prof. Dr. rer. nat. Thomas Hebbeker
2nd Examiner:	Univ.-Prof. Dr. rer. nat. Martin Erdmann

Contents

Abstract

The Model Unspecific Search in CMS (*MUSiC*) is a general approach to search for new physics beyond the Standard Model in CMS data of proton-proton collisions at LHC. This thesis studies hadronic tau lepton decays in the CMS data from 2018 at a centre-of-mass energy of $\sqrt{s} = 13\,\text{TeV}$. Collision events are sorted to several event classes depending on their final state multiplicities. In contrast to dedicated analyses, the goal is to investigate all possible final states. The observed data is compared to Monte Carlo simulations of Standard Model processes in different kinematic variables and a statistical test performed to quantify possible deviations. In former *MUSiC* analyses tau leptons have not been regarded but new reconstruction algorithms deliver a higher identification efficiency and low misidentification rate. This gives the opportunity of reasonably analyzing taus in this approach. In the general investigation no significant deviations are found in event classes containing taus. The most deviating event classes are regarded further by looking at the kinematic distributions. A sensitivity study is performed to asses the capability of finding new physics, regarding a theory beyond the Standard Model. Strong signals can be seen, but without a significant deviation. Weaker signals are not detectable in this approach.

1 Standard Model

The fundamental particles and interactions of the Universe are described by the Standard Model of particle physics (SM).[1] It consists of matter particles as well as interaction particles, that are named fermions and bosons after their spins and the resulting static behaviour, and explains the occurring forces. A basic illustration of the particles in the SM is shown in Fig. 1.

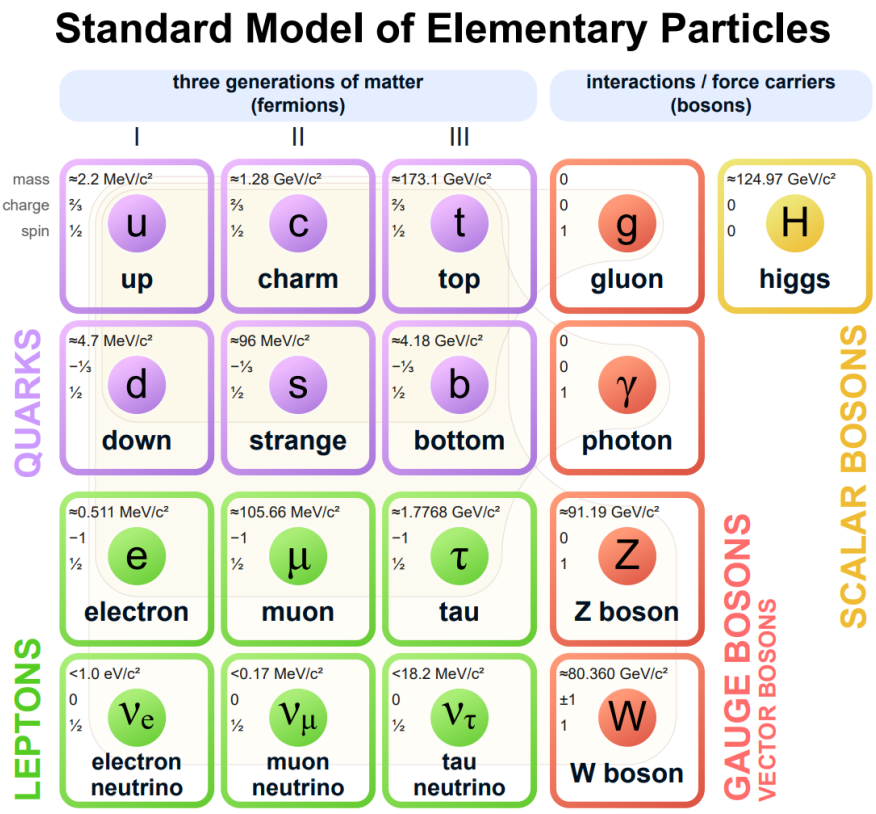

Figure 1: Illustration of the Standard Model of Particle Physics [51] - On the left the matter particles are shown: quarks in purple and leptons in green. They are ordered in the corresponding generation. The gauge bosons are shown in red and the last interaction boson, the Higgs boson, in yellow. Light grey lines indicate, which particles interact with each other.

[1] This analysis uses natural units. Consequently, the speed of light c and Planck's constant $\hbar$ are $c = \hbar = 1$. Moreover, the elementary charge e is regarded to be $e = 1.602 \times 10^{-19}$ C. This leads to the following definition of electron volts $1\,\mathrm{eV} = e \cdot 1\,\mathrm{V} = 1.602 \times 10^{-19}$ J. Hence, unlike in SI-units 1 eV is equally used for the units of mass m, momentum p and energy E.

1.1 Interactions

Particles can interact via forces, while force and interaction is used synonymously. Four fundamental forces has been observed, namely electromagnetic, weak and strong force as well as gravitation, but the latter is not included in the SM. So it consists of three basic forces, which are exchanged via interaction particles, the gauge bosons that have a spin of $S = 1$ and hence their behaviour is described by Bose-Einstein statistics [28].

1.1.1 Strong force

Every particle that has a so-called color charge can participate in processes of the strong force. Three different kinds of this charge exist, red, blue and green, as well as an corresponding anticolor. This is described in the theory of quantum chromodynamics (QCD) [24]. The related boson is the gluon (g), which carries a combination of color and anticolor itself. Subsequently, there are eight gluons with a different charge combination. Because of their charges they can not only transfer the strong force between particles but take part in the interaction also and even interact with each other [24]. The range of this force is restricted to 10^{-15} m [28], which is in the order of magnitude of the size of a proton. Every color-charged particle is subjected to a phenomenon called Confinement, in which particles cannot appear alone, but must be bounded to others in a neutral color state [9]. The corresponding potential can phenomenologically approximated by:

$$V(r) = -\frac{4\alpha_s}{r} + br + c \tag{1}$$

with different parameters b and c as well as the coupling constant (see 1.1.2) α_s and the distance r. Fig. 2 shows the potential for different parameters.

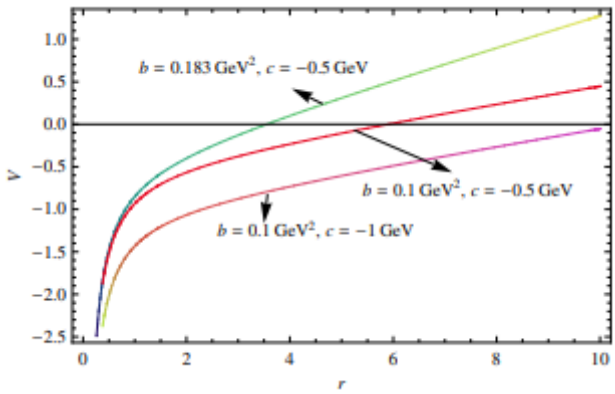

Figure 2: Variation of the potential $V(r)$ by changing the parameters [9].

Ergo, this especially applies to gluons. This force is the strongest of the interactions and it naturally appears in atomic nuclei, because it is the force that attracts the nucleons [28, 8].

1.1.2 Electromagnetic force

The photon (γ) is the gauge boson of the electromagnetic force. It does not carry an electric charge and hence it just mediates the interaction, but does not participate. Further this interaction applies to all particles that have an electric charge [24]. In contrast to the strong interaction, there are two types of charges, positive and negative, in which opposing charges attract and same ones repel each other. The theoretical background is quantum electrodynamics (QED) [24]. This force appears in Nature as the underlying of the stable bounds of atoms. Moreover, the coupling constant, that quantifies the strength of the fundamental force, of the electromagnetic interaction is smaller than the strong constant, which results in being a weaker force [8]. The range of a photon and consequently this force is infinite, but the potential decreases with growing distance like $\frac{1}{r}$ [28]. So particles are not subjected to a confinement within the electromagnetic interaction.

1.1.3 Weak force

The remaining interaction is the weak force. Thus it is the weakest of the interactions, as the coupling constant is about a millionth of the strong constant [28]. All particles that have masses can participate in weak processes. Three gauge boson transfer the weak force, the Z boson (Z^0) with a mass of $m_Z = 91\,\text{GeV}$ as well as an electrically charged W boson ($W^\pm$) that are $m_w = 80\,\text{GeV}$ heavy. Regarding that, only processes that satisfy the conservation of electric charge can happen. Additionaly, these are the only force-carrying bosons, which have masses. Because of that, the Z and W bosons quickly ($\approx 10^{-25}\,\text{s}$ [47]) decay into other particles and it limits the range of the weak force to about $10^{-17}\,\text{m}$ [36].

1.1.4 Electroweak unification

Ultimately, for processes on high energy levels the electromagnetic and weak forces appear to be the same type of interaction. This has been proposed in 1968 and therefore those forces are united to one phenomenon, the electroweak force. The theory behind has foreseen the existence of neutral currents, basically the Z boson, so its discovery in 1973 also verified the unification [36].

1.1.5 Higgs mechanism

The Higgs mechanism completes the SM concerning the interactions. It has been proposed by Peter Higgs in the 1960s [40, 39] and François Englert has published similar results at the same time [32]. Contrary to the other gauge bosons, the Higgs boson (H^0) has a spin of $S = 0$ and it does not carry a force. Instead the coupling of a particle and the Higgs boson provides mass to particles within the SM. The process of spontaneous breaking of the symmetry provides the explanation [27]. In 2012 a boson with a mass of $m_H = 125\,\text{GeV}$ has

been discovered at the LHC [15, 19] that has turned out to be identified as the Higgs boson.

1.2 Matter particles

The SM comprises of twelve matter particles as well as twelve corresponding anti-particles always having the opposite electric charge. These particles are called fermions because of having a spin of $S = \frac{1}{2}$ and following the Fermi-Dirac statistics. Fermions are divided into quarks (q) and leptons (ℓ) regarding the forces they are subjected to, while simultaneously being organized into three generations [60]. Ordinary matter is made of particles of the first generation. The other particles, being more massive, are unstable and decay to the lighter particles ending up in first generation. Lastly, all particles participate in weak interaction processes [26, 28, 8]

1.2.1 Quarks

Quarks are fermions, that carry color charges. Hence they are the only matter particles that participate in the strong interaction. Coming back to Confinement mentioned in Sec. 1.1, quarks cannot be found unbounded. After being produced they immediately form composite particles of at least two quarks, which are called hadrons. In order to observe quarks high energy levels are essential because to resolve small lengths high energies are required [28]. Every generation of fermions consists of two quarks, where one has an electric charge of $q^+ = \frac{2}{3}e$ and the other a charge of $q^- = -\frac{1}{3}e$. Hence, there are six quarks, that are called up (u) and down (d), charm (c) and strange (s) as well as top (t) and bottom (b), sorted in correct generation and charge order. Hadrons are divided into mesons, which consist of a quark-antiquark pair, and baryons that are particles made of three quarks. Ordinary matter consists of protons and neutrons, which are baryons. Two of the first discovered mesons are the pion ($\pi^{\pm}, \pi^0$) and the kaon ($K^{\pm}, K^0$). The pion emerges of different combinations of up- and down-quarks and the kaon of a strange-quark and an up- or down-quark. These meson constituents are shown in Tab. 1. The quarks in hadrons are composited in a way that only integer electric charges arise. Moreover, hadrons are color charge neutral [36, 61].

Meson	π^+	π^-	π^0	K^+	K^-	K^0	$\bar{K}^0$
Constituent quarks	$u\bar{d}$	$\bar{u}d$	$u\bar{u}, d\bar{d}$	$u\bar{s}$	$\bar{u}s$	$d\bar{s}$	$\bar{d}s$

Table 1: This Table shows the composite quarks of the two mentioned mesons for different charges. π^0 is a quantum superposition of up-antiup and down-antidown [47]

1.2.2 Leptons

To complete the SM, the generations of fermions also include two leptons each, one negatively charged particle with $q_{\ell^-} = -e$ which participates in electromagnetic and weak interaction

as well as an corresponding neutral one. Leptons do not have a color charge, so the neutral particle, called neutrino (ν), can only interact via weak force. The leptons are called electron (e^-) and electron neutrino (ν_e), muon (μ^-) and muon neutrino (ν_μ) along with tau (τ^-) and tau neutrino (ν_τ) [28]. The discovery of the electron by J.J. Thomson in 1897 [57] was the first evidence of a subatomic particle and the first known particle of todays' SM. While the mass of the charged leptons increases with the generation neutrinos are regarded to be massles in the SM. This leads to problems as described in Sec. 1.3.2.

1.2.3 Tau lepton

The tau lepton is the third of the non-neutrino leptons and the heaviest lepton with a mass of $m_\tau = 1776.86(12)\,\mathrm{MeV}$. Because of that, it has to be artificially produced in particle accelerators at high energies. This has happened first at the *SPEAR* e^+e^- storage ring in 1975 by the Team of M.L. Perl [36, 52]. Another consequence of its high mass is that its average lifetime is $\tau_{\tau^-} = 2.903(5) \times 10^{-13}\,\mathrm{s}$. Not only, taus can decay to the other charged leptons but their mass also allows them to decay to hadrons [36, 61], which is then denoted as τ_ℓ or τ_h. The most probable decays are listed in Tab. 2.

decay mode	frequency in %
$\mu^-\bar{\nu}_\mu\nu_\tau$	17.4
$e^-\bar{\nu}_e\nu_\tau$	17.8
$\pi^-\nu_\tau$	10.8
$\pi^-\pi^0\nu_\tau$	25.5
$\pi^-2\pi^0\nu_\tau$ (ex. K^0)	9.3
$\pi^-\pi^-\pi^+\nu_\tau$ (ex. K^0, ω)	9.0
$\pi^-\pi^-\pi^+\pi^0\nu_\tau$ (ex. K^0, ω)	2.7
$\pi^-\omega\nu_\tau$	1.9
$\pi^-3\pi^0\nu_\tau$ (ex. K^0)	1.0
total leptonic	35.2
total hadronic	64.8

Table 2: The most probable branching fractions of the tau lepton and the total probability of hadronic and leptonic tau decays. The ω meson is a different superposition of the same quarks like π^0 (Sec. 1.2.1) [47].

1.3 Shortcomings of the SM

The SM is a well tested theory [52, 19, 22]. Historically, it has not only explained the already discovered particles, but also has predicted the existence of later observed particles like the Higgs boson or the top quark. But gravitation is not included in the SM and other experimental findings also show that it cannot describe Nature satisfactory [60]. Moreover, recent precise measurements of the magnetic moment of the muon show disagreement with the SM expectation [38, 43]. This section concerns two exemplary phenomena that are not

explained by the SM.

1.3.1 Dark matter

Cosmology, a sub-discipline of physics that deals with the exploration of the Universe, has open questions also regarding the SM. There are among others two phenomena that suggest the existence of so-called dark matter [60] and an exemplary image is shown in Fig. 3. First, velocity distributions of stars in other galaxies do not fit to the amount of ordinary detectable, "visible", matter. Stars in larger distances to the central mass move faster than expected, hence an significant amount of matter that has not been observed yet is postulated [49]. Secondly, due to General Relativity ([31]), light can be distracted by gravity. This has been proven by studies of stars that are close to the sun in the starry sky. Now, this effect named as gravitational lens is observed in places without enough visible matter [34]. To conclude, dark matter cannot be explained by the SM because it expects particles to interact with light and hence become visible.

Figure 3: Image of the galaxy cluster *CL 0024+17*. It has been derived from light distractions because of the gravity in this galaxy (Gravitational Lensing). A circular structure is visible related to dark matter. A suggestion is that the dark matter has been produced in a collision of two clusters [48]. Credits: NASA, ESA, M.J. Jee and H. Ford (Johns Hopkins University)

1.3.2 Neutrino oscillations

Neutrinos are particles with rare interactions. As mentioned before, they only participate in weak force processes. Hence, the discovery of neutrino oscillations by the Super-Kamiokande Collaboration in 1998 [35] that resulted in the Nobel Prize 2015 "for the discovery of neutrino oscillations, which shows that neutrinos have mass" [55], has been a break-trough in particle physics. The phenomenon describes flavor oscillations of the three neutrino types, so e.g. an electron neutrino spontaneously converting to a muon neutrino and the probability for such a process depends on the squared mass difference Δm^2 of the involved neutrinos [35]. This is in contrast to the SM (see Sec. 1.2.2). In the end, it "is a first particle physics evidence of a new beyond the SM physics"[5].

2 Beyond Standard Model

As stated before the SM cannot explain certain observations. Thus, there are several new theories developed to describe these phenomena, which are labeled as 'Beyond Standard Model physics' (BSM) [60]. Accordingly, various research groups try to experimentally observe BSM processes.
Previous *MUSiC* analyses investigated its sensitivity on a heavy charged gauge boson (W') or processes with a sphaleron [42]. Hence this thesis will focus on composite leptons, obviously composite tau leptons.

2.1 Excited Taus

To solve why the generations of fermions and their order of mass exist, one hypothesis is that the particles of the SM are not fundamental but have an inner structure of smaller particles [58]. This is called compositeness model of leptons [50]. This theory assumes leptons to be built up of a fundamental particle named preon [37, 30], which has not been experimentally observed yet. Consequently, leptons could exists in an excited state. The following section treats this concept for tau leptons as presented in [3].

A certain hypothetical process in that an excited tau (τ^*) could be produced, is the interaction of two quarks as shown in Fig. 4. Through contact interaction they could exchange preons and convert to a pair of taus, in which one tau is excited and finally decays to a normal tau by emitting a photon. Hence, one can expect a resulting final state to contain two tau leptons and one photon. Characteristic quantities of this process are the mass of the excited tau as well as Λ, which is a scale factor to quantify the compositeness.

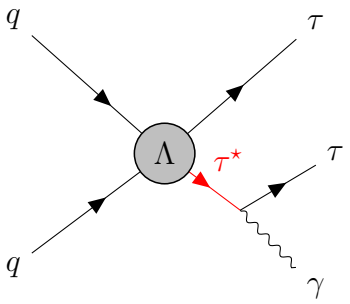

Figure 4: Feynman diagram of a potential excited tau production

3 Experiment

Fig. 5 shows an overview of the history of hadron colliders. As previously explained, high energies are necessary to not only observe processes described by the SM, but also to find new physics. This is because the production of particles requires higher energies the more massive the particles are. In addition, higher energetic particles can resolve smaller structures because of their de Broglie's wavelength [25]. Accordingly, one of the largest experiments ever, the Large Hadron Collider (LHC), has been built.

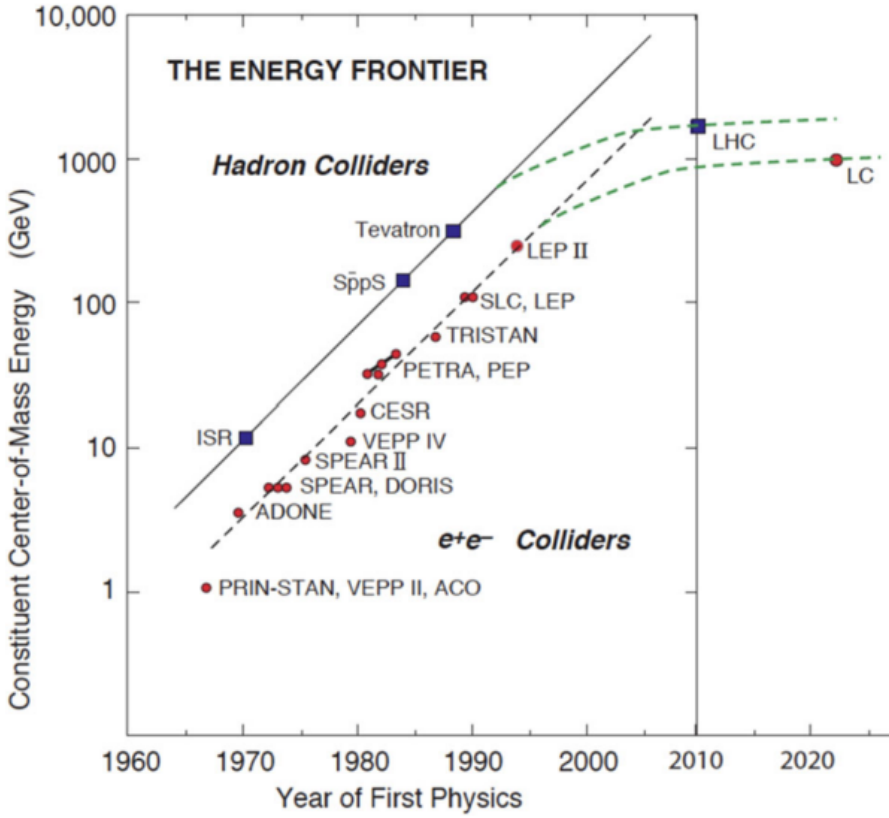

Figure 5: This figure presents how the center-of-mass energy of collider experiments has increased over time [38]. The tau lepton was discovered at SPEAR in 1975 [52]. In 1995 the top quark has been observed for the first time in the D0 experiment at Tevatron [22]. The Higgs boson has been discovered in 2012 at the LHC [19, 15].

3.1 Large Hadron Collider

The LHC is a particle accelerator that has been built in the already existing 26.7 km tunnel of the LEP experiment [44]. It is located in the Geneva border of Switzerland and France up to 170 m under the ground [33]. Three operating modes enable to either collide protons

to protons, lead nuclei to lead nuclei or protons to lead nuclei in high center-of-mass energies. The limit for proton-proton collisions is $\sqrt{s} = 14\,\text{TeV}$ [6]. There are more than 9000 superconducting magnets of different types to reach this energy regime. The most demanding aspect are 1232 superconducting dipoles that have to deliver reliably a magnetic field of about 8.33 T which is about 10^5 times the magnetic field of the Earth. An accelerated proton filling consists of 2808 bunches with 105 billion protons each [10]. On average, at the design luminosity of $10^{34}\,\text{cm}^{-2}\text{s}^{-1}$ there are 20 collisions per crossing of two bunches, in the end about 1000 charged particles are produced per interaction every 25 ns. To minimize background effects, vacuum is required in the beam pipes, which have a diameter of 6 cm. Hence, the room temperature parts of the system are at pressure of 10^{-8} to 10^{-9} Pa. That is about a hundred times less than the pressure on the Moon's surface [10].

The whole acceleration complex is displayed in Fig. 6. Hydrogen are ionized and injected

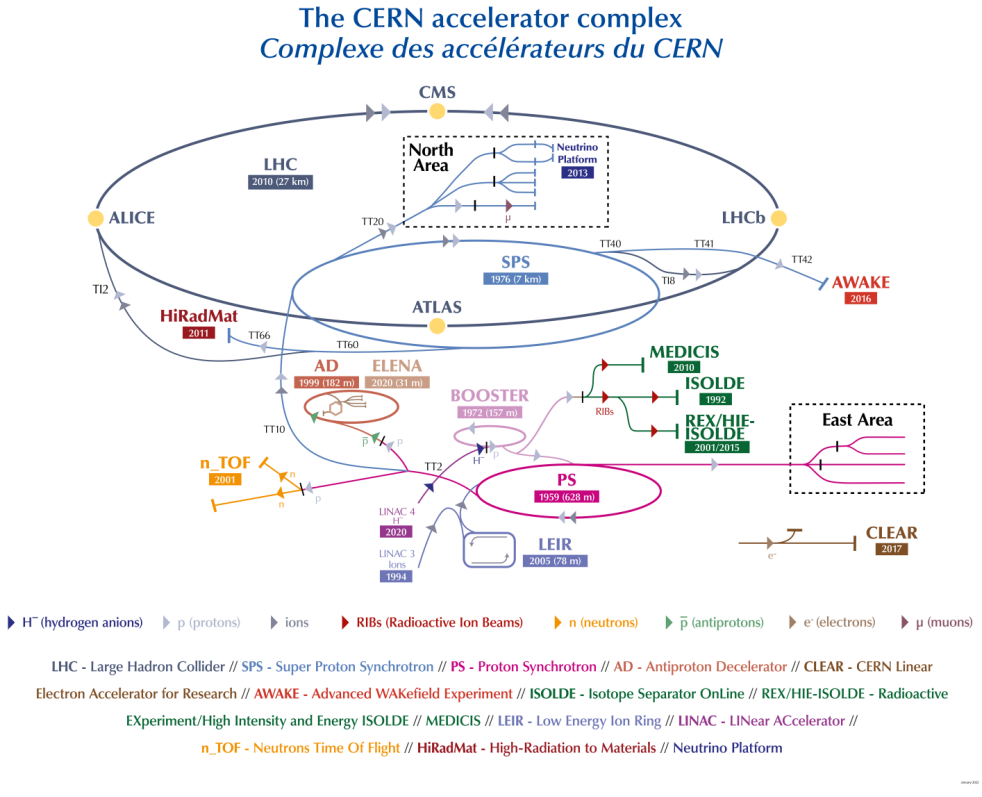

Figure 6: The LHC acceleration complex [45]. This is the 2022 layout.

to the PS Booster already carrying an energy of about 50 MeV from Linac2. The booster accelerates the protons to 1.4 GeV and afterwards provides them to the Proton Synchrotron (PS), which accelerates the beam further to 25 GeV [7]. In the next step, the protons reach the Super Proton Synchrotron (SPS) and their energies are increased up to 450 GeV. Only then, beams are transferred to the LHC (in both directions) and are accelerated for 20 min to 6.5 TeV each. In the usual operating conditions, a certain beam fill stays for hours inside the LHC [7].

Ultimately, to observe the events there are four points of collision, so-called interaction points, with corresponding experiments:

- ALICE (A Large Ion Collider Experiment):
  The ALICE experiment is specialized on observing heavy ion collisions [14].

- ATLAS:
  ATLAS is a general purpose detector for proton-proton collisions [1].

- CMS (Compact Muon Solenoid):
  CMS has the same purpose as ATLAS but is also capable of studying heavy ion collisions [4].

- LHCb (Large Hadron Collider beauty):
  The LHCb detector has been designed to study decays of B mesons and their properties [46].

In the end, the supervision of events at all detectors results in an amount of data of about 15 PB per year which is about 15 million gigabytes. The storage and data analysis is performed via the Worldwide LHC Computing Grid (WLCG) [6].

3.2 Compact Muon Solenoid

CMS is an experiment with several purposes located about 100 m underground near the village of Cessy in France. The cylindrical detector is divided into a barrel and endcap region and has a length of 21.6 m as well as a diameter of 14.6 m. The eponymous 6-m-diameter solenoid is designed to deliver a magnetic field of 3.8 T. CMS consists of various detector types focused on different particle detection [13]. The whole detector is shown in Fig. 7.

To perform the data analysis, the detector needs a coordinate system. Its origin is in the interaction point of CMS. The x-axis points radially towards the center of the LHC and the y-axis points upwards to the Earth's surface. Lastly, the z-axis points in the beam direction counterclockwise [29]. While the azimuthal angle ϕ is measured in the xy-plane starting from the x-axis, the polar angle θ is measured from the beam direction. Due to its shape, it is practical to use polar coordinates with r being the distance in xy-plane and the angle ϕ. To complete, usually the pseudorapidity $\eta = -\ln \tan(\theta/2)$ is used instead of the second angle [53, 13], because for high-energetic particles ($E \gg m$) differences $\Delta\eta$ are Lorentz invariant under a boost in z-direction and it approximates the particle rapidity in the high energy

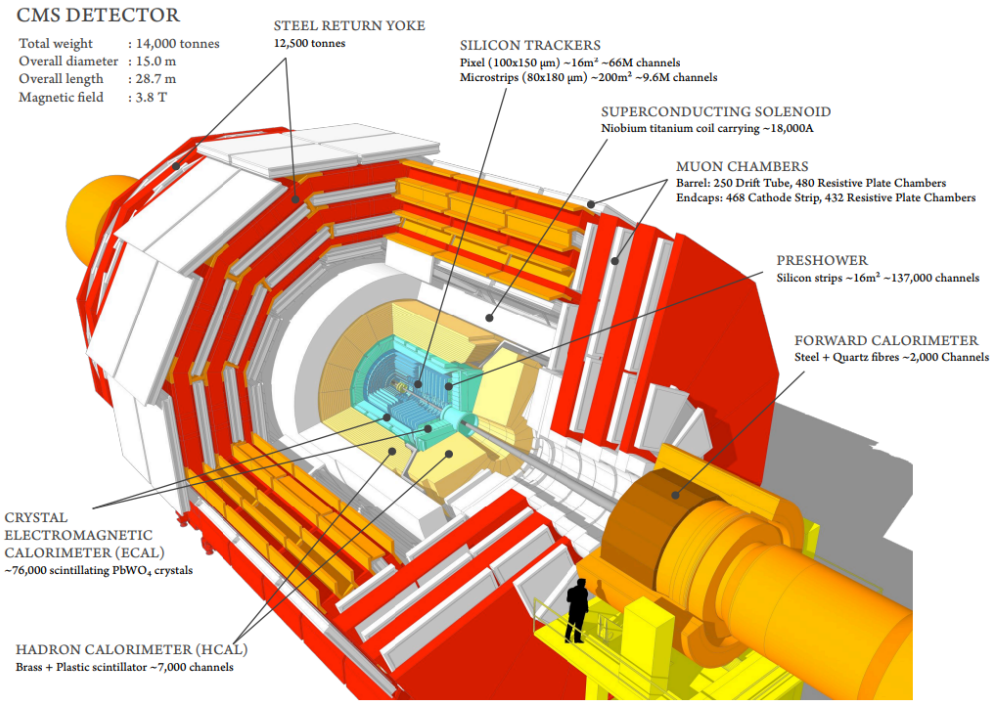

Figure 7: The CMS detector [54]. The constituent detectors are described in the following section.

limit. In this way, the lorentz-invariant angular distance ΔR can be calculated as:

$$\Delta R = \sqrt{\Delta\eta^2 + \Delta\phi^2} \tag{2}$$

There are many requirements to the detectors in terms of acquiring the data. Because of the short interval between collisions CMS allignes its clock with the LHC bunch crossings, in order to keep track of the signal timing. Of course, the characteristic quantities, such as energy, momentum and timing have to be determined with good resolution. To achieve these goals, a large number of detector channels with good time resolution is essential. Further, the particle collisions emit radiation, so the hardware has to be robust and radiation-hard. The whole detection system is shown in an exemplary sketch in Fig. 8 and each subsystem is presented in the following.

3.2.1 Tracker system

The Tracker System (TS) consists of silicon detectors that satisfy the mentioned requirements. It is the first detector directly surrounding the beam pipes, its length is about 5.8 m and its diameter is 2.5 m and the solenoid's homogeneous magnetic field covers the whole TS. There are two types of devices in the system, 1440 pixel detectors as well as 15 148

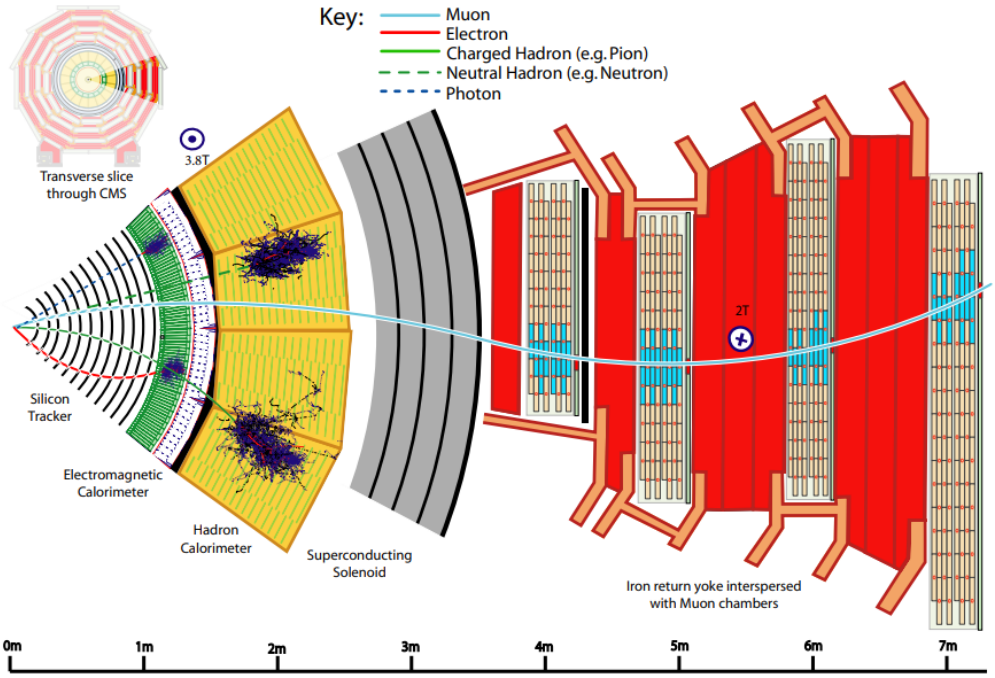

Figure 8: A sketch of the detection principle of CMS [20]. It is visible how the electrically charged particles are forced to circular paths by the solenoid's magnetic field. Neutral particles have a straight path. Photons and electrons are detected in the electromagnetic calorimeter. Neutral Hadrons reach the hadronic calorimeter on a straight path and charged hadrons on a circular path. Only muons traverse the first detectors and are finally observed in the muon chambers.

silicon strips. The size of one pixel cell is about $100 \times 150\,\mu\text{m}^2$ and it precisely measures the r, ϕ and z coordinate which reconstructs secondary vertices. Lastly, the pixel system can detect in the range of $|\eta| < 2.5$ [13]. The layout of it is shown in Fig. 9. The material of the strip trackers is n doped silicon and are depending on their position 320 to 500 μm thick. To cover all regions, the sensors are formed in 15 different geometries. The active area of all strip trackers is in total $198\,\text{m}^2$ [13].

3.2.2 Electromagnetic calorimeter

The electromagnetic calorimeter (ECAL) is a sensor for particles that interact via the electromagnet force, electrons and photons as well as charged hadrons. The purpose of calorimeters is to determine the amount energy deposited in the detector. ECAL is the second detector from the beam pipe to the outer region of CMS and consists of 61 200 lead tungstate crystals in the barrel region ($|\eta| < 1.479$) and 7324 in each endcap ($1.479 < |\eta| < 3.0$). So, when a detectable object passes the ECAL it deposits its energy and the crystals scintillate.[2] The created photons, which are proportional to the absorbed energy, are observed by Avalanche photodiodes in the barrel part and vacuum phototriodes in the endcaps. For example, this

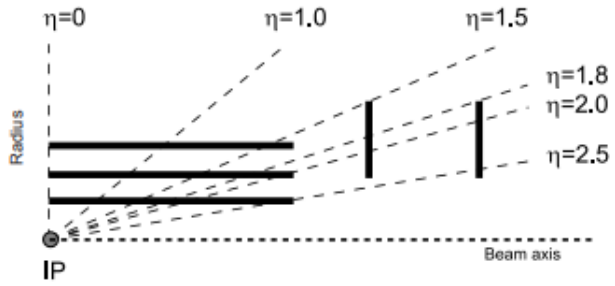

Figure 9: Geometrical layout of the pixel detectors [13]

setup is especially capable of monitoring two photons that are created in a Higgs decay [13].

3.2.3 Hadron calorimeter

The hadron calorimeter (HCAL) is designed to measure the energy of particles interacting via strong force. It is divided in four subsystems: the barrel (HB), endcap (HE), outer (HO) and forward (HF) calorimeters, where the first two are sampling calorimeters inside the cryostat of the solenoid that have brass as an absorbing material and a scintillator as active material [11]. Layers of plastic scintillator outside the cryostat comprise the HO [16]. The HF is made of quartz fibers and steel and it can detect particles even up to $|\eta| < 5.19$ by measuring Cherenkov light of secondary charged particles traversing the fibers [13].

3.2.4 Superconducting Solenoid

The name-providing and already mentioned superconducting solenoid of CMS has a length of 12.5 m and can store an amount of energy up to 2.6 GJ when operated with a current of 19.5 kA. It usually provides a magnetic field of 3.8 T. The superconduction is achieved by cooling the Niobium-titanium wires down to 4.5 K. To return the magnetic flux, there is a 10 000 t yoke made of iron. This apparatus is central to force charged particles on a circular paths and it allows other detectors to measure the momentum [13, 53, 2].

3.2.5 Muon system

The last, also eponymous, feature of CMS is the muon system. It is designed to reconstruct momentum and charge of muons at any. The system is located outside the solenoid and reaches a pseudorapidity of $|\eta| < 2.4$. In order to detect muons, it consists of gas ionization chambers [13, 12, 53]. Their operating principle is detection of electron avalanches, that are produced by accelerated electrons arising from ionization due to the passage of an charged particle, here muons. In order to have suitable detectors at any location of the system, there are three different types of sensor chambers. Drift Tubes are installed in the barrel region,

Cathode Strip Chambers are located in the endcap region. To complement the other systems resistive Plate Chambers are along them and provide better time resolution [13].

3.2.6 Trigger and Data Acquisition

As mentioned before (Sec. 3.1), proton-proton collisions happen every 25 ns, which leads to a very high amount of data that has to be reduced before storage. Hence there is a triggering system that acts as a prefilter.

The first stage of triggering system is the Level-1 (L1) trigger system. It is an hardware based trigger made of programmable electronics. It rejects low-energetic events with information of the calorimeters as well as the muon system and doing so, it decreases the collision rate of about 16 MHz to a data rate of 100 kHz which is the limit of the read out system [59, 2]. The second stage is the High Level Trigger (HLT), which is a software based filter.
L1 analyzes the bunch crossings and launches a signal of L1 Accept if the event shall be further investigated. When a subsystem receives the signal their information is storaged and provided to DAQ. Then an event is approved by HLT, which reads the data of all the subsystems online from DAQ [56]. This procedure reduces the data rate to 1 kHz. It is performed on a farm of commercial computers including over 13 000 CPU's and afterwards stored for further analysis (see Sec. 3.1 WLCG). Further, CMS uses a reconstruction algorithm called Particle Flow (PF), that identifies particles, like taus, jets or missing tranverse energy, individually using the correlated information of all subdetectors of CMS. The usage of PF improves the energy resolution of trigger objects and their identification efficiency [59].

4 Model Unspecific Search in CMS

The Model Unspecific Search in CMS (*MUSiC*) is a general approach for searching new physics in colllider data. The MUSiC algorithm searches the CMS data for deviations of the SM predictions not in a given final state, but in almost all possible final states unbiased of particular BSM theories. This ansatz is a trade off between the higher sensitivity of a model specific search and the broad phase-space searched by *MUSiC*. The SM prediction is represented by a set of Monte-Carlo-Simulations (MC) that imitate the physics behaviour of particles according to the SM. Dedicated analyses are more sensitive to signals but only search in well-defined regions. Here, a broad region is examined which results in less sensitivity, but the *MUSiC* analysis reduces the possibility of just overlooking new physics phenomena. In the following sections the search strategy is presented.
The *MUSiC* analysis for the LHC Run-2 Ultralegacy (UL) dataset, which is data from 2016 to 2018, is currently evolving. This thesis is part of this process and only regards data from 2018 with a center of mass energy of $\sqrt{s} = 13\,\text{TeV}$ and a corresponding luminosity of $\mathcal{L} = 59.8\,\text{fb}^{-1}$.

4.1 Preprocessing

The CMS data is distributed via data streams and not the whole recorded data is provided to every applicant because of storage reasons. *MUSiC* uses data from the streams associated to the used triggers. But the raw CMS data is not applicable for the *MUSiC* algorithm, so it has to be preprocessed. The emerging data is stored for further analysis.
A list of all used MC samples for the SM prediction is documented in Appendix F. MC events are weighted as follows. The weight regarding the cross section and luminosity is computed by

$$\alpha_{lumi} = \frac{k \cdot \sigma \cdot \int \mathcal{L} \mathrm{d}t}{N_{MC}} \tag{3}$$

to match with the expected data count. Pileup (PU) describes the fact that high luminosity bunch crossings can generate numerous proton-proton interactions which are mixed within the same readout window by the detector. The distribution of the MC pileup has to fit to the measured data pileup. Therefore a weight factor α_{PU} is regarded. MC processes can also provide a negative contribution to the complete MC yield, which can be implement by passing a generator weight factor α_{gen}. So the total MC weight is computed by

$$\alpha_{MC} = \alpha_{lumi} \cdot \alpha_{PU} \cdot \alpha_{gen}. \tag{4}$$

For every recorded event, the content in terms of physics objects has to be reconstructed. *MUSiC* distinguishes between muons, electrons, taus (τ_h), photons, jets, b-tagged jets and missing transverse momentum (p_T^{miss}). Tight object selection criteria are applied o ensure a low misidentification rate of the reconstructed objects, but keep a reasoned selection efficiency, as shown in Tab. 3. This is corresponding to previous *MUSiC* analyses. The criteria

Object	p_T [GeV]	Pseudorapidity
Muon (μ)	> 25	$\lvert\eta\rvert < 2.4$
Electron (e)	> 25	$0 < \lvert\eta\rvert < 1.44$ or $1.57 < \lvert\eta\rvert < 2.50$
Tau (τ_h)	> 25	$\lvert\eta\rvert < 2.1$
Photon (γ)	> 25	$\lvert\eta\rvert < 1.44$
Jet	> 50	$\lvert\eta\rvert < 2.4$
b-tagged Jet	> 50	$\lvert\eta\rvert < 2.4$
Missing transverse momentum (p_T^{miss})	> 100	—

Table 3: Object selection criteria

Trigger	Trigger level requirement	Analysis requirement
Single-muon trigger	1μ with $p_T > 50\,\text{GeV}$	$\geq 1\mu$ with $p_T > 53\,\text{GeV}$
Single-electron trigger	$1e$ with $p_T > 115\,\text{GeV}$	$\geq 1e$ with $p_T > 120\,\text{GeV}$
Dimuon trigger	1μ with $p_T > 17\,\text{GeV}$	$\geq 2\mu$, each with $p_T > 21\,\text{GeV}$
	second μ with $p_T > 8\,\text{GeV}$	
Dielectron trigger	$2e$, each with $p_T > 25\,\text{GeV}$	$\geq 2e$, each with $p_T > 40\,\text{GeV}$
Single-photon trigger	1γ with $p_T > 200\,\text{GeV}$	$\geq 1\gamma$ with $p_T > 225\,\text{GeV}$

Table 4: Online and offline trigger criteria

for τ_h selection are also listed there.

Moreover, every event to be further analyzed has to fulfill one of the single-lepton, dilepton or single-photo triggers as listed in Tab. 4. A triggering object has to have a higher momentum than the documented threshold in the second column. Afterwards a slightly higher p_T is required per object to be regarded in the analysis. These thresholds are applied to maximize the efficiency but still ensure that objects are selected with a high enough statistics.

When physical objects in the detectors are too close, this can lead to misidentified objects in the analysis. To avoid systematic uncertainties arising from that, particles that are to close to others are cleared following a clear hierarchy. For example, if an electron is closer than $\Delta R < 0.4$ to a muon, the electron will be removed and just the muon will be analyzed. The clearing criteria are listed in Tab. 5

Hadronic Tau reconstruction
In order to identify hadronic tau decays the hadron-plus-strip algorithm is used [21, 17]. First, regions that contain hadronic jets, reconstructed by the PF algorithm, are defined as seed region with the goal to reconstruct one τ_h per seed region. Then, π^0 candidates are identified by using strips in $\eta - \phi$ space, which is basically adding up the four-momenta of electrons and photons. Furhther, charged hadrons ($h^{\pm}$) are selected using the information about charged particles from PF. With these particles, the τ_h candidates are reconstructed

Object to be cleared	against	distance cut ΔR
e	μ	0.4
τ_h	μ, e	0.4
γ	μ, e, τ_h	0.4
Jet	μ, e, τ_h, γ	0.5
b-tagged Jet	μ, e, τ_h, γ	0.5

Table 5: Hierarchy of clearing objects. The distance is defined in Eq. 2. If an object of the left column is closer to an object of the right column than the cut, it will be cleared and not further analysed.

in seven different decay modes, where the momentum of the τ_h is computed by adding the decays constituent particles' momenta. The reconstructed decay modes are shown in Tab. 6. In the last step, an individual τ_h is selected per seed region. To do so, the mass of the

via PF observed hadrons	targetted τ decay
h^-	$\tau^- \to h^-\nu_\tau$
$h^-\pi^0$	$\tau^- \to h^-\pi^0\nu_\tau$
$h^-\pi^0\pi^0$	$\tau^- \to h^-\pi^0\pi^0\nu_\tau$
$h^-h^+h^-$	$\tau^- \to h^-h^+h^-\nu_\tau$
$h^-h^+h^-\pi^0$	$\tau^- \to h^-h^+h^-\pi^0\nu_\tau$
$h^-h^{+/-}$	$\tau^- \to h^-h^+h^-\nu_\tau$
$h^-h^{+/-}\pi^0$	$\tau^- \to h^-h^+h^-\pi^0\nu_\tau$

Table 6: This table shows the reconstructed hadrons by PF as well as the hadronic tau decay that is aimed to be reconstructed in the event. [17] is able to reconstruct three more decay modes compared to previous algorithms, where in two of them one hadron is not reconstructed as a charged particle. The content of the Table also applies for the conjugated charge.

candidate has to fit to the decay mode. Moreover, its charge has to be ± 1, unless for the modes with missing charged (Tab. 6), there the charge has to correspond to the reconstructed hadron with higher p_T. Lastly, all reconstructed hadrons have to be in a certain cone limited to $\Delta R = 0.05 - 0.1$ depending on the τ_h momentum ($\Delta R = \frac{3.0}{p_T[\mathrm{GeV}]}$). At last, the τ_h with the highest p_T is chosen [17].

4.2 Classification

Subsequently, the events are sorted into so called *event classes* regarding the multiplicity of particles that appear in the final state. An event has to consist at least of one data point or have a total MC yield of greater than 0.1 to be regarded as an event class. In *MUSiC*, there are three kinds of event classes. The assigning process is sketched in Fig. 10. The *exclusive*

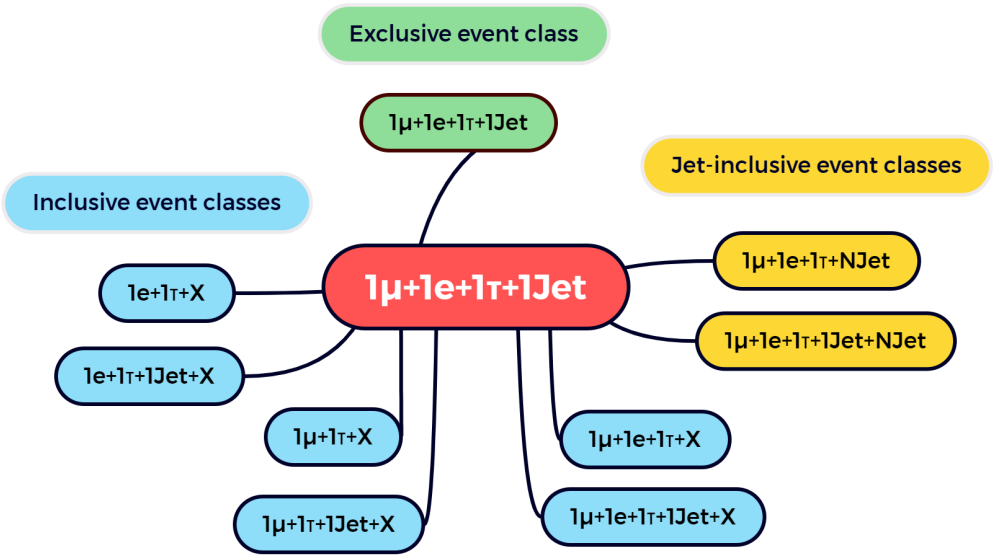

Figure 10: A sketch of the classification process. A certain event (red) can be sorted to exactly one exclusive class (green), but according to the event content to more inclusive (blue) or jet inclusive classes (yellow).

event class is named exactly after the physics objects in the final state of an event, consequently, an event can only be sorted to precisely one exclusive event class. Moreover, new phenomena can occur in several final states because of a certain combination of particles, such as Drell-Yan production in classes including two leptons. Hence, *inclusive* event classes contain all events that have at least the number of objects stated in the name of the class, which is denoted by a "+X". Therefore, a single event can contribute to several different inclusive event classes (see Fig. 10). Lastly, in a collider experiment, jets can also occur from initial radiation, so the number of jets does not necessarily describe the underlying physics process of an event. Hence, there a *jet inclusive* event classes with only jets or b-tagged jets as additionally allowed objects. So an event can be sorted to one or more jet inclusive event classes depending on the number of jets.

4.3 Kinematic Variables

In *MUSiC*, three variables are chosen to account as kinematic distribution of interest. This is because they are particularly promising to be sensitive to phenomena predicted by BSM models. All of those variables are calculated with the class defining physics object, e.g. in an inclusive class, only the objects explicitly mentioned in the class name are considered. Thus in an event class of "$1\mu + 1\tau + 1\text{jet} + X$" the muon, the electron and the Jet are used to calculate the variables. These kinematical quantities are described in the following.

1. S_T: It is the sum of the transverse momenta over all considered particles, defined as

$$S_T = \sum_i |\vec{p}_{T,i}|. \tag{5}$$

Since many BSM theories postulate new heavy particles, it is reasonable to regard this variable because such effects could be visible in the tail of a S_T distribution.

2. M or M_T: If new heavy particles are produced as a resonance, it could also be visible in the mass distribution of its decay products. Here, the combined M corresponds to the invariant mass of the objects of a class. In case of a class with p_T^{miss}, the transverse mass M_T is used due to the lack of information about the z-coordinate of the missing momentum. The tranverse mass M_T is calculated with a sum over all considered object of the class, as

$$M_T = \sqrt{\left(\sum_i E_i\right)^2 - \left(\sum_i p_{x,i}\right)^2 - \left(\sum_i p_{y,i}\right)^2}. \tag{6}$$

.

3. p_T^{miss}: The missing transverse momentum is defined as the negative sum of the transverse momenta of all regarded objects

$$p_T^{miss} = |-\sum_i \vec{p}_{T,i}|. \tag{7}$$

In low p_T^{miss} regions, mainly SM processes with neutrinos or limited detector resolution cause missing momentum. Hence, only events with $p_T^{miss} \geq 100\,\text{GeV}$ are considered. For higher values it indicates that energy escapes the detector undetected and could be linked to new particles with high p_T.

To display these variables the bin widths of the histograms is optimized based on the expected resolution, considering the objects stated in the event class name. The minimal bin size allowed is 10 GeV.

4.4 Implementation of Taus

The previous *MUSiC* publication has not considered tau leptons [18]. Due to their short lifetime (see Sec. 1.2.2), tau decays can happen within the beam pipes of particle accelerators and then can only be reconstructed via objects that are produced in the decay. This could lead to false reconstruction. The leptons of τ_ℓ decays are detected as the arising leptons and τ_h as jets. The identification rate of τ_h has been increased due to a new identification

procedure based on a neural network called *DeepTau* [17]. The reconstruction of a τ_h candidate is described in Sec. 4.1. Unlike before, the *DeepTau* algorithm does not have different discriminators against other particles, but discriminates against jets, electrons and muons simultaneously. It uses the information of all reconstructed particles in the near area of the τ_h candidate to reconstruct it correctly [17]. This algorithm provides an increase of the signal efficiency and decreases the misidentification rate of other particles as τ_h. From here on taus always refer to hadronic tau decays unless it is specified otherwise.

It makes sense to explore how the consideration of taus can expands the *MUSiC* algorithm. Regard as many particles as possible fulfills the *MUSiC* claim of a broad analysis. The algorithm has been extended to analyze tau leptons and the newly observed event classes are presented. Classes with a relatively high deviation to the SM prediction are further investigated.

	VVTight	VTight	Tight	Medium	Loose	VLoose	VVLoose	VVVLoose
D_e	60%	70%	80%	90%	95%	98%	99%	99.5%
D_μ	—	—	99.5%	99.8%	99.9%	99.95%	—	—
D_{jet}	40%	50%	60%	70%	80%	90%	95%	98%

Table 7: τ identification efficiencies for the different working points. They are calculated with a $H \to \tau\tau$ sample [17].

Further criteria to Sec. 4.1 that a tau lepton has to fulfill to be regarded in this analysis are listed in Tab. 8. For a reasonable good identification efficiency, together with a high enough number of observed events, only tight working points are used for the discriminators of the *DeepTau* algorithm. The efficiencies for the different working points are shown in Tab.7. Two decay modes are especially vetoed because the increasing background that arises outweighs the increase of efficiency by including them, according to CMS recommendations. The rejected decay modes are the ones including two charged hadrons with or without an additional neutral π^0. As seen in sec. 4.1, these are the two modes that include a missing charged hadron. Lastly, a certain maximum distance to the primary vertex is required.

Criterion	value
Discriminator score against electrons (D_e)	"Tight"
Discriminator score against muons (D_μ)	"Tight"
Discriminator score against jets (D_{jet})	"Tight"
Decay mode veto	$2h^{\pm}(+\pi^0)$
Distance of lead track with respect to the primary vertex in z-direction	$\lvert dz\rvert < 0.2\,\text{cm}$

Table 8: Additional selection criteria for tau leptons

4.5 Finding deviations

In order to find hints of new phenomena, different steps of statistical tests are performed. If a significant deviation is found, this can be a motivation for a dedicated analysis looking at the deviating final state. This section describes the search algorithm implemented by *MUSiC*.

4.5.1 Region of Interest scan

To find an outstanding deviation between the MC prediction and the measured data, a p-value is calculated for every considered region. The p-value measures the significance of a deviation with respect to the null hypothesis. In the case of *MUSiC* the null hypothesis is that the data is fully described by the SM expectation. The implemented p-value is a mixture of a bayesian and a frequentist approach. The probability of finding N_{data} events in measurements is assumed to be Poisson distributed around the expected value of the SM prediction of N_{SM} events. Concerning statistical disturbances and systematic uncertainties the prediction value N_{SM} is expected to follow a truncated Gaussian distribution [23]. This results in the following definition,

$$p_{data} = \begin{cases} \sum_{i=N_{data}}^{\infty} C \int_0^{\infty} d\lambda \ \exp\left(-\frac{(\lambda - N_{SM})^2}{2\sigma_{SM}^2}\right) \frac{e^{-\lambda}\lambda^i}{i!} & \text{if } N_{data} \geq N_{SM'} \\ \sum_{i=0}^{N_{data}} C \int_0^{\infty} d\lambda \ \exp\left(-\frac{(\lambda - N_{SM})^2}{2\sigma_{SM}^2}\right) \frac{e^{-\lambda}\lambda^i}{i!} & \text{if } N_{data} < N_{SM'}, \end{cases} \tag{8}$$

where C is a factor to normalize the Gaussian distribution and both, statistical and systematic uncertainties, are combined to $\sigma_{SM} = \sqrt{\sigma_{SM,stat}^2 + \sigma_{SM,sys}^2}$. The sum is splitted in two parts, in order to take in to account the case where more data is observed than the MC simulation (summation from N_{data} to inf) or vice-versa (summation from 0 to N_{data}).

As the next step of the analysis a Region of Interest (*RoI*) scan is performed. A region is considered to be a certain number of bins that are interconnected. Every possible combination of regions is regarded, from one bin to all bins in a distribution. This leads to $N_{bins}\left(N_{bins}+1\right)/2$ possible groupings, in such a way that one bin can be part of several regions. In fact, this procedure is used for the mass distribution M or M_T. For S_T and p_T^{miss} a minimum of three bins per region is required to minimize statistical fluctuations, still keeping sensitivity of mass distributions to narrow resonances. Moreover, regions with a low number of events are also removed for statistics reasons. The region with the lowest p-value, which corresponds to an unexpected high deviation, is regarded as the *RoI* and used for further investigation. Fig. 11 shows a sketch of the scan process.

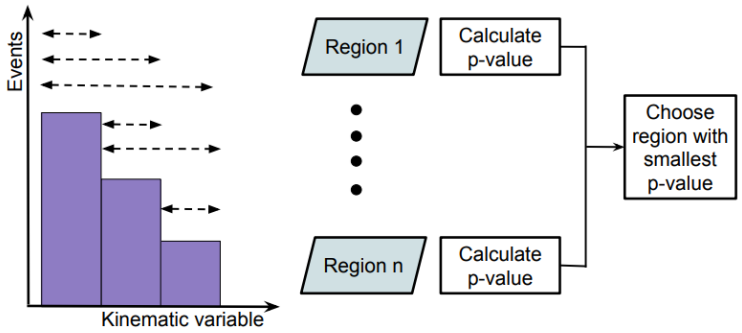

Figure 11: A sketch of the region of interest scan [18]. For every possible region p-values are calculated and the region with the lowest p-value will be further investigated as Region of Interest.

4.5.2 $\tilde{p}$ and Look-Elsewhere Effect

So far, the p-value gives an indication on the likelihood of deviations in a single region. Hence, pseudo-experiments are simulated to find a global measure of a certain deviation. By taking into account the Look-Elsewhere Effect (LEE) the so-called $\tilde{p}$ is computed.
The RoI scan delivers a region with the lowest p-value p^{min}_{data}. The random pseudo-experiments sample toy data from the SM-only hypothesis. A statistical relevant number of simulations, up to 10^5 pseudo-experiments, are sampled and for each one a p-value is calculated repeating the procedure described in Sec. 4.5.1. Here, the RoI can be any region and does not have to be equal to the observed one. Lastly, the $\tilde{p}$ is the ratio of the number of all pseudo-experiments N^{total}_{pseudo} and the number of pseudo-experiments in which the p-value of the RoI is smaller than the observed one in the data p_{min}, given by:

$$\tilde{p} = \frac{N_{pseudo}\left(p_{min} < p^{data}_{min}\right)}{N^{total}_{pseudo}} \tag{9}$$

A pseudo-experiment is performed as follows. For a bin b in any distribution of any class the SM expected value $\langle N_b \rangle$ is used. The corresponding systematic uncertainties are modeled by parameters ν_j. Since they are expected to be correlated across all bins, the shift of an uncertainty source has to be the same across all bins for all event classes.
A parameter ν_j is expected to follow a Gaussian distribution centered around $\langle N_b \rangle$. It is regarded for every bin with the factor $\delta_{\nu_j,b}$. The correlation is taken into consideration by multiplying this uncertainty factor with a standard normally distributed number κ_j, except for statistical uncertainty, which is considered uncorrelated across bins. Finally, a pseudo-experiment results in its certain number of events per bin $\langle N_{b,shifted} \rangle$ by adding a contribution of every kind of uncertainty, which is then used as the mean of a Poisson distribution from which the bin occupancy is sampled:

$$\langle N_{b,shifted} \rangle = \langle N_b \rangle + \sum_j \kappa_j \delta_{\nu_j,b} \tag{10}$$

4.5.3 Global overview

So far, the search algorithm delivers a number of $\tilde{p}$ for several event class distributions. This can be helpful for BSM phenomena that create significant deviations in a few final states. But other theories predict relatively small deviations in a large number of final states. To account that, a global overview diagram is produced by *MUSiC* analyses. All $\tilde{p}$ for each kinematic distributions separately are displayed in one histogram. To emphasize deviations the negative decadic logarithm of $\tilde{p}$ is used. The expectation value is calculated as the median of the toy experiments. The $1\,\sigma$ and $2\,\sigma$ bands are estimated from its quantiles as displayed in an exemplary histogram in Fig. 12.

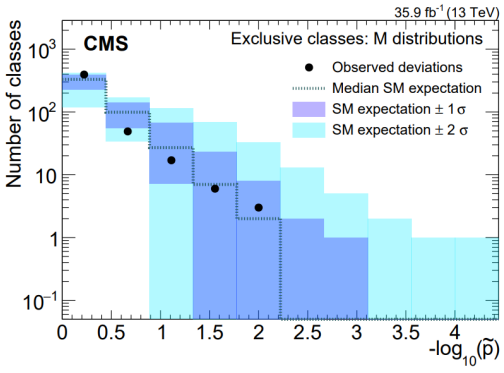

Figure 12: Results of the global overview for invariant mass distributions for exclusive classes. Taken from a previous *MUSiC* analysis using the 2016 Data [18].

4.6 Systematic uncertainties

In this analysis, systematic uncertainties are treated similar to previous *MUSiC* analyses [18]. A summary of these is shown in Tab. 9.

A general uncertainty of 1.6% of the integrated luminosity is estimated. Regarding pileup, a 4.6% uncertainty is estimated on top of the minumum bias cross section and the difference with respect to the nominal count is quoted as systematic uncertainty. In *MUSiC* a general cross section uncertainty of 50% is estimated for processes simulated in leading order (LO). Higher order calculations are treated by variations of QCD renormalization and factorization scale of -0.5 and $+2.0$ (relative variation). Further, parton distribution functions (PDF) describe how a certain momentum of a hadron is divided to its constituent quarks and gluons. PDF cannot be calculated analytically but can only be computed after measurements. A corresponding systematic uncertainty is estimated by following the PDF4LHC recommendations [41]. During the analysis process unreasonable high uncertainties for PDF have been found. In those cases, the uncertainty is limited to 60%. The coupling constant α_S (see Sec.

1.1.1) is varied around a central value of 0.118. Moreover, the kinematic variables like p_T or η of the measured particles have uncertainties regarding the location of detection. Hence, different uncertainties are applied as stated in more detail in [18], and for taus in [17]. Despite the already tight selection criteria, a 50% uncertainty is estimated due to misidentified objects. This is mainly because of jets being incorrectly identified as leptons or photons. Vice-versa wrong identifications arenegligible. Lastly, a statistical uncertainty regarding the limited number of generated events is included.

Source of uncertainty	typical value
Integrated luminosity	1.6%
Pileup	$< 5\%$
Cross sections of SM processes	LO: 50% higher order: varies
Parton distribution functions	Varies, following PDF4LHC [41] recommendations
Value of α_S	Varies, variations of ± 0.002 around central value (0.118)
e, μ, τ and γ energy scales	$0.1 - 10.00\%$
Jet energy scale and resolution	$3 - 5\%$
Unclustered energy	Varies, typically $0 - 20\,\text{GeV}$
Reconstruction and identification efficiency	Varies, $< 10\%$
Misidentification uncertainties	50%
MC statistical uncertainty	Varies, up to 30%

Table 9: Systematic uncertainties used in this analysis [18].

4.7 Evaluation of the Run-2 UL data

As already mentioned, the *MUSiC* analysis is currently under developed. Hence, in this thesis the integrated p-value (Eq. 8, considering the whole distribution as one region) is the central tool. The *RoI* scan and further steps of *MUSiC* are not applied here. Performing this analysis on the Run-2 UL data from 2018, a total number of 1801 event classes including tau leptons arise. This section show the results of this analysis. In the presented plots an overview of the 30 most occupied event classes regarding the MC yield is exhibited. The SM prediction is displayed in different colors according to the simulated process and the observed data as black dots with statistical uncertainty. The systematic uncertainties are drawn as hashed stripes. The p-value calculated for a certain event class is also shown in the plot.
Tab. 13 gives an overview in how many classes are observed and shows new classes that emerge from including tau leptons to the analysis framework. It compares the number classes that have a MC yield (≥ 0.1 events) with the number of classes that contain data (≥ 1 events). The thresholds are mentioned in Sec. 4.2. In the end, a total of 1101 new

event classes containing data are observed by implementing tau leptons to *MUSiC*.

	MC	Data
exclusive	1558	1034
inclusive	1781	1202
jet inclusive	1691	1153
total	5030	3389

	MC	Data
exclusive w/ τ	538	323
inclusive w/ τ	658	402
jet inclusive w/ τ	605	376
total w/ τ	1801	1101

Figure 13: The left table shows the number of event classes that arise in the 2018 data and the right table shows the number of all event classes that contain at least one τ_h.

Regarding the p-values of all event classes with at least one τ_h, it appears that there is only a small number of event classes with a considerable low p-value, which is visible in the cumulative distribution of the p-values in Fig. 14. The median of the p-value distribution is 0.4.

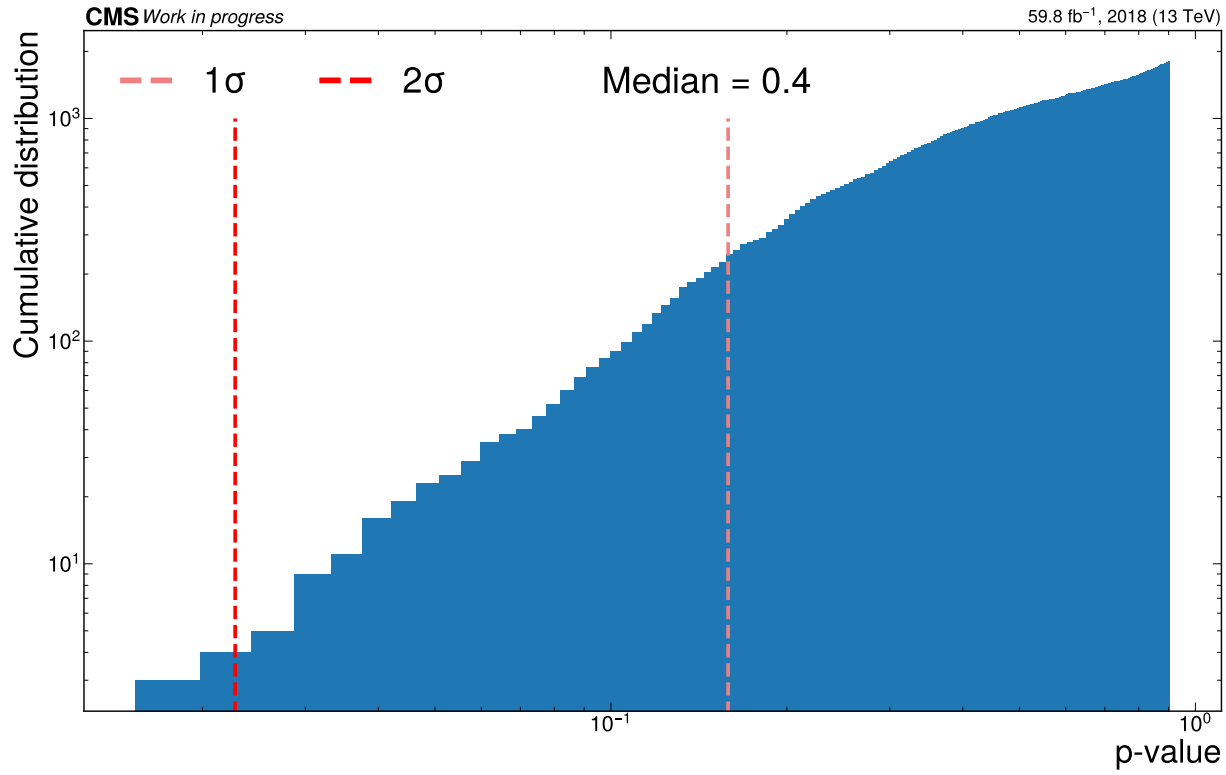

Figure 14: Cumulative distribution of the p-values of the event classes that contain at least one τ_h.

4.7.1 Exclusive event classes

Fig. 15 shows the most occupied exclusive event classes including taus. As one can expect, the most simple classes, "$1\mu + 1\tau$" and "$1e + 1\tau$", have the highest events counts. This is followed by classes containing one Jet each and then more complex classes. Overall, the observed data is in good agreement with the SM prediction within the uncertainties. This is supported by the high p-values of the classes. The lowest shown p-value of $p = 0.15$, in the "$1e + 1\tau + 1\text{bjet} + p_T^{miss}$" event class, corresponds to a Z-score of about $\approx 1.04\sigma$.

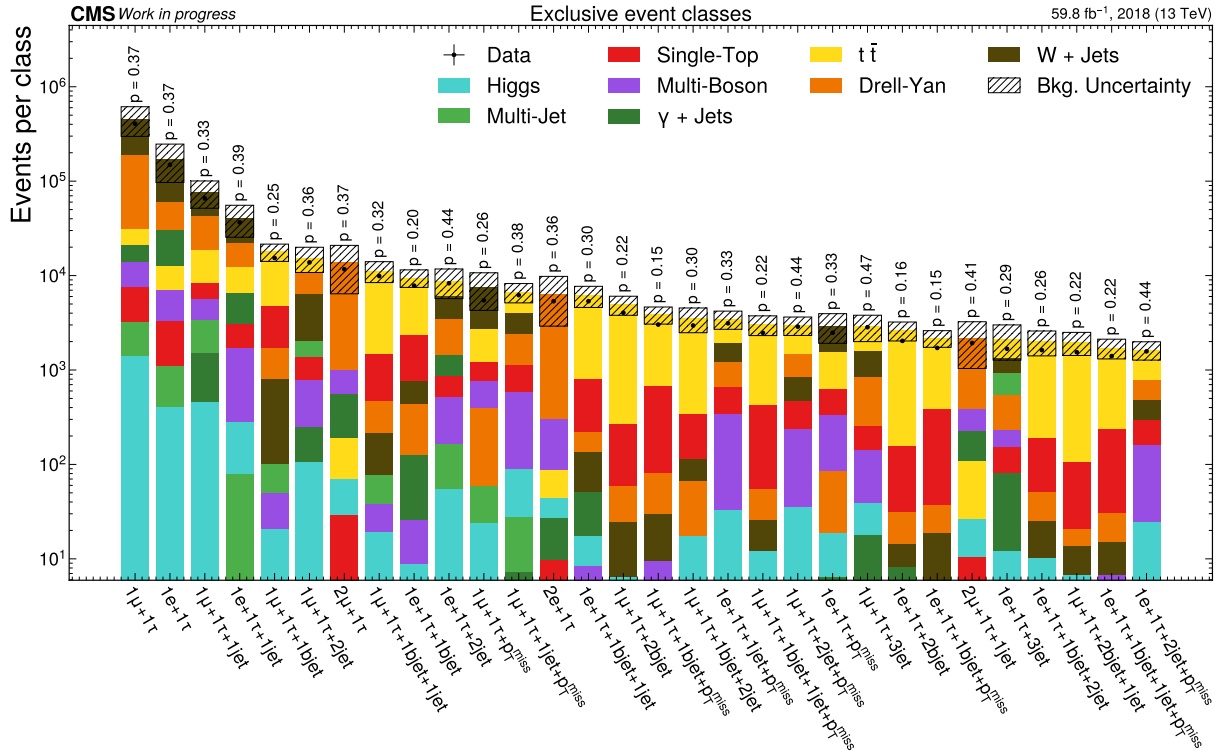

Figure 15: The 30 most occupied exclusive event classes that contain at least one tau lepton regarding their MC yield.

Event class: $1e/1\mu + 1\tau$

Fig. 16 shows the invariant mass distribution of the "$1e + 1\tau$" exclusive event class as well as Fig. 17 this distribution of the "$1\mu + 1\tau$" exclusive class. Appendix B contains a table on how the individual MC process groups are sorted to aggregation groups for the event class plots (as in Fig. 15). In these classes a dominant contribution of *Drell-Yan* is expected, regarding the production of a Z boson which then decays to a τ_ℓ and a τ_h resulting in the two classes. A peak of *Drell-Yan* is visible below the mass of 91 GeV due to the neutrinos in the τ decays that have not been detected. But apparently the contribution of W + *Jets* is dominant. Considering this a potentially high rate of wrongly reconstructed ("misidentified") taus has been found in these classes. One can also observe high uncertainty bars in

the higher mass region as well as bins with a very high *QCD* contribution, which can be due to only a few *QCD* events weighted by their high cross sections. Still both outcomes are worth further investigation.

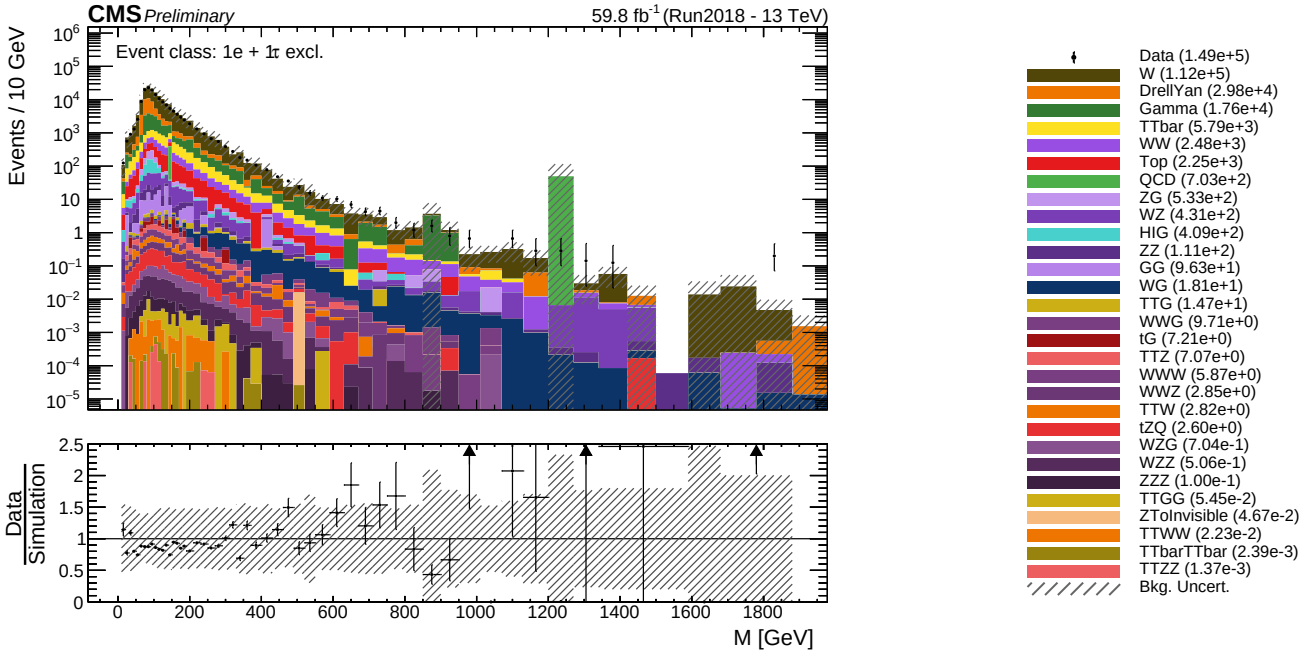

Figure 16: Invariant mass distribution for the $1e + 1\tau$ exclusive event class. The legend is displayed on the right and also shows the total number of event counts per process group and Data.

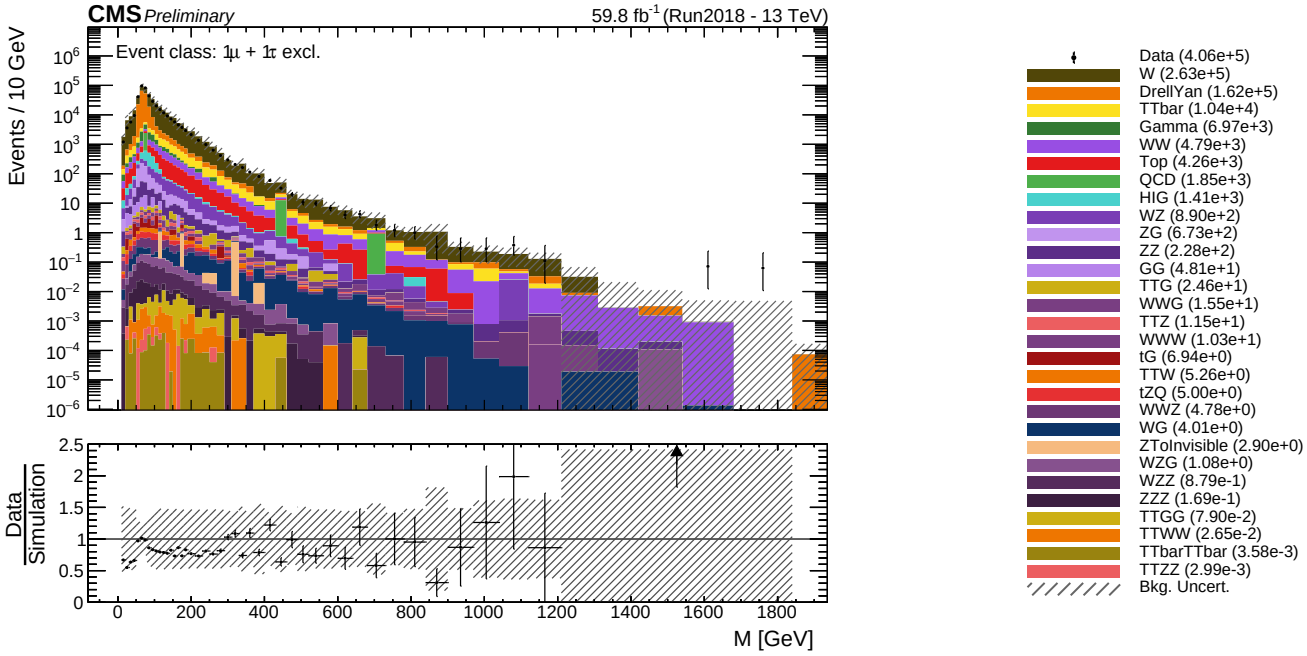

Figure 17: Invariant mass distribution for the $1\mu + 1\tau$ exclusive event class. The legend is displayed on the right and also shows the total number of counts per process group and Data.

Inclusive and Jet inclusive event classes

Regarding the most occupied inclusive and jet inclusive event classes, the same observations can be made. The most occupied inclusive and jet inclusive classes are displayed in Appendix A. One can say that the algorithm performs as expected. The dominance of *W + Jets* can be explained. So this serves as a validation of the implementation of τ_h to *MUSiC*.

4.7.2 Investigation of most deviating classes

Some classes appear to deviate more from the SM prediction than others. The ten most deviating classes are summarized in Tab. 10 and their counts are presented in Fig. 18. One can see correlation in the classes, because for certain combinations of physical objects, namely "$1\mu + 1\tau + 1\gamma + 1\text{bjet} + p_T^{miss}$" and "$2\mu + 1\tau + 2\text{bjet} + p_T^{miss}$", the inclusive and jet inclusive event class appear in this list. There is also the inclusive class of "$1\mu + 1\tau + 1\gamma + 1\text{bjet}$", which corresponds to the first objects except for the missing transverse momentum. Moreover, all three kinds of classes with the objects "$2\mu + 1\tau + 1\text{bjet} + 2\text{jet} + p_T^{miss}$" have a low p-value. Since the Z-score is less than 2 for all classes, no significant deviation is found. Still, for a closer look this section regards the distributions of the kinematic variables. The most deviating event class is shown as an example. The other distributions of the remaining nine event classes are presented in Appendix C. The exclusive event classes corresponding to these classes, that appear in the list as inclusive and jet inclusive class, are also documented there.

event class	p-value	Z-score
$2\mu + 1\tau + 1\text{bjet} + 2\text{jet} + p_T^{miss} + \text{NJet}$	0.0154	2.16
$1\mu + 1\tau + 1\gamma + 1\text{bjet} + p_T^{miss} + \text{X}$	0.0176	2.11
$1\mu + 2\tau + 3\text{jet} + p_T^{miss}$	0.0178	2.10
$1\mu + 1\tau + 1\gamma + 1\text{bjet} + p_T^{miss} + \text{NJet}$	0.0202	2.05
$2\mu + 1\tau + 2\text{bjet} + p_T^{miss} + \text{X}$	0.0277	1.92
$1\mu + 1\tau + 1\gamma + 2\text{bjet} + 1\text{jet} + \text{X}$	0.0298	1.88
$2\mu + 1\tau + 1\text{bjet} + 2\text{jet} + p_T^{miss} + \text{X}$	0.0301	1.88
$1\mu + 1\tau + 1\gamma + 1\text{bjet} + \text{X}$	0.0316	1.86
$2\mu + 1\tau + 2\text{bjet} + p_T^{miss} + \text{NJet}$	0.0322	1.85
$2\mu + 1\tau + 1\text{bjet} + 2\text{jet} + p_T^{miss}$	0.0334	1.83

Table 10: The most deviating event classes (of the 1801 event classes that have at least one tau lepton) regarding the p-value. The absolute p-value as well as the corresponding Z-score is also shown.

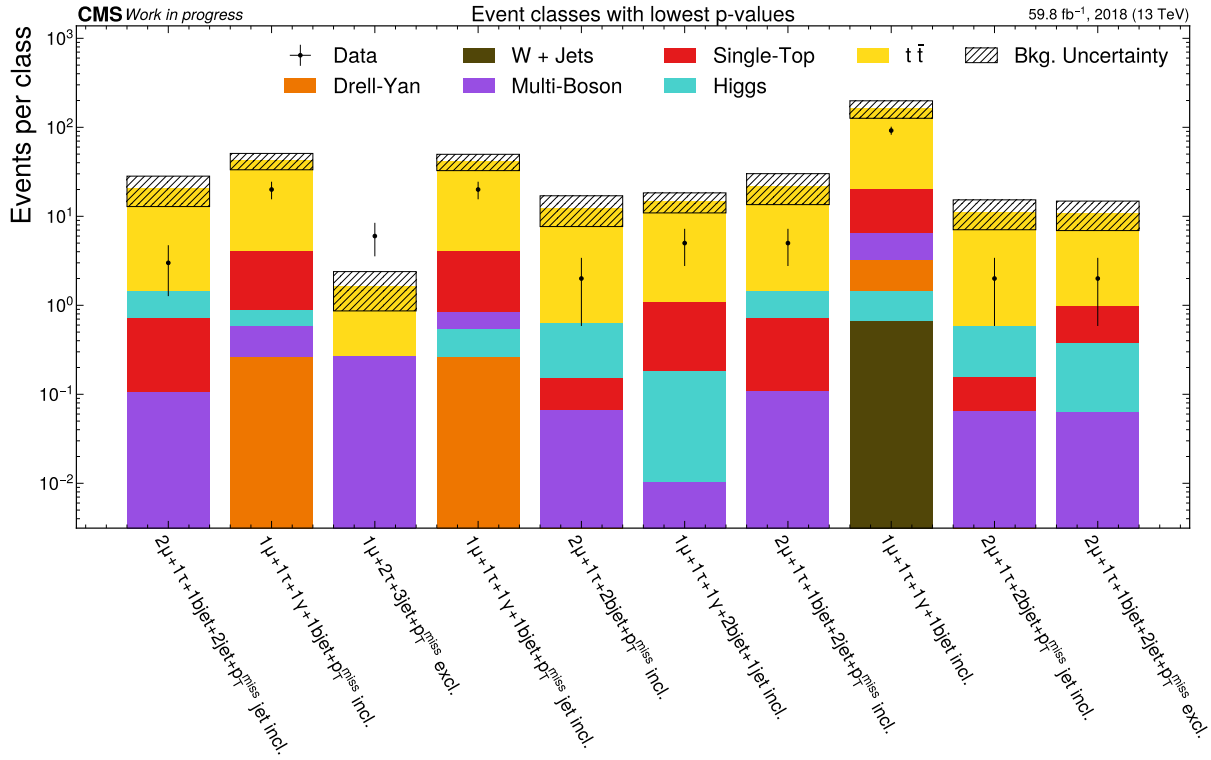

Figure 18: Event counts of the classes with the ten lowest p-values that at least have one tau lepton.

Jet inclusive event class: $2\mu + 1\tau + 1\text{bjet} + 2\text{jet} + \mathbf{p_T^{miss}}$

As an example, the kinematic distributions of the most deviating event class (see headline) are shown. As seen in Fig. 18, this event class has an excess of MC compared to the measured data.
Fig. 19 shows the transverse mass distribution. Three data points are measured that do not fit well to the expectation. The MC yield is low and several bins have a large uncertainty. The same observations can be made for the S_T distribution, except for a slightly better agreement of Data and MC prediction, which is visible in Fig. 20. In contrast to that, the missing transverse momentum p_T^{miss} fits well to the prediction. Regarding this distribution in Fig. 21, one can assume that it continues for lower energies with a not negligible contribution. So the strict criteria for p_T^{miss} used in *MUSiC* can be a reason for that deviation. The small statistics of data events may also account to that.

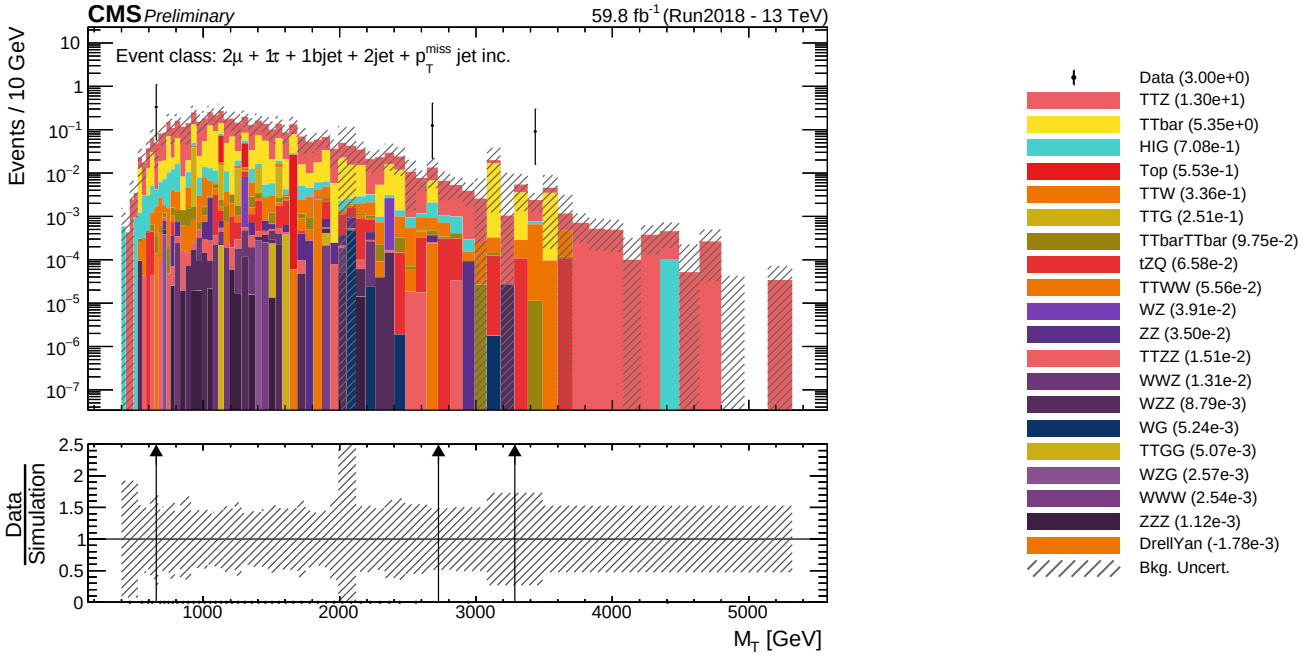

Figure 19: Transverse mass distribution of the $2\mu + 1\tau + 1\text{bjet} + 2\text{jet} + p_T^{miss}$ jet inclusive event class. The legend is displayed on the right and also shows the total number of counts per process group and Data.

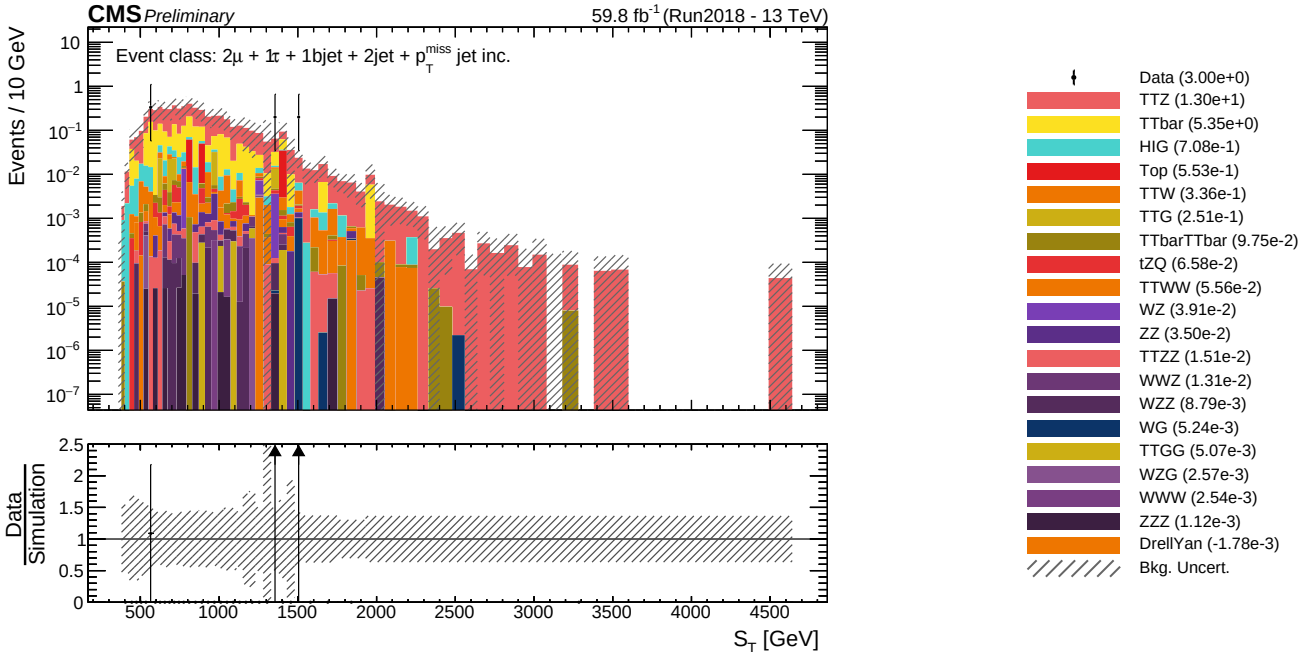

Figure 20: Sum of the transverse momenta distribution of the $2\mu+1\tau+1\text{bjet}+2\text{jet}+p_T^{miss}$ jet inclusive event class. The legend is displayed on the right and also shows the total number of counts per process group and Data.

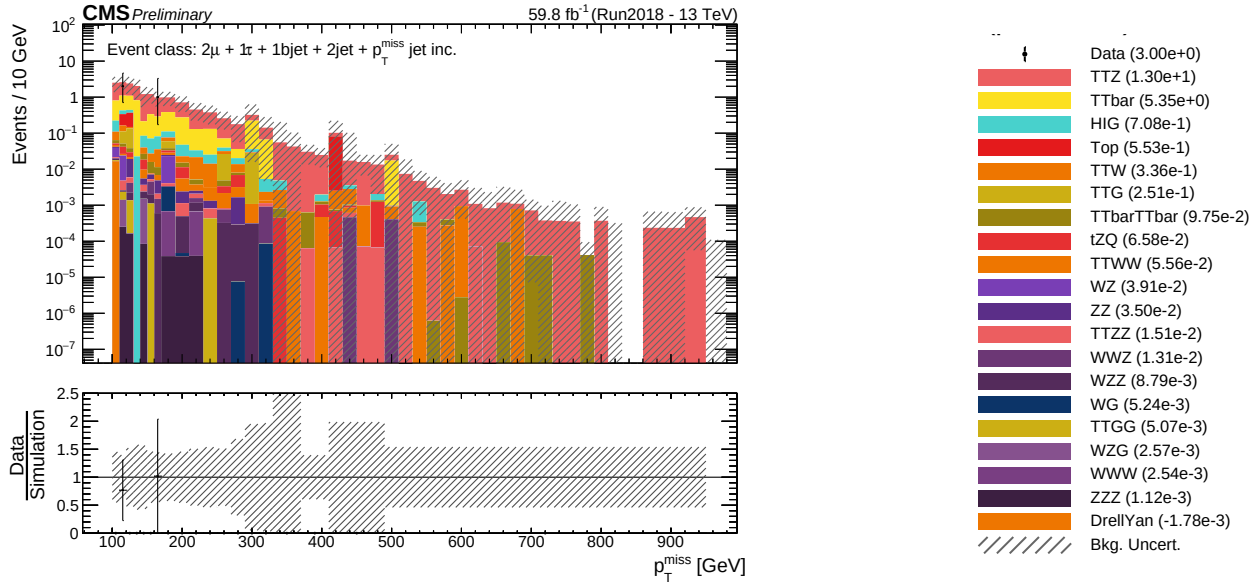

Figure 21: Missing transverse momentum distribution of the $2\mu+1\tau+1\text{bjet}+2\text{jet}+p_T^{miss}$ jet inclusive event class. The legend is displayed on the right and also shows the total number of counts per process group and Data.

General observations on the other classes

Regarding the remaining event class similar observations can be made. In most of the distributions there are several bins with high uncertainty. The only event classes that has a deficit in MC yield is worth to be investigated further, since the others have a deficit of data counts. Moreover, in some of the classes the measured data is in agreement with the prediction within the uncertainties, but for higher energies a lack of data occurs. Moreover, for some event classes there are bins with a small contribution in high energy regions. The additional shown $2\mu + 1\tau + 2\text{bjet} + p_T^{miss}$ exclusive event class has no data point, but is shown for completeness.

5 Sensitivity studies

In order to check and demonstrate *MUSiC* capability of observing New Physics, a sensitivity study is performed. Samples of hypothetical excited tau leptons (see Sec. 2) are used to simulate events that are not described by the SM. They are also listed in Tab. 18. Samples with different masses of the τ^* are investigated, but for all samples the constant Λ mentioned in Sec. 2.1 is equal to 10 TeV. This section shows similar event class plots in which the contribution of the signal samples is presented in blue. Since the Region of Interest scan is not performed in this thesis, one can assume that only individual classes with a certain deviation are detectable. Hence, the signal is plotted on top of the histograms to make visible in which classes the contribution is relevant.

A common way to perform a sensitivity study is the comparision of the SM-only and the SM plus a signal hypothesis. Regarding the evolving process of the current *MUSiC* analysis, a simpler approach is used. This section compares the data with the SM plus signal prediction using the arising p-value. The dependency on the measured data clearly is a disadvantage in terms of determining the sensitivity of this algorithm to BSM signals in general.

5.1 Excited Tau leptons with low mass

This section studies a signal that is expected to be clear. It is done to observe the effects of the signal to the τ selection and hence to validate that the analysis is performed properly.

In order to find classes with a relevant signal distribution the relative difference $\delta p = (p^{signal} - p^{data})/p^{data}$ is calculated, where p^{data} is the p-value obtained by comparing Data and SM-only prediction, and p^{signal} is the p-value that arises after including the signal MC. Regarding the signal sample with a $m_{\tau^*} = 175\,\text{GeV}$ the event classes with the ten lowest δp are listed in Tab. 11 and their event counts are displayed in Fig. 22. As expected from Sec. 2.1 a signal contribution occurs in event classes that contain 2 τ and 1 γ. Moreover, the exclusive event class $1\mu + 1\tau + 1\gamma + p_T^{miss}$ also shows a low δp which corresponds to a τ_ℓ.

Jet inclusive event class: $2\tau + 1\gamma + \mathbf{p_T^{miss}}$
This event class has most decreasing p-value so it is worth it to look at its kinematic distributions. The mass M_T distribution is shown in Fig. 23 and it is well visible, that the signal delivers a relevant contribution for high energies. However, some bins have a high uncertainty. The S_T and p_T^{miss} distributions can be found in Appendix D.1 and similar observations can be made.

Significance of the p^{signal}-values
Taking a closer look to the differences of the p-values, there are still no significant deviations even though the signal is included. A comparison of the arising p-values (Tab. 11) is shown in Fig. 24. Only the exclusive event class of $1\mu + 1\tau + 1\gamma + p_T^{miss}$ that already has a low

event class	p^{signal}-value	p^{data}-value	δp [%]
$2\tau + 1\gamma + p_T^{miss} + \text{NJet}$	0.0348	0.537	−93.52
$2\tau + 1\gamma + p_T^{miss} + \text{X}$	0.0305	0.443	−93.12
$2\tau + 1\gamma + p_T^{miss}$	0.0468	0.664	−92.95
$2\tau + 1\gamma + \text{X}$	0.0369	0.441	−91.65
$2\tau + 1\gamma$	0.0508	0.489	−89.62
$2\tau + 1\gamma + \text{NJet}$	0.0566	0.409	−86.16
$2\tau + 1\gamma + 1\text{jet} + p_T^{miss}$	0.0455	0.304	−85.03
$2\tau + 1\gamma + 1\text{jet} + p_T^{miss} + \text{X}$	0.0765	0.469	−83.70
$1\mu + 1\tau + 1\gamma + p_T^{miss}$	0.0215	0.131	−83.63
$2\tau + 1\gamma + 1\text{jet} + p_T^{miss} + \text{NJet}$	0.0973	0.581	−83.26

Table 11: These are the classes with the most decreasing p-value when the signal with a τ^* mass of 175 GeV and $\Lambda = 10$ TeV is included.

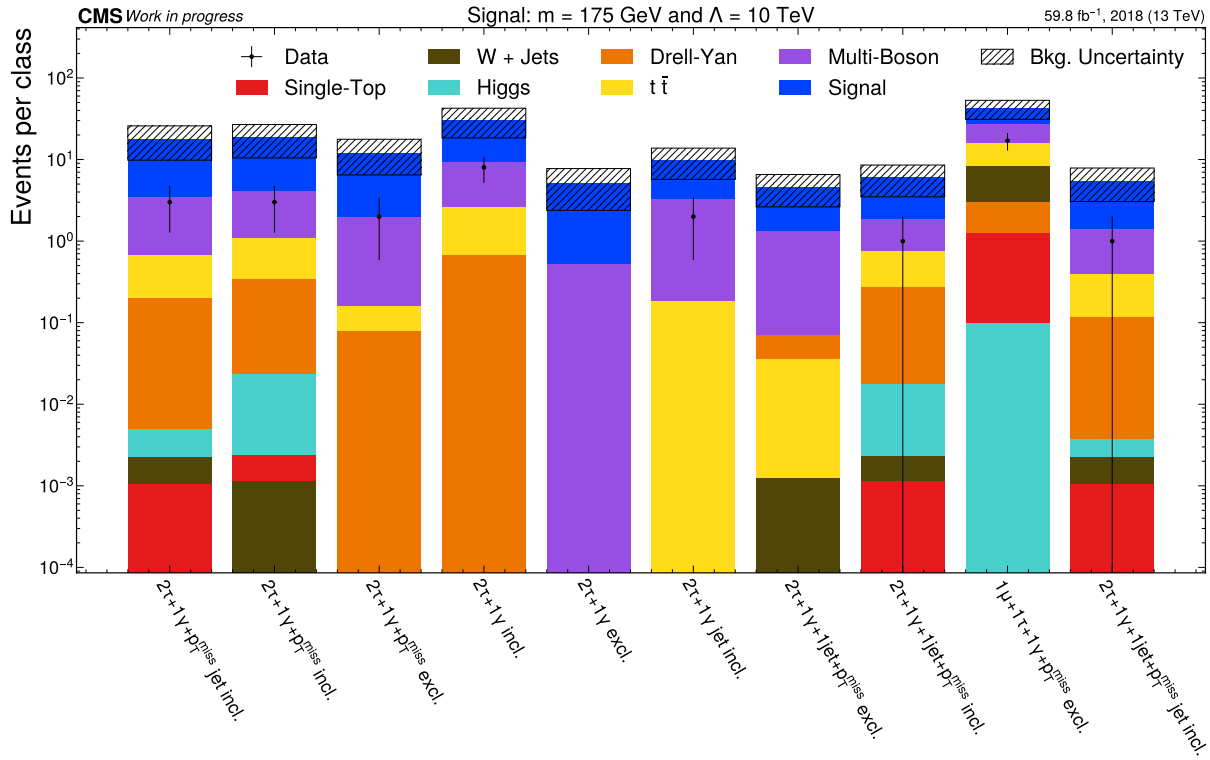

Figure 22: This plot shows the event classes, with the most decreasing p-value when the signal is included ($m_{\tau^*} = 175$ GeV and $\Lambda = 10$ TeV). Two event classes have no data point.

p^{data}-value, has a p^{signal}-value beyond the significance of 2σ. The p-value decreases for all classes considerably, but the level of 3σ is not reached. Further steps have to be performed to properly study the sensitivity to this signal, e.g. perform the *RoI* scan.

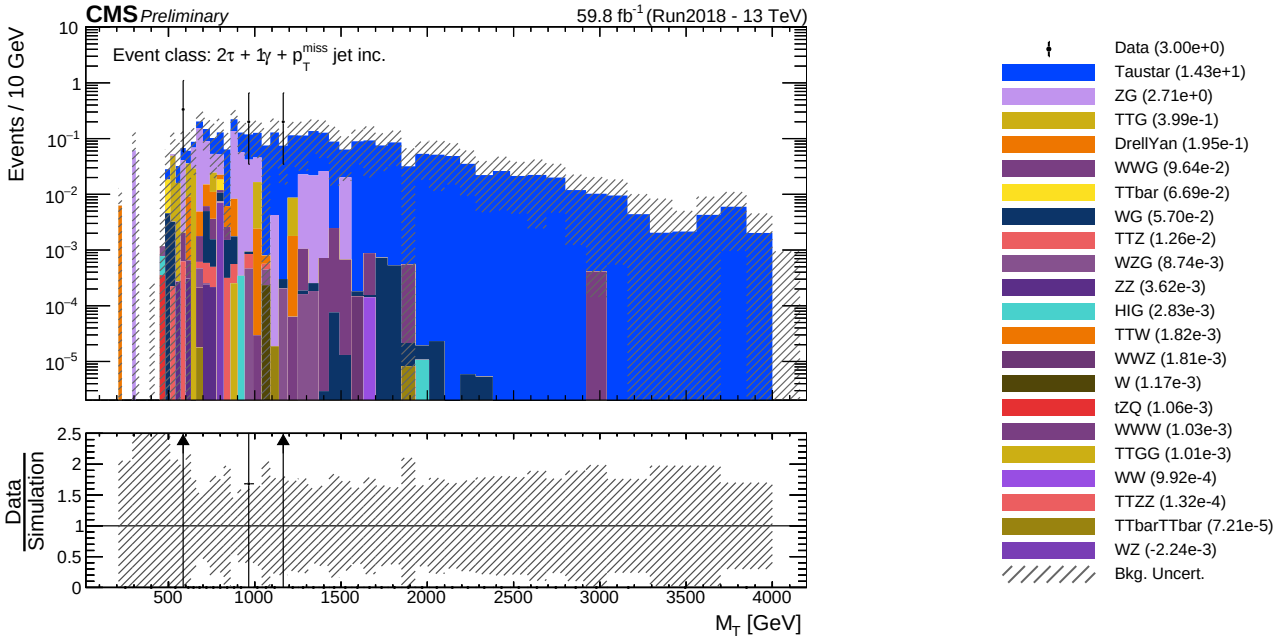

Figure 23: Transverse mass distribution of the $2\tau + 1\gamma + p_T^{miss}$ jet inclusive event class when the signal ($m_{\tau^*} = 175\,\text{GeV}$ and $\Lambda = 10\,\text{TeV}$) is included. The legend is displayed on the right and also shows the total number of counts per process group and Data. The signal process group is called "Taustar".

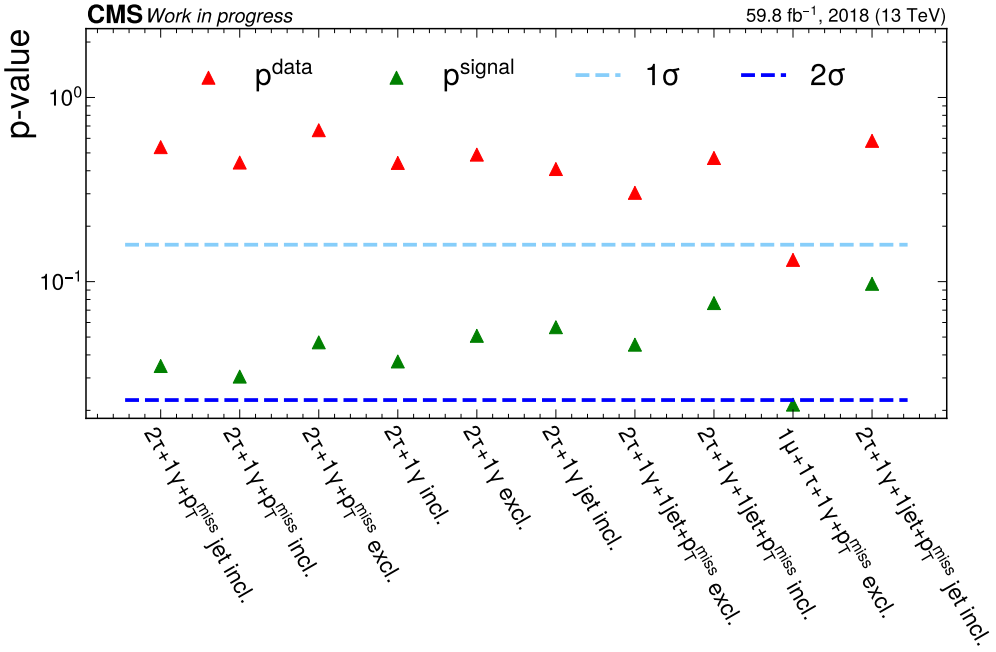

Figure 24: This plot shows the p-values of the event classes, with the lowest δp when the signal is included ($m_{\tau^*} = 175\,\text{GeV}$ and $\Lambda = 10\,\text{TeV}$). The significance level is also shown by the dashed lines.

5.2 Sensitivity to higher masses

Ongoing CMS analyses expect to exclude the τ^* hypothesis for masses smaller than 3000 GeV, which makes it interesting to look at signal samples above this threshold. As done in the previous section, the ten event classes with the lowest δp are presented in Appendix D.2. Tab. 12 shows the p-values of these classes for a signal with a mass of 3000 GeV, the remaining are documented in Appendix E. An overview of these p-values is shown in Fig. 25. Since the cross section of the simulated process decreases with a higher mass, the contribution of the signal also decreases. For a mass of 3000 GeV and a mass of 3500 GeV a change of the p-value is visible, but clearly not significant. The decrease of the p-value is not visible for the higher masses of the signal and it is negligible.

event class	p^{signal}-value	p^{data}-value	δp [%]
$2\tau + 1\gamma + p_T^{miss} + \mathrm{X}$	0.412	0.443	−6.98
$2\tau + 1\gamma + p_T^{miss} + \mathrm{NJet}$	0.504	0.537	−6.20
$2\tau + 1\gamma + \mathrm{X}$	0.420	0.441	−4.80
$2\tau + 1\gamma + p_T^{miss}$	0.635	0.664	−4.31
$2\tau + 1\gamma + 1\mathrm{jet} + p_T^{miss}$	0.291	0.304	−4.27
$2\tau + 1\gamma + 1\mathrm{jet} + p_T^{miss} + \mathrm{X}$	0.453	0.469	−3.43
$1\tau + 2\gamma + p_T^{miss} + \mathrm{X}$	0.265	0.273	−3.09
$2\tau + 1\gamma + 1\mathrm{jet} + p_T^{miss} + \mathrm{NJet}$	0.564	0.581	−2.98
$1\mu + 1\tau + 1\gamma + p_T^{miss}$	0.128	0.131	−2.20
$2\tau + 1\gamma + 1\mathrm{jet} + \mathrm{X}$	0.504	0.515	−2.01

Table 12: These are the classes with the most decreasing p-value when the signal with a τ^* mass of 3000 GeV and $\Lambda = 10$ TeV is included.

The mass distributions of the event classes with the most decreasing p-values including the signals with higher masses are shown in appendix D.2. The contribution of the signal decreases with the increasing mass as expected. One can see that the actual height of the signal peak is diminished compared to most contributing SM processes. The peak is smaller by a factor of about a hundred for 3000 GeV up to ten thousand for 5000 GeV. But its width covers several thousands of GeV, so that the total contribution is, at least for masses of 3000 GeV and 3500 GeV, slightly visible in the p-values as described before.

The algorithm is not sensitive to the signal with higher masses. As already suggested in the previous section, it is worth the use of the *RoI* scan in order to increase the sensitivity of the *MUSiC* analysis to this signal.

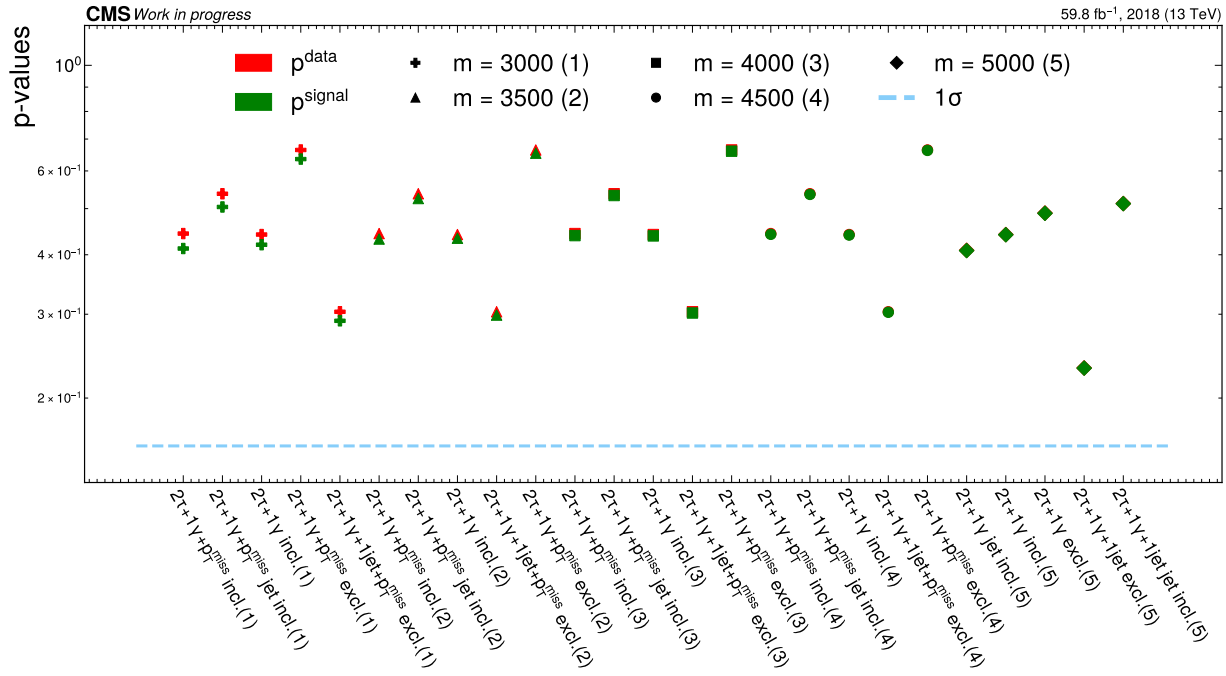

Figure 25: This plot shows the p-values of the five event classes, with the lowest δp for all signals with a mass of $m_{\tau^*} \geq 3000\,\text{GeV}$ ($\Lambda = 10\,\text{TeV}$). The significance level is also shown by the dashed line. There is no considerable change of p-values visible. The use of the *RoI* scan improve the performance of the *MUSiC* search.

6 Conclusion and perspectives

One can say that the implementation of tau leptons to *MUSiC* delivers a large number of new classes to investigate. For the most populated classes the measured data points fit well to the MC prediction. Unexpected contributions in the prediction are due to still existing false reconstruction. Some deviations are visible for less populated classes, but it is far away from a Z-score of 3σ. A further investigation shows high uncertainties for several bins as well as low populated event classes.

Furthermore, a sensitivity study has been performed. A considerable change in the obtained p-values is observed, when comparing the Data to a signal with very low τ^* masses. The contributions of the signal are detected in those event classes that would be expected. But the p-values that have been calculated for these classes still show no significant deviation.
For higher masses of the τ^*, above the threshold expected to be excluded by dedicated analyses, the signals weakens and becomes undetectable.

To conclude, this is a good foundation for further studies. The algorithm behaves as expected when taus are included. It has become clear, that p-values can show strong signals but *MUSiC* Region of Interest scan is necessary to find weak deviations which can occur because of events with a comparetively small cross section, such as many BSM phenomena. Tau leptons can be a good contribution to future *MUSiC* analyses.

Regarding this thesis, some more interesting approaches of analysis arise. First, one can have a closer look on the most deviating classes to understand why there is such an excess of MC prediction as observed in this thesis as well as the high uncertainties for some of the bins. Then, it is worth to investigate the high rate of false reconstruction in the most occupied classes. Thirdly, one can work on the implementation of Single-τ and Double-τ triggers to also include event classes that consist of taus (τ_h) only. Moreover, in a larger scope of work, a full *MUSiC* analysis can be performed including taus, especially the further calculation of the $\tilde{p}$ and the global overview to observe whether there are small deviations over all event classes that may have been overlooked using the present approach and of course to repeat the excited tau study for higher masses. Including these ideas, sensitivity studies of other BSM signals, that only have taus in final states may be interesting, since the event classes of 2τ or $1\tau+p_T^{miss}$ would be examinable. It is also interesting to analyze the CMS Data of other Run-2 years (2016 and 2017) in order to assess the agreement between measurement and prediction.

7 Acknowledgements

First, I want to say thank you to Prof. Dr. Thomas Hebbeker for the opportunity of writing my Bachelor's thesis in the *MUSiC* research group as well as Prof. Dr. Martin Erdmann to agreeing in performing the second examination and for the inspiring lecture on particle physics last year. I would also like to thank Dr. Arnd Meyer and Dr. Felipe Torres da Silva de Araujo for giving me the interesting topic of investigating tau leptons. Moreover, I want to express my appreciation to the very pleasant atmosphere in the *MUSiC* office and the friendly colleagues from the other offices making me enjoy every day at the institute. I want to specially mention Dr. Felipe Torres da Silva de Araujo, M.Sc. Chinmay Seth and B.Sc. Yannik Kaiser, who have always helped me when I needed some, regardless of whether it was getting to know the *MUSiC* code, my first steps in *ROOT* or learning to work with *C++*. Also to mention are my fellow bachelor students Lucas Karwatzki and B.Sc. Nils Esper, who especially has helped me with *LaTeX* related affairs. I really enjoyed working with you in the last months.

I want to say thank you to my friends for all the enjoyable and unforgettable moments in the last three years, for the constant moral support and for just being there for me when I need someone to talk to. But in the end, I want to pronounce my biggest appreciation and say thank you to my lovely mother, Sabine Kersten, who has always been there for me and who has made it possible for me to go to university by supporting me over my whole childhood. You are the greatest person that I know and will always have a special place in my heart, thank you!

References

[1] A. Airapetian et al. “ATLAS: Detector and physics performance technical design report. Volume 1”. In: (May 1999).

[2] Andrade, A. *Machine Learning for a Model Unspecific Search in CMS*. Master thesis. 2023. URL: https://web.physik.rwth-aachen.de/user/hebbeker/theses/andrade_master.pdf.

[3] U. Baur, M. Spira, and P. M. Zerwas. “Excited-quark and -lepton production at hadron colliders”. In: *Phys. Rev. D* 42 (3 1990), pp. 815–824. DOI: 10.1103/PhysRevD.42.815. URL: https://link.aps.org/doi/10.1103/PhysRevD.42.815.

[4] G. L. Bayatian et al. “CMS Physics: Technical Design Report Volume 1: Detector Performance and Software”. In: (2006).

[5] Bilenky, S. “Neutrino oscillations: from an historical perspective to the present status”. In: *Journal of Physics: Conference Series* 718.6 (2016). DOI: 10.1088/1742-6596/718/6/062005.

[6] CERN. *LHC Facts*. URL: https://www.lhc-facts.ch/. (accessed: 16.09.2023).

[7] CERN. *LHC the guide FAQ / CERN Brochure 2021 004*. URL: https://www.home.cern/resources/brochure/knowledge-sharing/lhc-facts-and-figures. (accessed: 25.09.2023).

[8] CERN. *The Standard Model*. URL: https://home.cern/science/physics/standard-model. (accessed: 19.09.2023).

[9] D K Choudhury and Krishna Kingkar Pathak. “Comments on the perturbation of Cornell potential in a QCD potential model”. In: *Journal of Physics: Conference Series* 481.1 (2014), p. 012022. DOI: 10.1088/1742-6596/481/1/012022. URL: https://dx.doi.org/10.1088/1742-6596/481/1/012022.

[10] Cid-Vidal, X. & Cid, R. “LHC: the emptiest space in the solar system”. In: *Physics Education* 46.1 (2011). DOI: 10.1088/0031-9120/46/1/005.

[11] CMS Collaboration. “Performance of the CMS hadron calorimeter with cosmic ray muons and LHC beam data”. In: *Journal of Instrumentation* 5.03 (2010). DOI: 10.1088/1748-0221/5/03/T03012.

[12] CMS Collaboration. “Performance of the CMS muon detector and muon reconstruction with proton-proton collisions at $\sqrt{s} = 13\,\text{TeV}$”. In: *Journal of Instrumentation* 13.06 (2018). DOI: 10.1088/1748-0221/13/06/P06015.

[13] CMS Collaboration. “The CMS experiment at the CERN LHC”. In: *Journal of Instrumentation* 3.08 (2008). DOI: 10.1088/1748-0221/3/08/S08004.

[14] ALICE Collaboration. “ALICE: Physics Performance Report, Volume I”. In: *Journal of Physics G: Nuclear and Particle Physics* 30.11 (2004), p. 1515. DOI: 10.1088/0954-3899/30/11/E01. URL: https://dx.doi.org/10.1088/0954-3899/30/11/E01.

[15] ATLAS Collaboration. "Observation of a new particle in the search for the Standard Model Higgs boson with the ATLAS detector at the LHC". In: *Physics Letters B* 716.1 (2012), pp. 1–29. ISSN: 0370-2693. DOI: https://doi.org/10.1016/j.physletb.2012.08.020. URL: https://www.sciencedirect.com/science/article/pii/S037026931200857X.

[16] CMS Collaboration. "Calibration of the CMS hadron calorimeters using proton-proton collision data at $\sqrt{s} = 13\,\text{TeV}$". In: *Journal of Instrumentation* 15.05 (2020). DOI: 10.1088/1748-0221/15/05/P05002.

[17] CMS Collaboration. "Identification of hadronic tau lepton decays using a deep neural network". In: *Journal of Instrumentation* 17.07 (2022), P07023. DOI: 10.1088/1748-0221/17/07/p07023. URL: https://doi.org/10.1088%2F1748-0221%2F17%2F07%2Fp07023.

[18] CMS Collaboration. "MUSiC: a model-unspecific search for new physics in proton-proton collisions at $\sqrt{s} = 13\,\text{TeV}$". In: *European Physical Journal C* 81.7 (2021). DOI: https://doi.org/10.1140/epjc/s10052-021-09236-z.

[19] CMS Collaboration. "Observation of a new boson at a mass of 125 GeV with the CMS experiment at the LHC". In: *Physics Letters B* 716.1 (2012), pp. 30–61. ISSN: 0370-2693. DOI: https://doi.org/10.1016/j.physletb.2012.08.021. URL: https://www.sciencedirect.com/science/article/pii/S0370269312008581.

[20] CMS Collaboration. "Particle-flow reconstruction and global event description with the CMS detector". In: *Journal of Instrumentation* 12.10 (Oct. 2017), P10003–P10003. DOI: 10.1088/1748-0221/12/10/p10003.

[21] CMS Collaboration. "Performance of reconstruction and identification of τ leptons decaying to hadrons and ν_τ in pp collisions at $\sqrt{s} = 13\,\text{TeV}$". In: *Journal of Instrumentation* 13.10 (Oct. 2018), P10005–P10005. DOI: 10.1088/1748-0221/13/10/p10005.

[22] D0 Collaboration. "Observation of the Top Quark". In: *Physical Review Letters* 74.14 (Apr. 1995), pp. 2632–2637. DOI: 10.1103/physrevlett.74.2632.

[23] Robert D. Cousins, James T. Linnemann, and Jordan Tucker. "Evaluation of three methods for calculating statistical significance when incorporating a systematic uncertainty into a test of the background-only hypothesis for a Poisson process". In: *Nuclear Instruments and Methods in Physics Research Section A: Accelerators, Spectrometers, Detectors and Associated Equipment* 595.2 (Oct. 2008), pp. 480–501. DOI: 10.1016/j.nima.2008.07.086.

[24] Alessandro De Angelis and Mário Pimenta. "Interactions and Field Theories". In: *Introduction to Particle and Astroparticle Physics: Multimessenger Astronomy and its Particle Physics Foundations*. Cham: Springer International Publishing, 2018, pp. 265–391. ISBN: 978-3-319-78181-5. DOI: 10.1007/978-3-319-78181-5_6. URL: https://doi.org/10.1007/978-3-319-78181-5_6.

[25] Alessandro De Angelis and Mário Pimenta. "Particle Detection". In: *Introduction to Particle and Astroparticle Physics: Multimessenger Astronomy and its Particle Physics Foundations*. Cham: Springer International Publishing, 2018, pp. 109–206. ISBN: 978-3-319-78181-5. DOI: 10.1007/978-3-319-78181-5_4. URL: https://doi.org/10.1007/978-3-319-78181-5_4.

[26] Alessandro De Angelis and Mário Pimenta. "Particles and Symmetries". In: *Introduction to Particle and Astroparticle Physics: Multimessenger Astronomy and its Particle Physics Foundations*. Cham: Springer International Publishing, 2018, pp. 207–263. ISBN: 978-3-319-78181-5. DOI: 10.1007/978-3-319-78181-5_5. URL: https://doi.org/10.1007/978-3-319-78181-5_5.

[27] Alessandro De Angelis and Mário Pimenta. "The Higgs Mechanism and the Standard Model of Particle Physics". In: *Introduction to Particle and Astroparticle Physics: Multimessenger Astronomy and its Particle Physics Foundations*. Cham: Springer International Publishing, 2018, pp. 393–454. ISBN: 978-3-319-78181-5. DOI: 10.1007/978-3-319-78181-5_7. URL: https://doi.org/10.1007/978-3-319-78181-5_7.

[28] Wolfgang Demtröder. "Physics of Elementary Particles". In: *Nuclear and Particle Physics*. Cham: Springer International Publishing, 2022, pp. 173–212. ISBN: 978-3-030-58313-2. DOI: 10.1007/978-3-030-58313-2_7. URL: https://doi.org/10.1007/978-3-030-58313-2_7.

[29] Duchardt, D. "MUSiC: A Model Unspecific Search for New Physics Based on $\sqrt{s} = 8\,\text{TeV}$ CMS Data". Doctoral thesis. RWTH Aachen University, 2017. URL: https://publications.rwth-aachen.de/record/698906.

[30] Eichten, E.J. and Lane, K.D. and Peskin, M.E. "New Tests for Quark and Lepton Substructure". In: *Phys. Rev. Lett.* 50 (11 Mar. 1983), pp. 811–814. DOI: 10.1103/PhysRevLett.50.811.

[31] A. Einstein. "Die Grundlage der allgemeinen Relativitätstheorie". In: *Annalen der Physik* 354.7 (1916), pp. 769–822. DOI: https://doi.org/10.1002/andp.19163540702.

[32] F. Englert and R. Brout. "Broken Symmetry and the Mass of Gauge Vector Mesons". In: *Phys. Rev. Lett.* 13 (9 Aug. 1964), pp. 321–323. DOI: 10.1103/PhysRevLett.13.321. URL: https://link.aps.org/doi/10.1103/PhysRevLett.13.321.

[33] Evans, L. & Bryant, P. "LHC Machine". In: *Journal of Instrumentation* 3.08 (2008). DOI: 10.1088/1748-0221/3/08/S08001.

[34] Zhenkai Fu and Sirui Gao. "The Application of Gravitational Lensing on Observation of Dark Matter Candidates". In: *Journal of Physics: Conference Series* 2386.1 (2022), p. 012076. DOI: 10.1088/1742-6596/2386/1/012076.

[35] Fukuda, Y. et al. (Super-Kamiokande Collaboration). "Evidence for Oscillation of Atmospheric Neutrinos". In: *Phys. Rev. Lett.* 81 (8 1998), pp. 1562–1567. DOI: 10.1103/PhysRevLett.81.1562.

[36] Mary K. Gaillard, Paul D. Grannis, and Frank J. Sciulli. "The standard model of particle physics". In: *Rev. Mod. Phys.* 71 (2 1999), S96–S111. DOI: 10.1103/RevModPhys.71.S96. URL: https://link.aps.org/doi/10.1103/RevModPhys.71.S96.

[37] Harari, H. "Composite models for quarks and leptons". In: *Physics Reports* 104.2 (1984), pp. 159–179. ISSN: 0370-1573. DOI: https://doi.org/10.1016/0370-1573(84)90207-2.

[38] Robert Harlander, Jean-Philippe Martinez, and Gregor Schiemann. "The end of the particle era?" In: *The European Physical Journal H* 48.1 (June 2023), p. 6.

[39] P. W. Higgs. "Broken Symmetries and the Masses of Gauge Bosons". In: *Phys. Rev. Lett.* 13 (16 1964), pp. 508–509. DOI: 10.1103/PhysRevLett.13.508. URL: https://link.aps.org/doi/10.1103/PhysRevLett.13.508.

[40] P.W. Higgs. "Broken symmetries, massless particles and gauge fields". In: *Physics Letters* 12.2 (1964), pp. 132–133. ISSN: 0031-9163. DOI: https://doi.org/10.1016/0031-9163(64)91136-9. URL: https://www.sciencedirect.com/science/article/pii/0031916364911369.

[41] Jon Butterworth, J. et al. "PDF4LHC recommendations for LHC Run II". In: *Journal of Physics G: Nuclear and Particle Physics* 43.2 (Jan. 2016), p. 023001. DOI: 10.1088/0954-3899/43/2/023001.

[42] Kaiser, Y. *Sensitivity study of the MUSIC algorithm for LHC run 2*. Bachelor thesis. 2021. URL: https://web.physik.rwth-aachen.de/user/hebbeker/theses/kaiser_bachelor.pdf.

[43] K. R. Labe. *The Muon g-2 Experiment at Fermilab*. 2022. arXiv: 2205.06336 [hep-ex].

[44] "LEP Design Report Vol.1: The LEP Injector Chain". In: (June 1983).

[45] E. Lopienska. *The CERN accelerator complex*. URL: https://cds.cern.ch/images/CERN-GRAPHICS-2022-001-1. (accessed: 26.09.2023).

[46] F Machefert. "Status of the LHCb detector commissioning and first running scenarios". In: *Journal of Physics: Conference Series* 110.9 (May 2008), p. 092016. DOI: 10.1088/1742-6596/110/9/092016.

[47] Stephen P. Martin and James D. Wells. *Elementary Particles and Their Interactions*. Cham: Springer International Publishing, 2022. ISBN: 978-3-031-14368-7. DOI: 10.1007/978-3-031-14368-7. URL: https://doi.org/10.1007/978-3-031-14368-7.

[48] NASA. *Hubble Finds Dark Matter Ring in Galaxy Cluster*. URL: https://hubblesite.org/contents/media/images/2007/17/2120-Image.html?news=true. (accessed: 19.09.2023).

[49] Oort, J. H. "The force exerted by the stellar system in the direction perpendicular to the galactic plane and some related problems". In: *Bulletin of the Astronomical Institutes of the Netherlands* 6 (1932). URL: https://ui.adsabs.harvard.edu/abs/1932BAN.....6..249O.

[50] Pati, J.C. and Salam, A. and Strathdee, J. "Are quarks composite?" In: *Physics Letters B* 59.3 (1975), pp. 265–268. ISSN: 0370-2693. DOI: https://doi.org/10.1016/0370-2693(75)90042-8.

[51] PBS NOVA, Fermilab, Office of Science, United States Department of Energy, Particle Data Group. *Standard Model of Elementary Physics*. URL: https://commons.wikimedia.org/w/index.php?curid=4286964. (accessed: 17.09.2023).

[52] Martin L. Perl et al. "Evidence for Anomalous Lepton Production in e+ - e- Annihilation". In: *Phys. Rev. Lett.* 35 (1975), pp. 1489–1492. DOI: 10.1103/PhysRevLett.35.1489.

[53] Pook, T. "A model unspecific search in CMS (MUSiC) using 13 TeV Data". Doctoral thesis. RWTH Aachen University, 2022. URL: https://publications.rwth-aachen.de/record/861275.

[54] Sakuma, T. and McCauley, T. "Detector and Event Visualization with SketchUp at the CMS Experiment". In: *Journal of Physics: Conference Series* 513.2 (June 2014), p. 022032. DOI: 10.1088/1742-6596/513/2/022032.

[55] The Royal Swedish Academy of Sciences. *The 2015 Nobel Prize in Physics - Press release*. URL: https://www.nobelprize.org/prizes/physics/2015/press-release. (accessed: 16.09.2023).

[56] Dr. Felipe Torres da Silva de Araujo. Private communication. Oct. 2023.

[57] SMITH, GEORGE E. "J. J. Thomson and The Electron: 1897–1899 An Introduction". In: *The Chemical Educator* 2.6 (Dec. 1997), pp. 1–42. DOI: 10.1007/s00897970149a.

[58] Terazawa, H. and MYasuè, M. and Akama, K. and Hayashi, M. "Observable effects of the possible sub-structure of leptons and quarks". In: *Physics Letters B* 112.4 (1982), pp. 387–392. ISSN: 0370-2693. DOI: https://doi.org/10.1016/0370-2693(82)91075-9. URL: https://www.sciencedirect.com/science/article/pii/0370269382910759.

[59] Trocino, D. "The CMS High Level Trigger". In: *Journal of Physics: Conference Series* 513.1 (June 2014), p. 012036. DOI: 10.1088/1742-6596/513/1/012036.

[60] James D. Wells. "The Once and Present Standard Model of Elementary Particle Physics". In: *Discovery Beyond the Standard Model of Elementary Particle Physics*. Cham: Springer International Publishing, 2020, pp. 51–69. ISBN: 978-3-030-38204-9. DOI: 10.1007/978-3-030-38204-9_2. URL: https://doi.org/10.1007/978-3-030-38204-9_2.

[61] R. L. Workman et al. "Review of Particle Physics". In: *PTEP* 2022 (2022), p. 083C01. DOI: 10.1093/ptep/ptac097.

A Most occupied inclusive and jet inclusive event classes

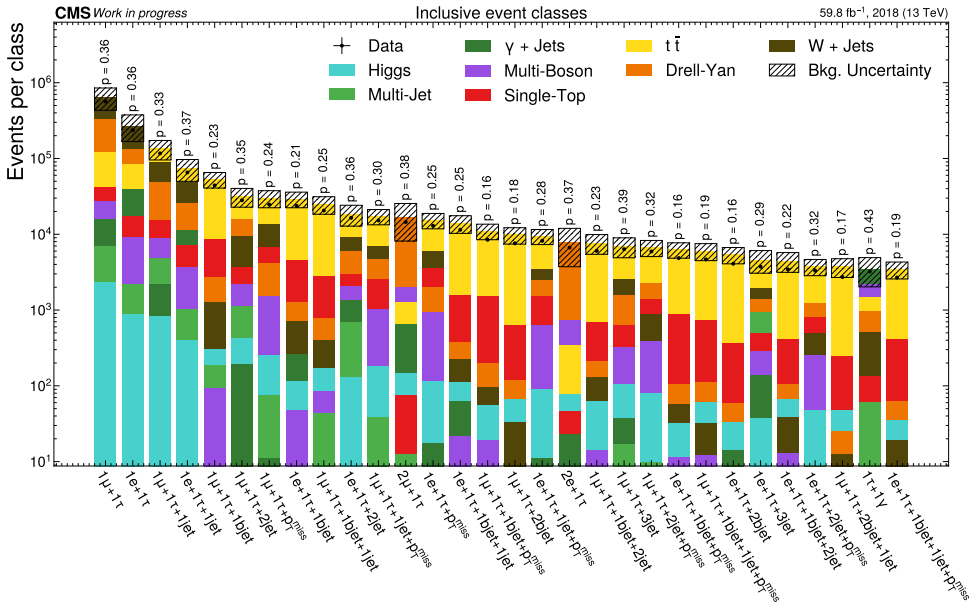

Figure 26: The 30 most occupied inclusive event classes that contain at least one tau lepton regarding their MC yield.

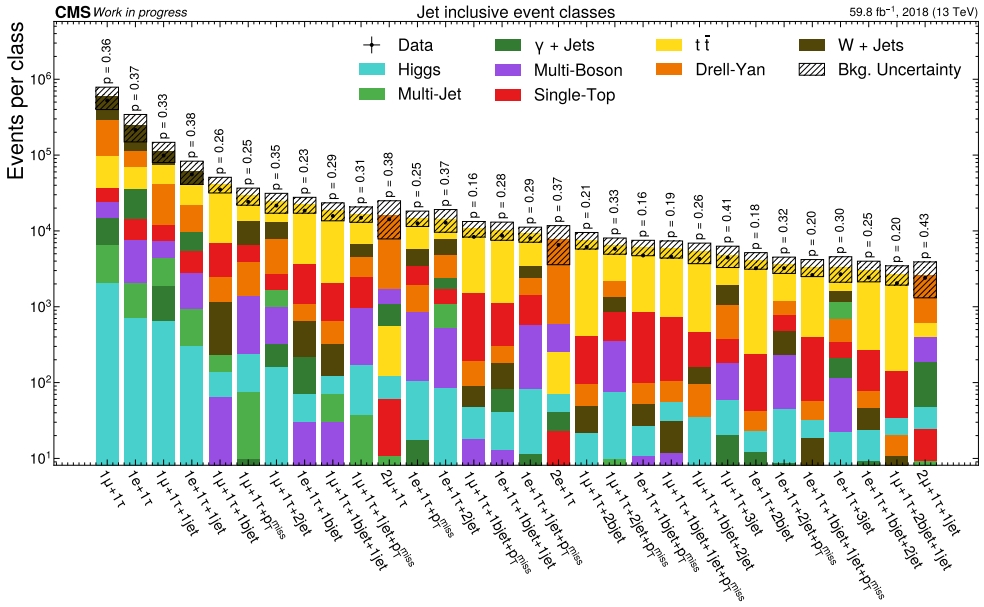

Figure 27: The 30 most occupied jet inclusive event classes that contain at least one tau lepton regarding their MC yield.

B Aggregation groups

Tab. 13 shows which samples are labelled as which process in plots.

Label name	Samples included
Drell-Yan	"DrellYan", "ZToInvisible"
Higgs	"HIG"
Multi-Boson	"WW", "ZZ", "WZ", "WG"
	"GG", "WWW", "WWZ", "WZZ"
	"ZZZ", "WWG", "WGG", "WZG", "ZG"
Multi-Jet	"QCD"
Single-Top	"Top", "tG", "tZQ"
$t\bar{t}$	"TTW", "TTZ", "TTbar"
	"TTbarTTbar", "TTG", "TTGG"
	"TTWW", "TTZZ"
W + Jets	"W"
γ + Jets	"Gamma"

Table 13: Aggregation groups of MC samples.

C Kinematic distributions of classes with low p-value

This section shows the kinematic distributions of the other most deviating event classes. The exclusive event class corresponding to the correlating event classes are also shown here.

C.1 Event classes: $1\mu + 1\tau + 1\gamma + 1\text{bjet} + \mathbf{p_T^{miss}}$

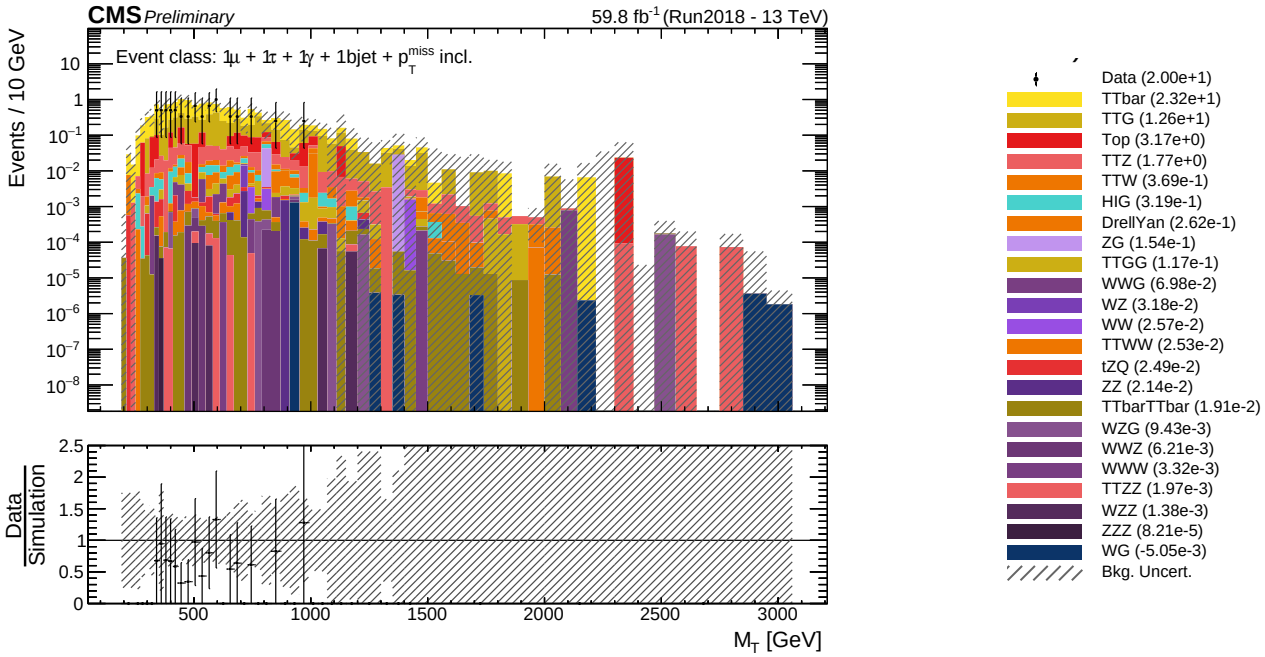

Figure 28: Transverse mass distribution of the $1\mu + 1\tau + 1\gamma + 1\text{bjet} + p_T^{miss}$ inclusive event class. The legend is displayed on the right and also shows the total number of counts per process group and Data.

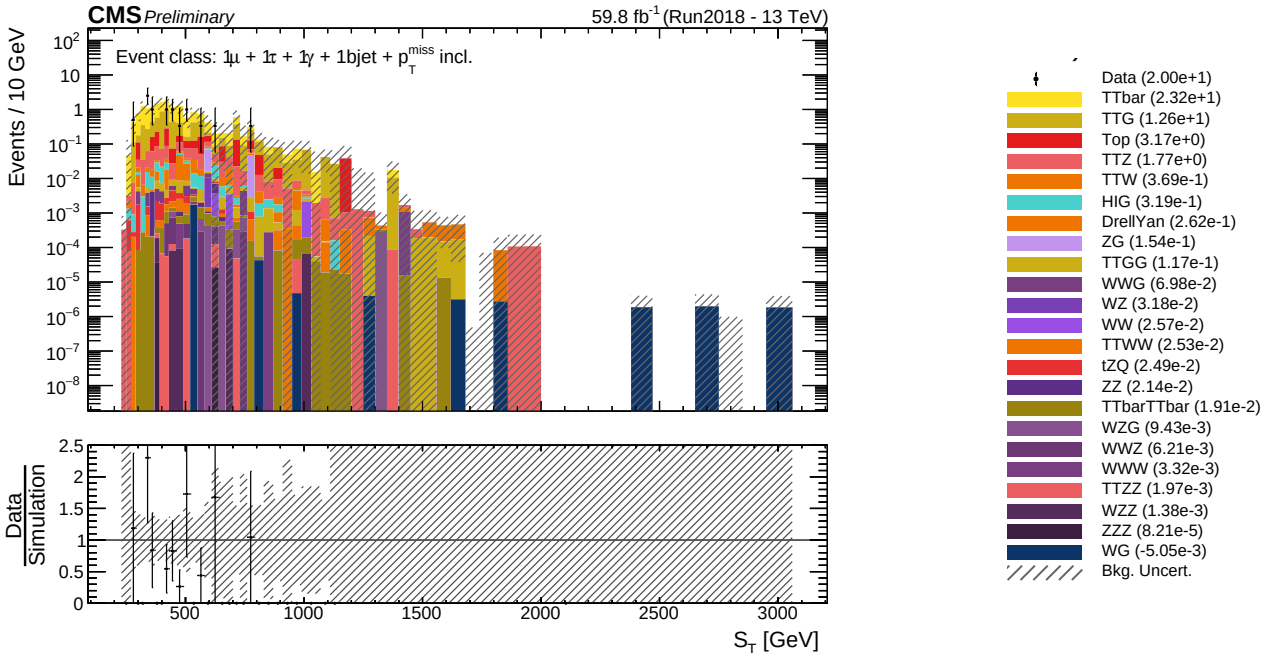

Figure 29: Sum of the transverse momenta distribution of the $1\mu + 1\tau + 1\gamma + 1\text{bjet} + p_T^{miss}$ inclusive event class. The legend is displayed on the right and also shows the total number of counts per process group and Data.

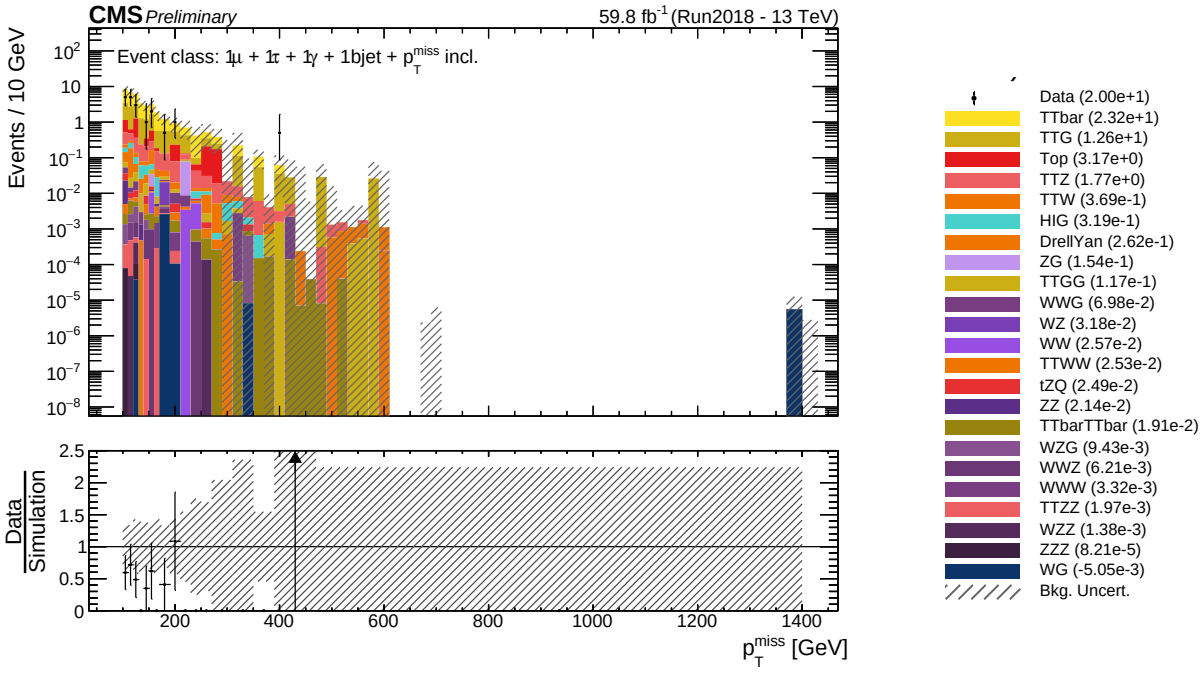

Figure 30: Missing transverse momentum distribution of the $1\mu + 1\tau + 1\gamma + 1\text{bjet} + p_T^{miss}$ inclusive event class. The legend is displayed on the right and also shows the total number of counts per process group and Data.

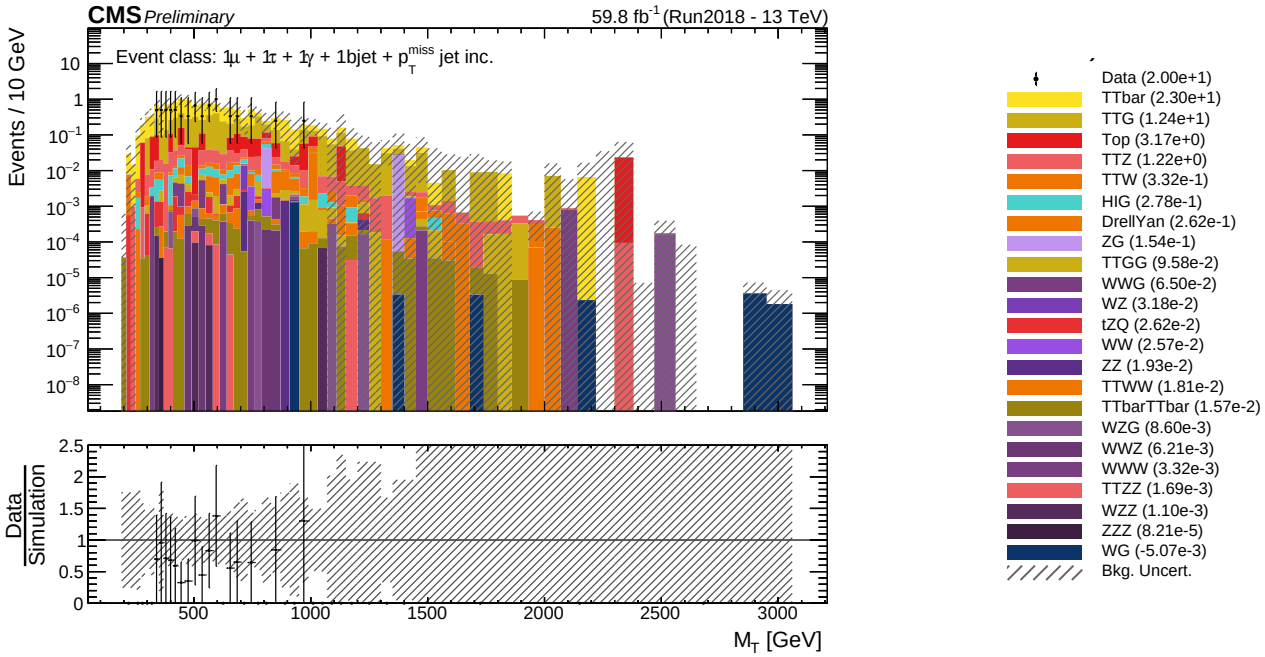

Figure 31: Transverse mass distribution of the $1\mu + 1\tau + 1\gamma + 1\text{bjet} + p_T^{miss}$ jet inclusive event class. The legend is displayed on the right and also shows the total number of counts per process group and Data.

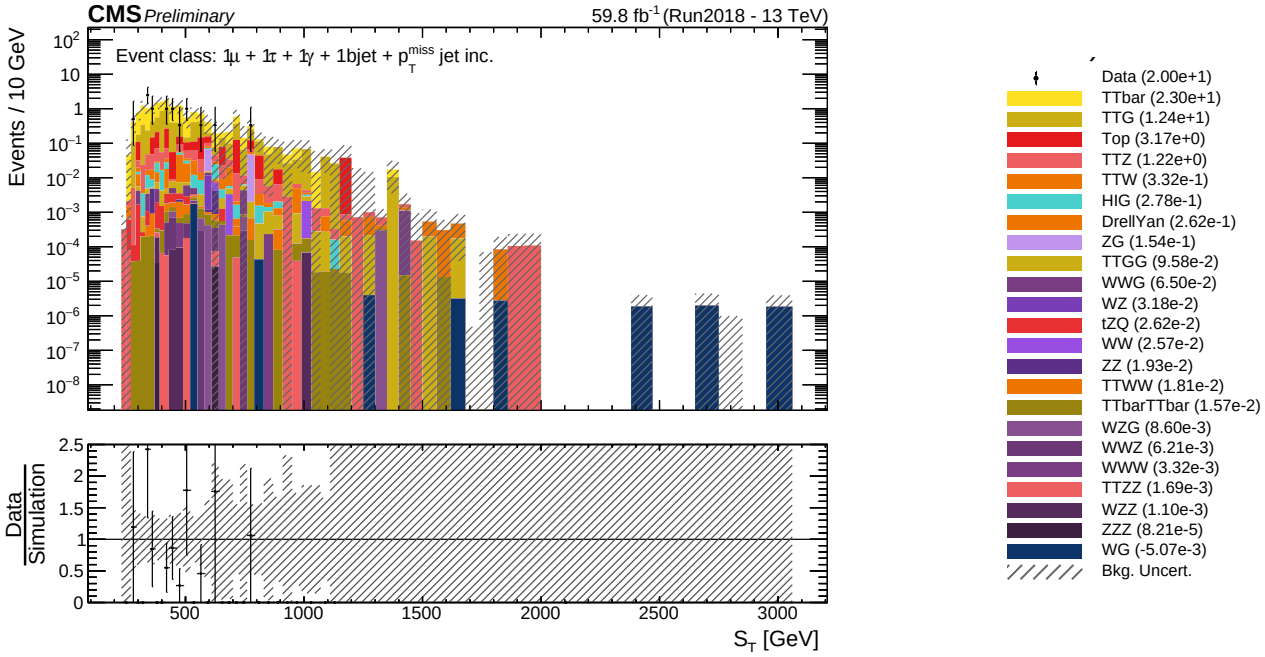

Figure 32: Sum of the transverse momenta distribution of the $1\mu + 1\tau + 1\gamma + 1\text{bjet} + p_T^{miss}$ jet inclusive event class. The legend is displayed on the right and also shows the total number of counts per process group and Data.

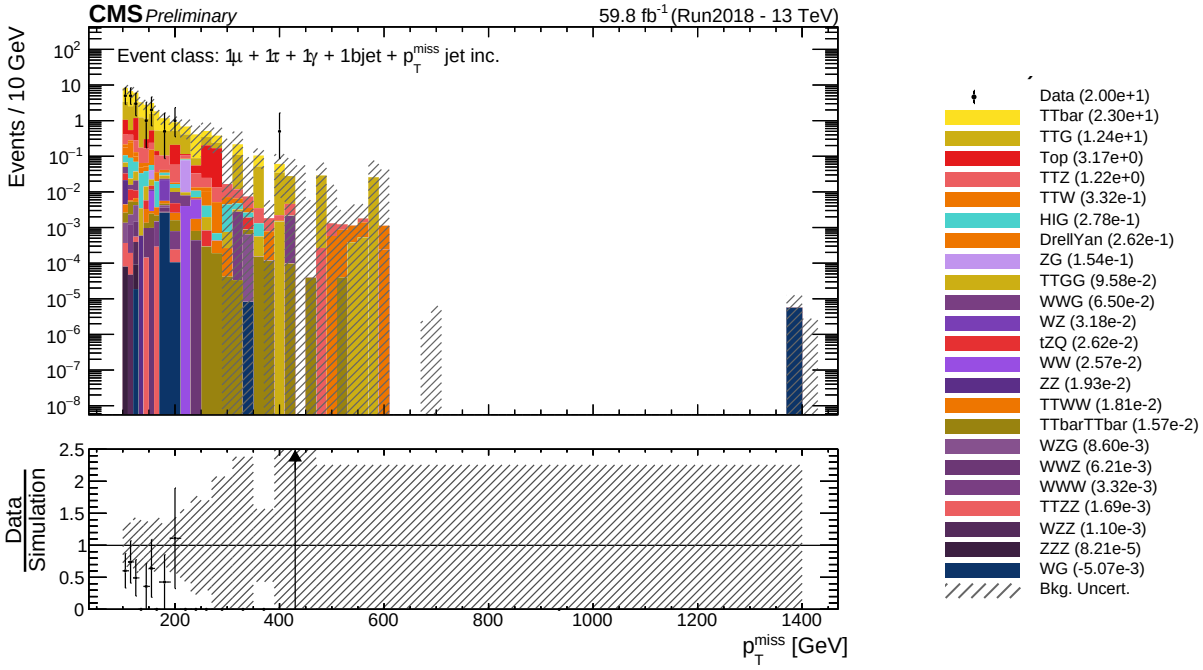

Figure 33: Missing transverse momentum distribution of the $1\mu + 1\tau + 1\gamma + 1\text{bjet} + p_T^{miss}$ jet inclusive event class. The legend is displayed on the right and also shows the total number of counts per process group and Data.

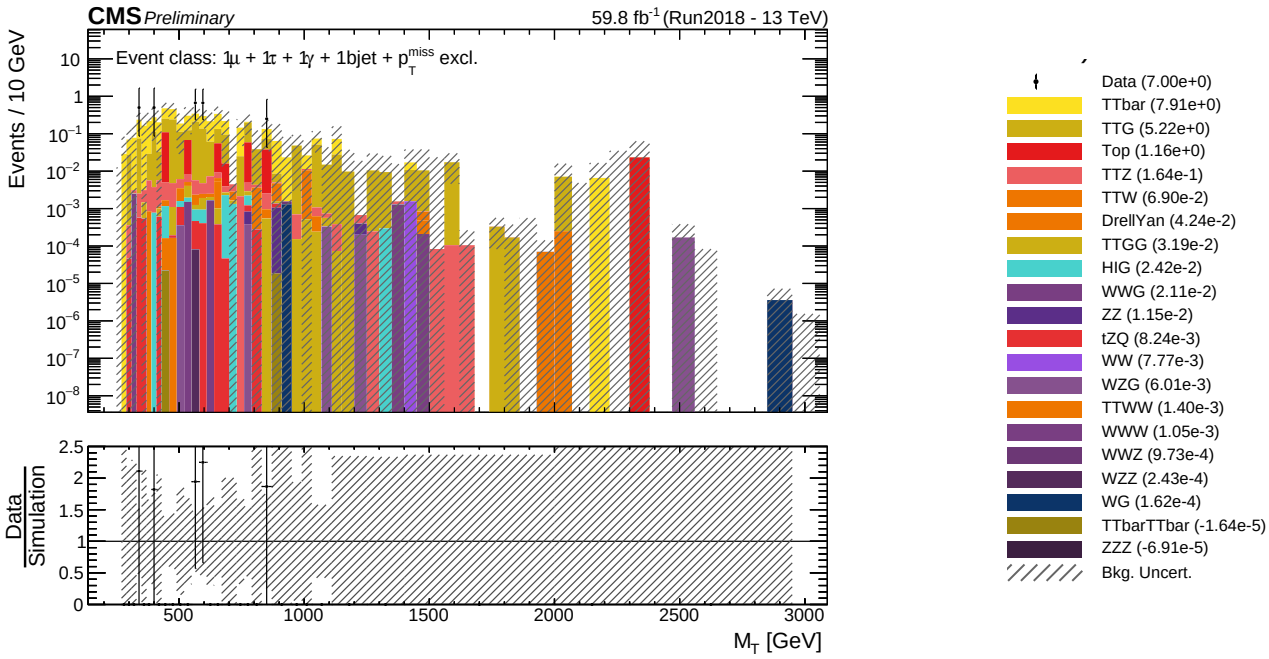

Figure 34: Transverse mass distribution of the $1\mu + 1\tau + 1\gamma + 1\text{bjet} + p_T^{miss}$ exclusive event class. The legend is displayed on the right and also shows the total number of counts per process group and Data.

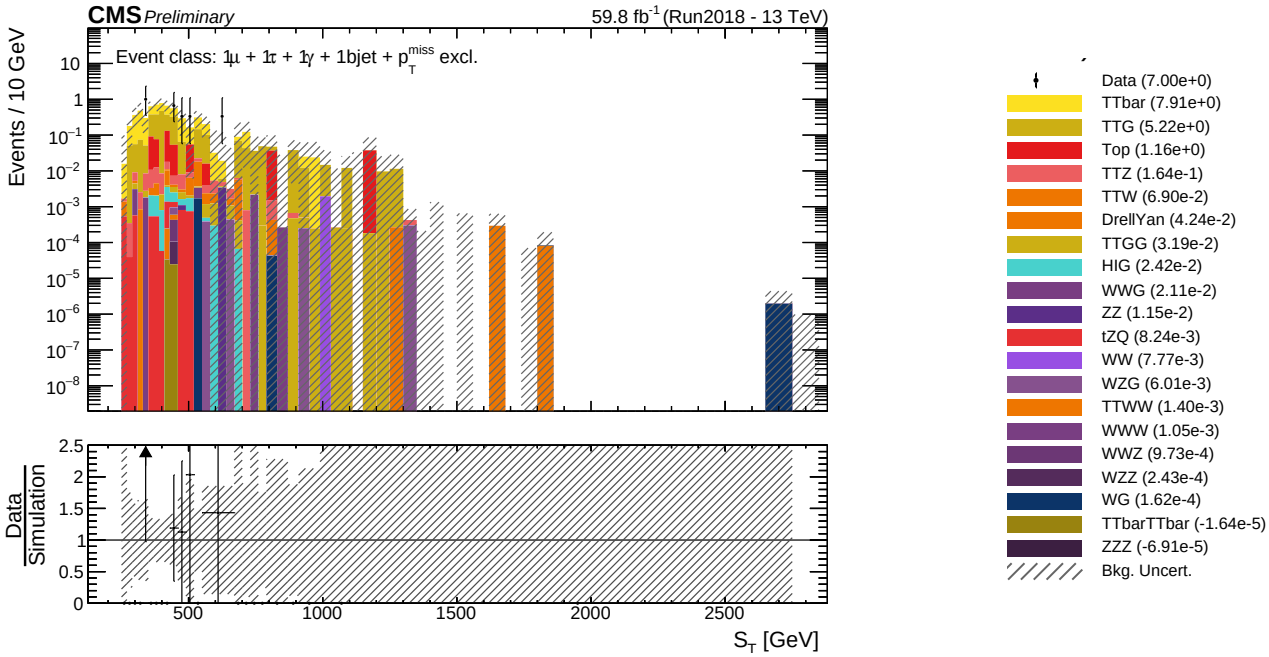

Figure 35: Sum of the transverse momenta distribution of the $1\mu + 1\tau + 1\gamma + 1\text{bjet} + p_T^{miss}$ exclusive event class. The legend is displayed on the right and also shows the total number of counts per process group and Data.

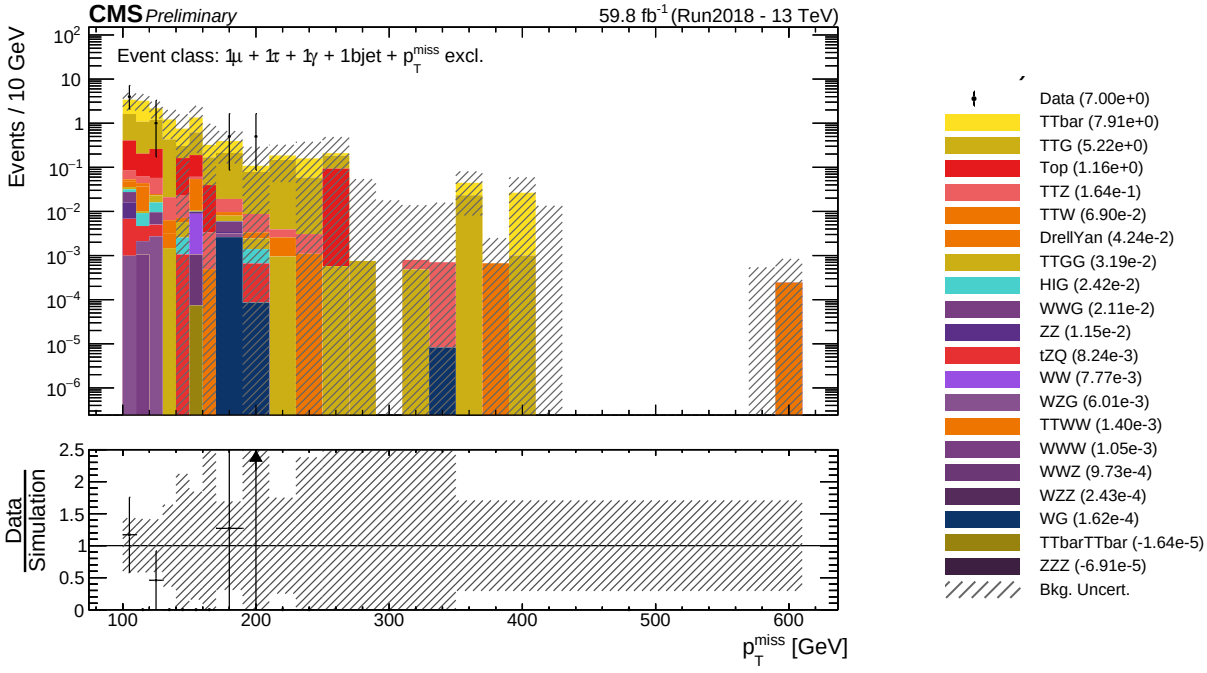

Figure 36: Missing transverse momentum distribution of the $1\mu + 1\tau + 1\gamma + 1\text{bjet} + p_T^{miss}$ exclusive event class. The legend is displayed on the right and also shows the total number of counts per process group and Data.

C.2 Exclusive event class: $1\mu + 2\tau + 3\text{jet} + \mathbf{p_T^{miss}}$

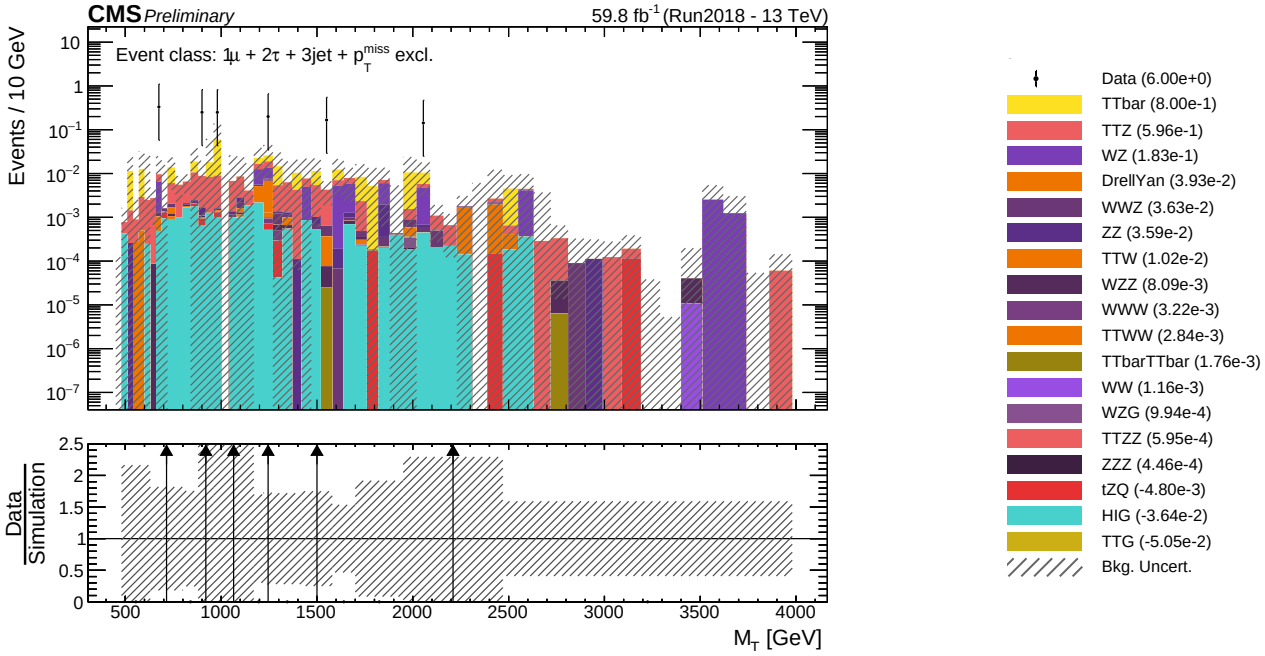

Figure 37: Transverse mass distribution of the $1\mu + 2\tau + 3\text{jet} + p_T^{miss}$ exclusive event class. The legend is displayed on the right and also shows the total number of counts per process group and Data.

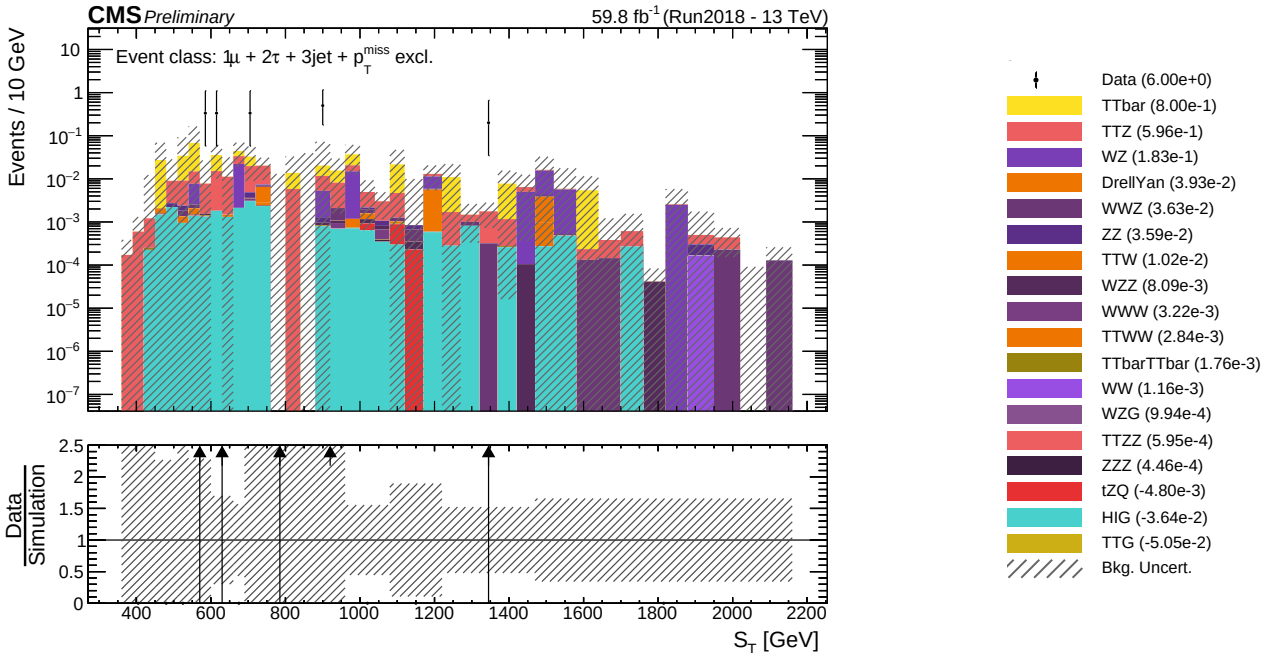

Figure 38: Sum of the transverse momenta distribution of the $1\mu + 2\tau + 3\text{jet} + p_T^{miss}$ exclusive event class. The legend is displayed on the right and also shows the total number of counts per process group and Data.

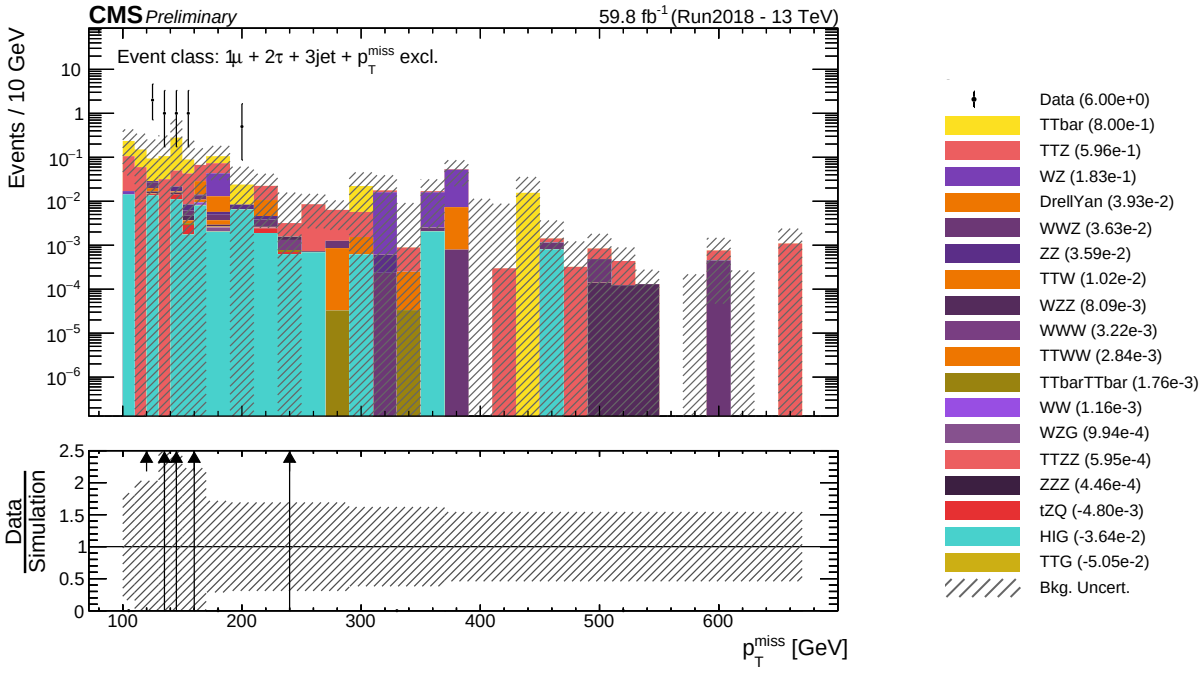

Figure 39: Missing transverse momentum distribution of the $1\mu + 2\tau + 3\text{jet} + p_T^{miss}$ exclusive event class. The legend is displayed on the right and also shows the total number of counts per process group and Data.

C.3 Event classes: $2\mu + 1\tau + 2\text{bjet} + \mathbf{p_T^{miss}}$

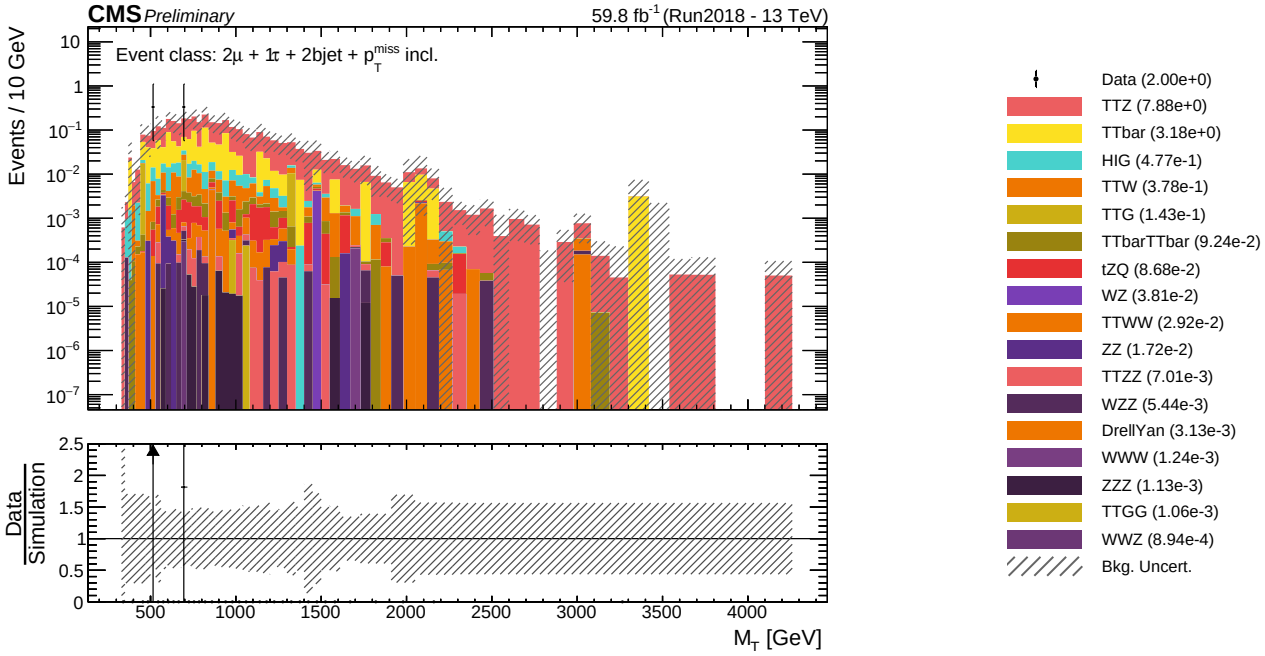

Figure 40: Transverse mass distribution of the $2\mu + 1\tau + 2\text{bjet} + p_T^{miss}$ inclusive event class. The legend is displayed on the right and also shows the total number of counts per process group and Data.

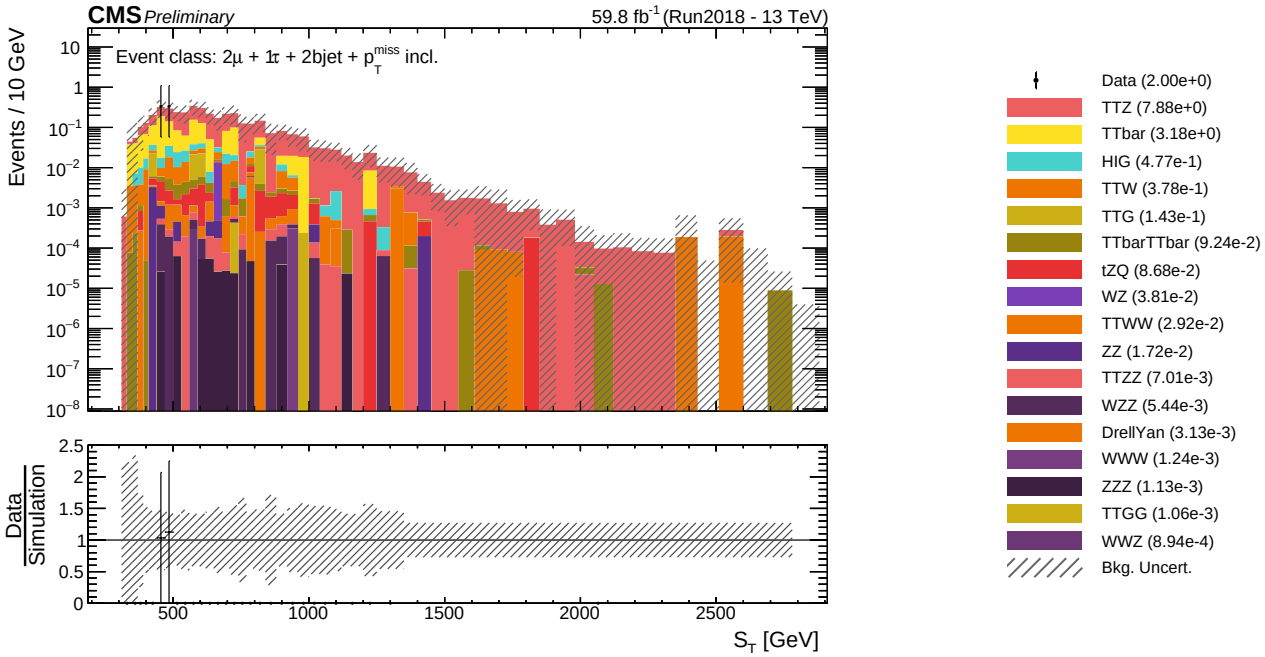

Figure 41: Sum of the transverse momenta distribution of the $2\mu+1\tau+2\text{bjet}+p_T^{miss}$ inclusive event class. The legend is displayed on the right and also shows the total number of counts per process group and Data.

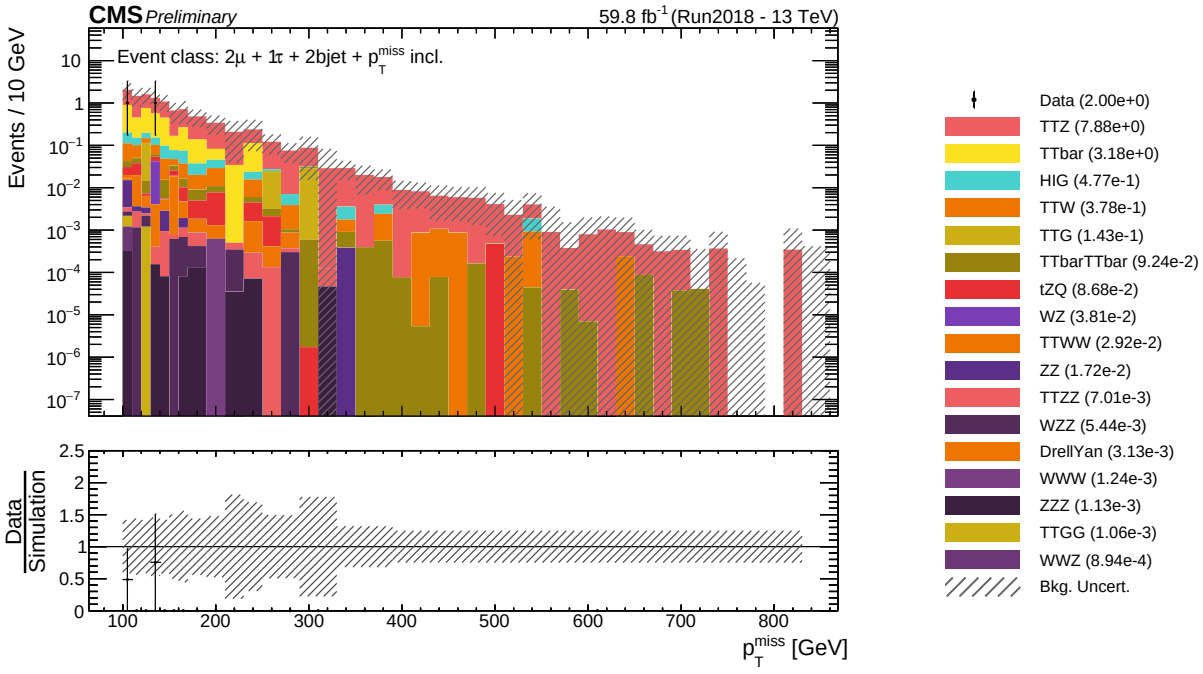

Figure 42: Missing transverse momentum distribution of the $2\mu+1\tau+2\text{bjet}+p_T^{miss}$ inclusive event class. The legend is displayed on the right and also shows the total number of counts per process group and Data.

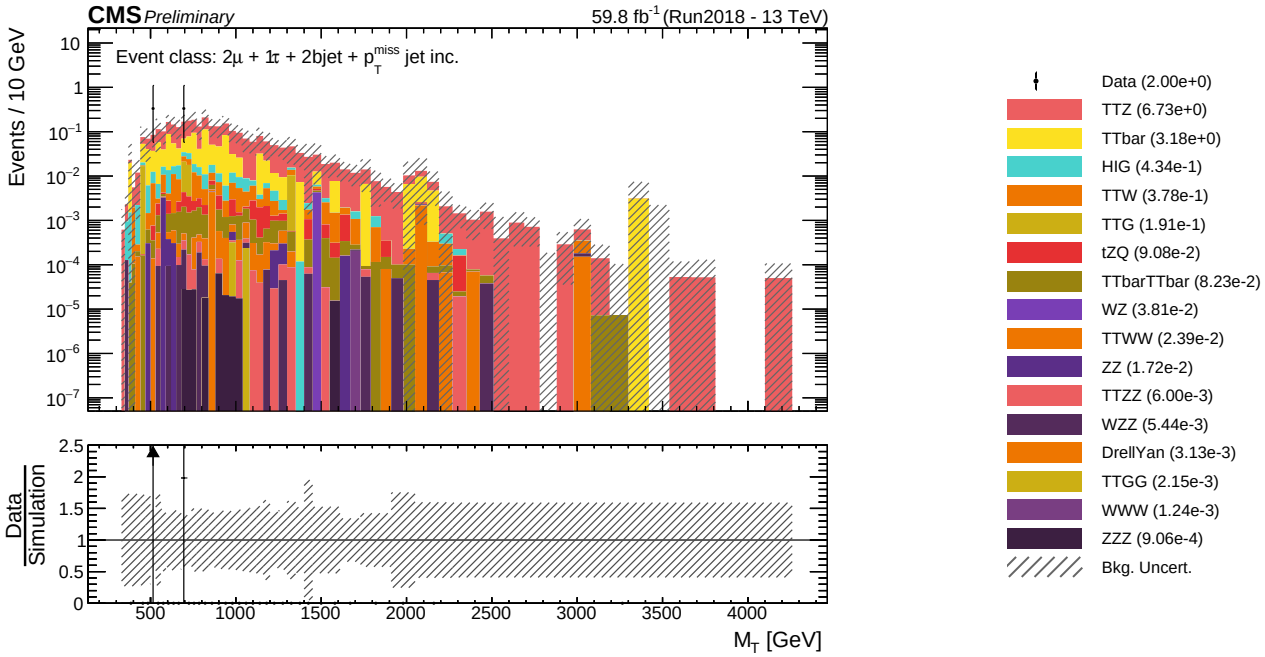

Figure 43: Transverse mass distribution of the $2\mu + 1\tau + 2\text{bjet} + p_T^{miss}$ jet inclusive event class. The legend is displayed on the right and also shows the total number of counts per process group.

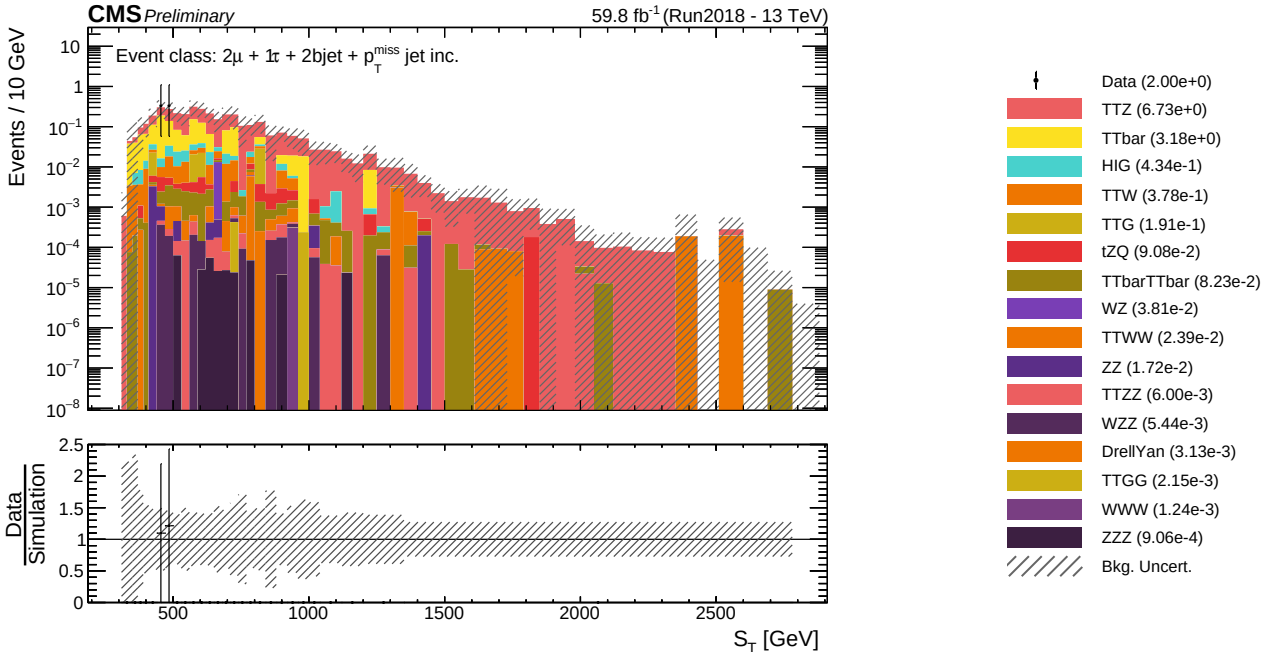

Figure 44: Sum of the transverse momenta distribution of the $2\mu + 1\tau + 2\text{bjet} + p_T^{miss}$ jet inclusive event class. The legend is displayed on the right and also shows the total number of counts per process group.

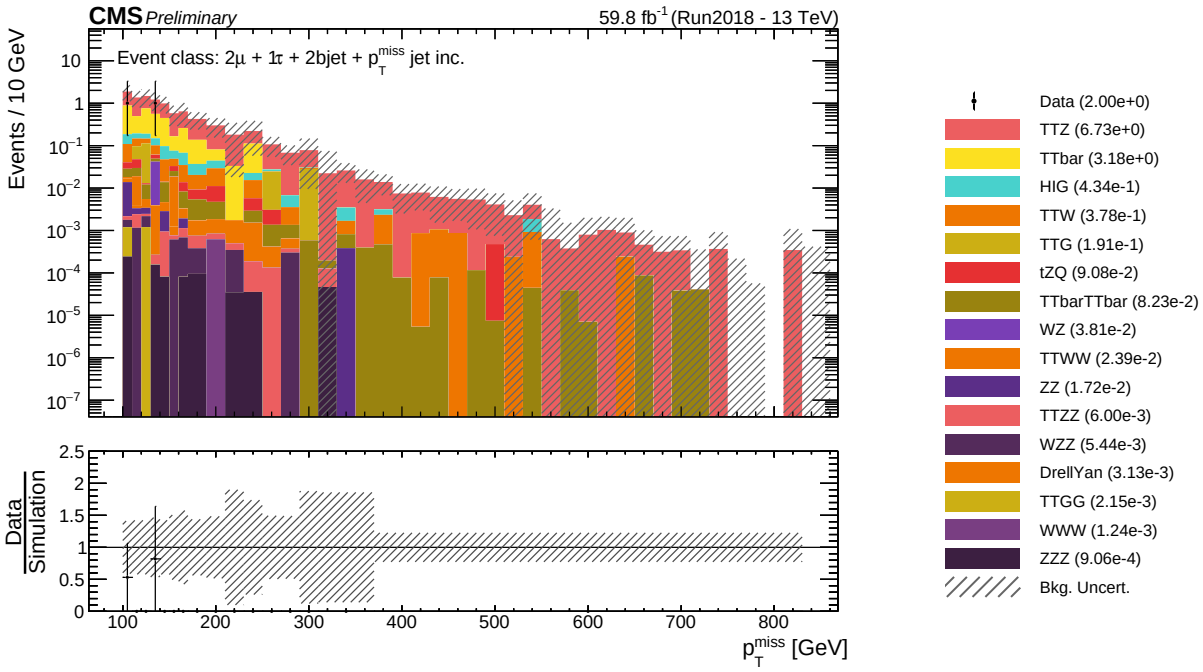

Figure 45: Missing transverse momentum distribution of the $2\mu + 1\tau + 2\text{bjet} + p_T^{miss}$ jet inclusive event class. The legend is displayed on the right and also shows the total number of counts per process group and Data.

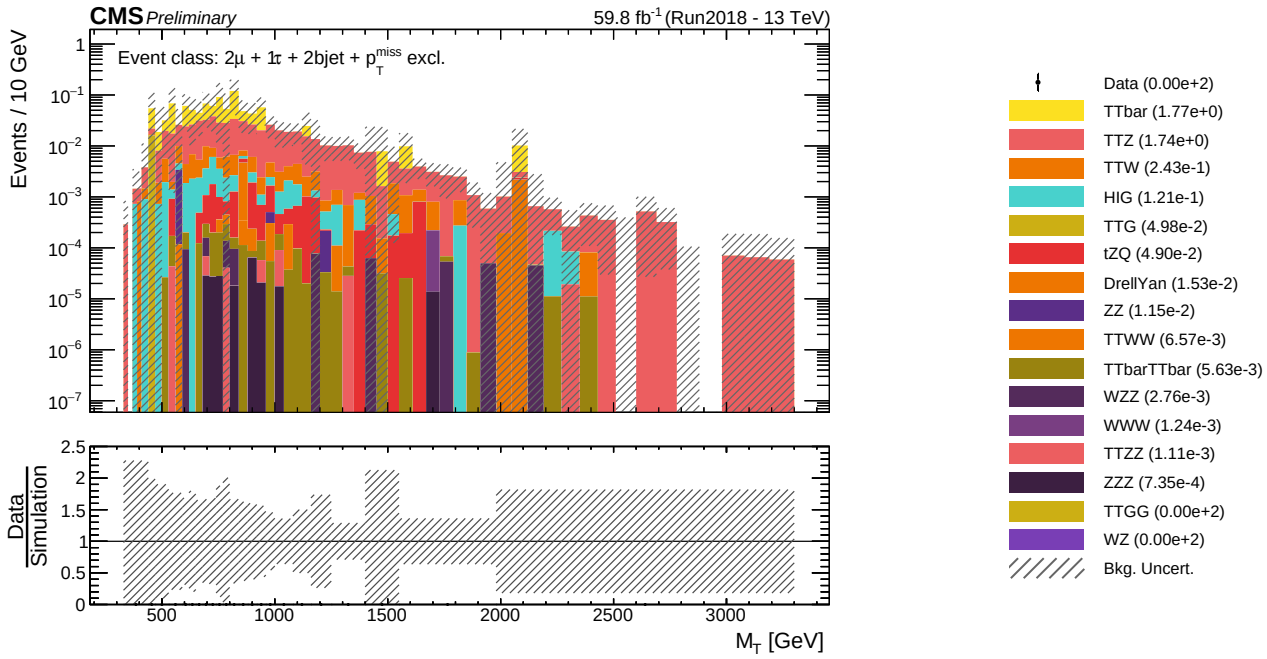

Figure 46: Transverse mass distribution of the $2\mu + 1\tau + 2\text{bjet} + p_T^{miss}$ exclusive event class. The legend is displayed on the right and also shows the total number of counts per process group and Data.

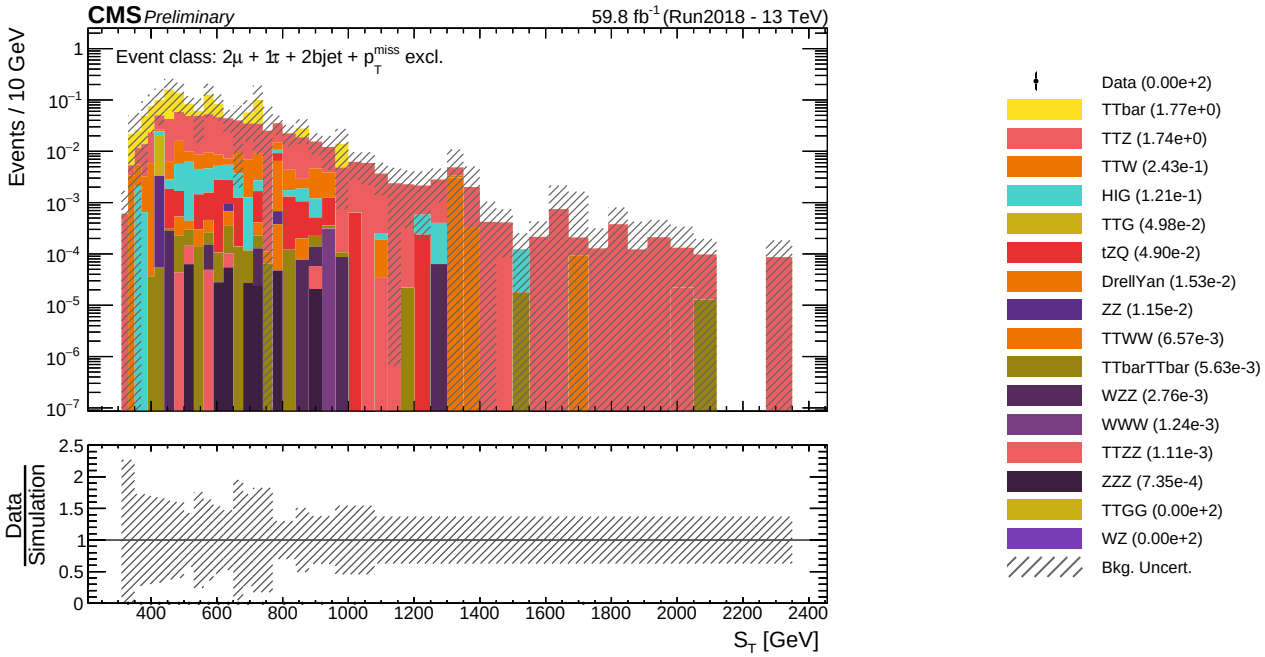

Figure 47: Sum of the transverse momenta distribution of the $2\mu+1\tau+2\text{bjet}+p_T^{miss}$ exclusive event class. The legend is displayed on the right and also shows the total number of counts per process group.

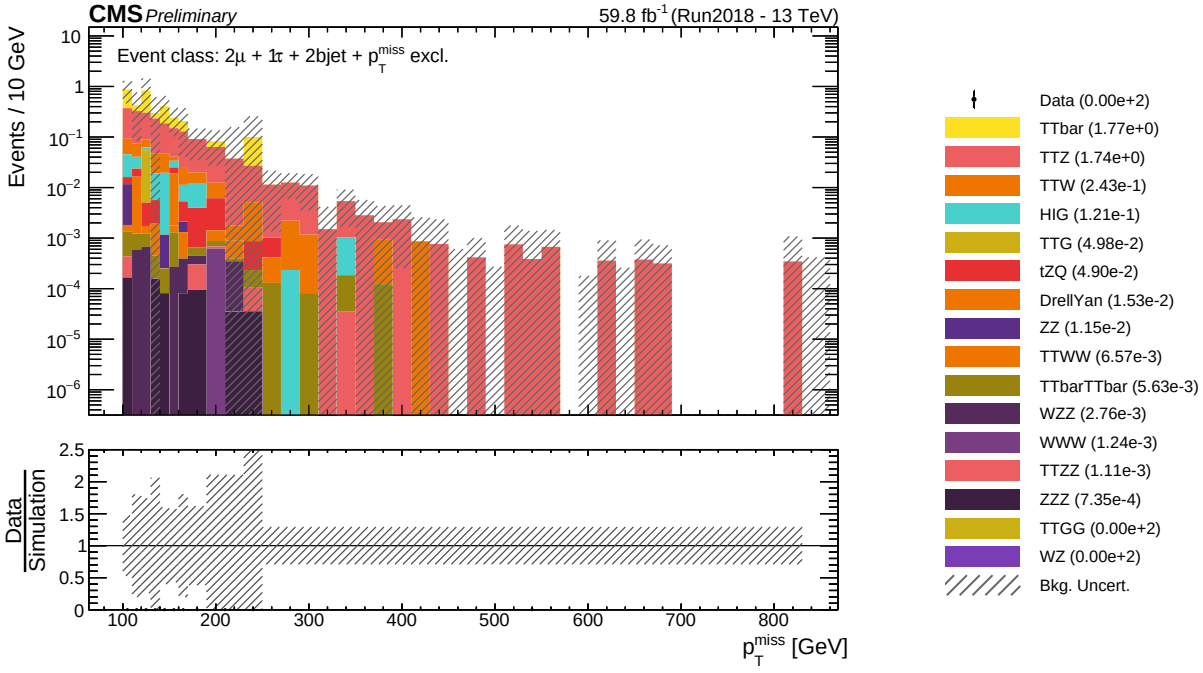

Figure 48: Missing transverse momentum distribution of the $2\mu+1\tau+2\text{bjet}+p_T^{miss}$ exclusive event class. The legend is displayed on the right and also shows the total number of counts per process group.

C.4 Inclusive event class: $1\mu + 1\tau + 1\gamma + 2\text{bjet} + 1\text{jet}$

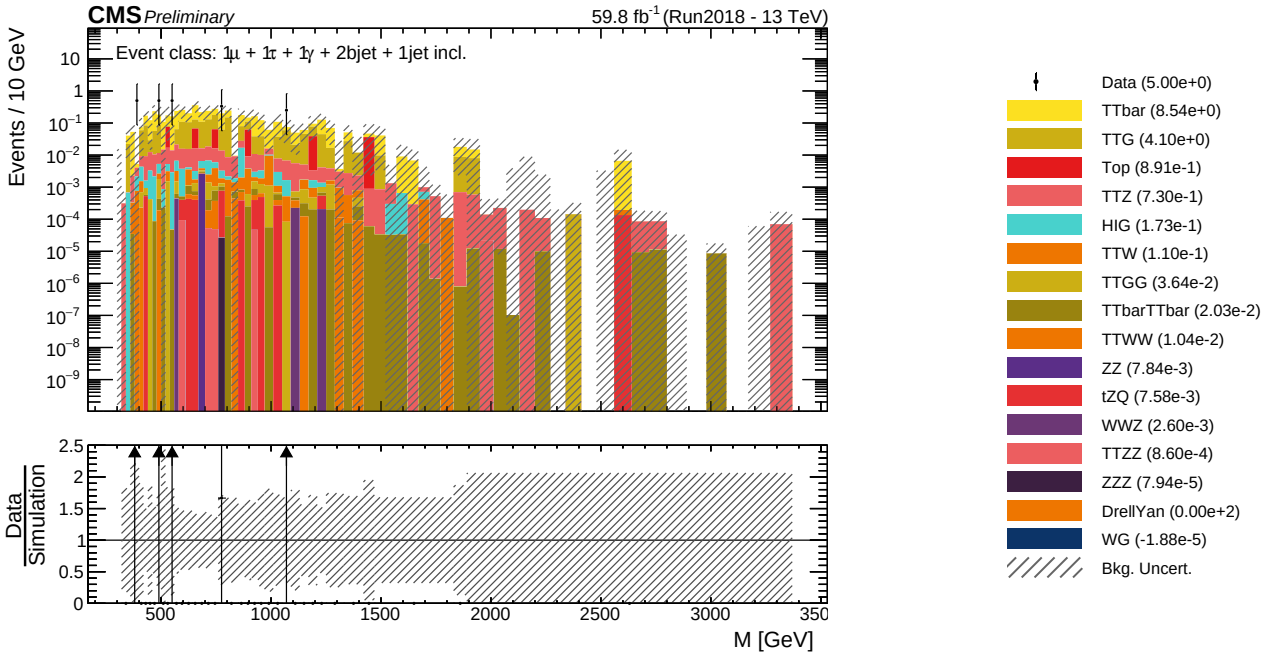

Figure 49: Invariant mass distribution of the $1\mu + 1\tau + 1\gamma + 2\text{bjet} + 1\text{jet}$ inclusive event class. The legend is displayed on the right and also shows the total number of counts per process group and Data.

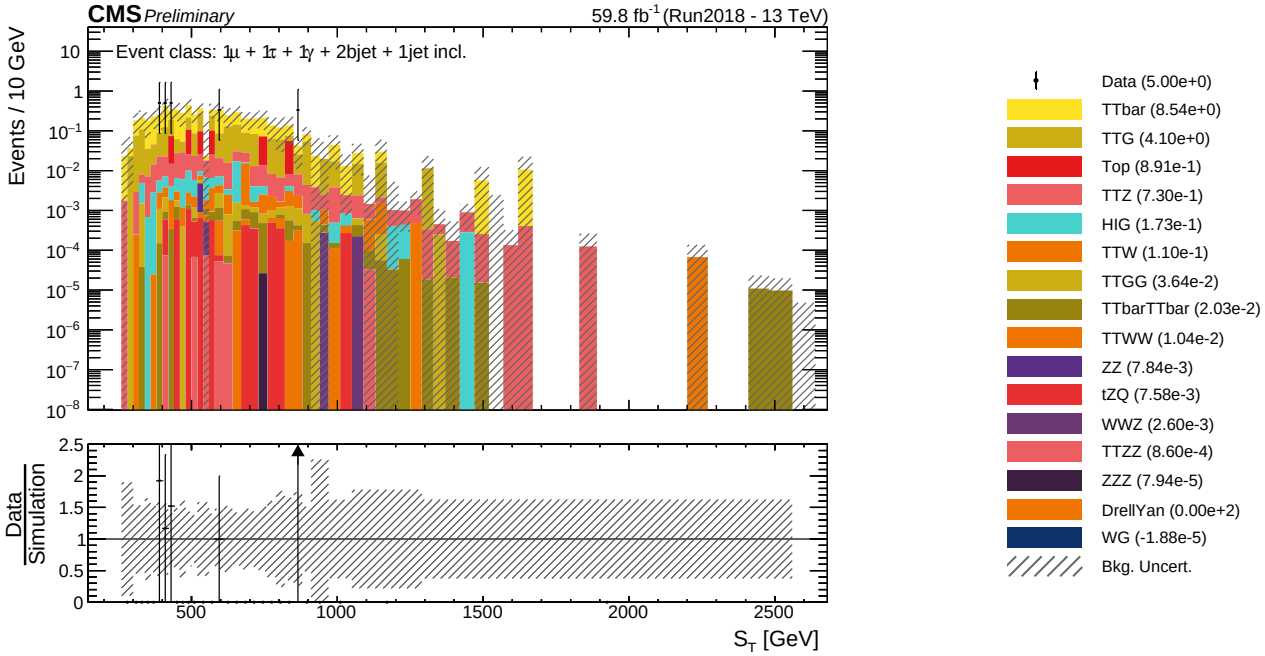

Figure 50: Sum of the transverse momenta distribution of the $1\mu + 1\tau + 1\gamma + 2\text{bjet} + 1\text{jet}$ inclusive event class. The legend is displayed on the right and also shows the total number of counts per process group and Data.

C.5 Event classes: $2\mu + 1\tau + 1\text{bjet} + 2\text{jet} + \mathbf{p_T^{miss}}$

The corresponding jet inclusive event class is the one shown in the main part of the thesis.

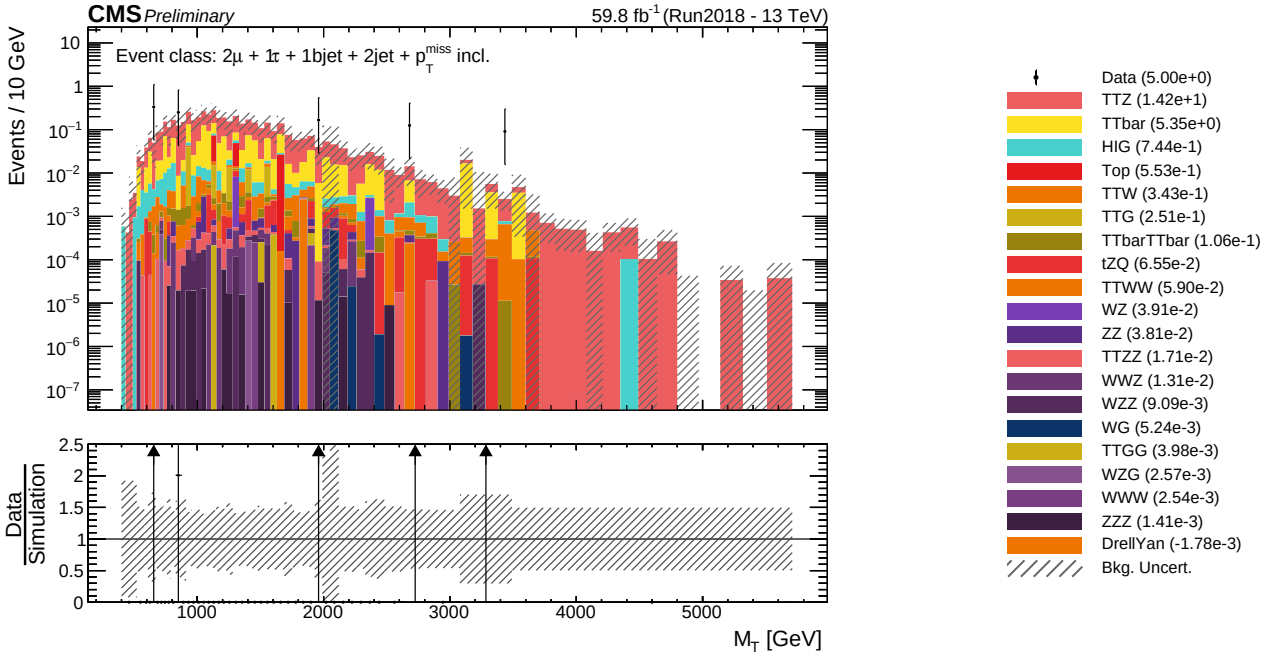

Figure 51: Transverse mass distribution of the $2\mu + 1\tau + 1\text{bjet} + 2\text{jet} + p_T^{miss}$ inclusive event class. The legend is displayed on the right and also shows the total number of counts per process group and Data.

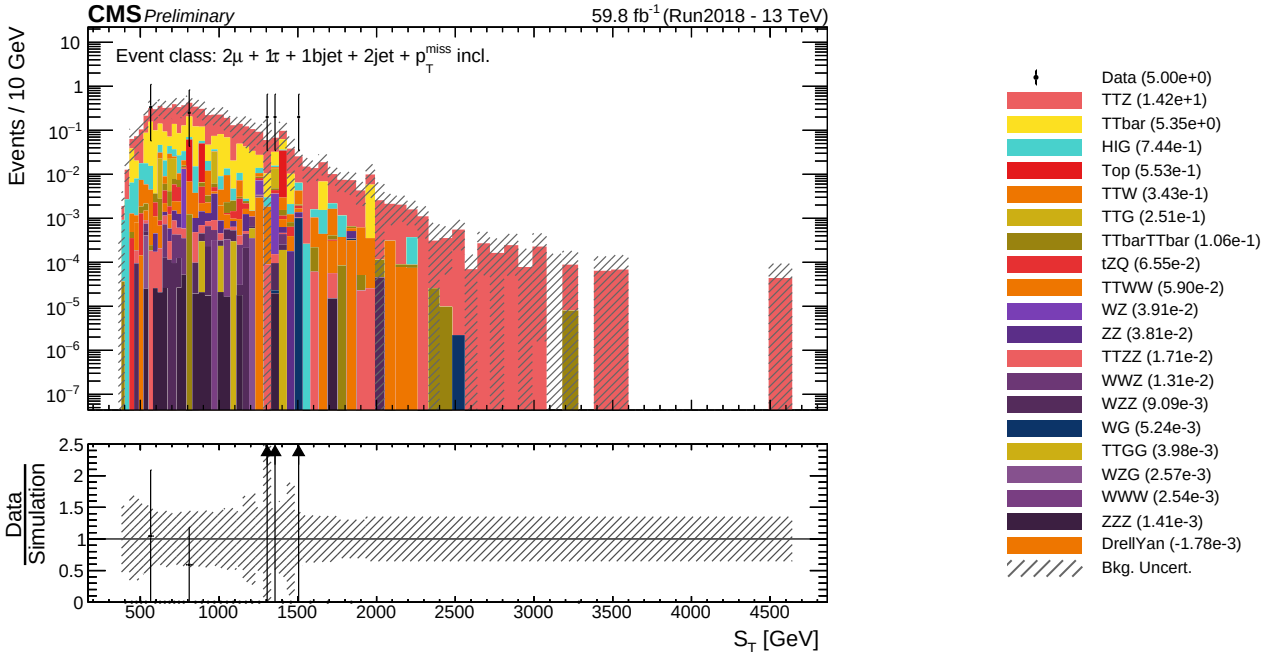

Figure 52: Sum of the transverse momenta distribution of the $2\mu + 1\tau + 1\text{bjet} + 2\text{jet} + p_T^{miss}$ inclusive event class. The legend is displayed on the right and also shows the total number of counts per process group and Data.

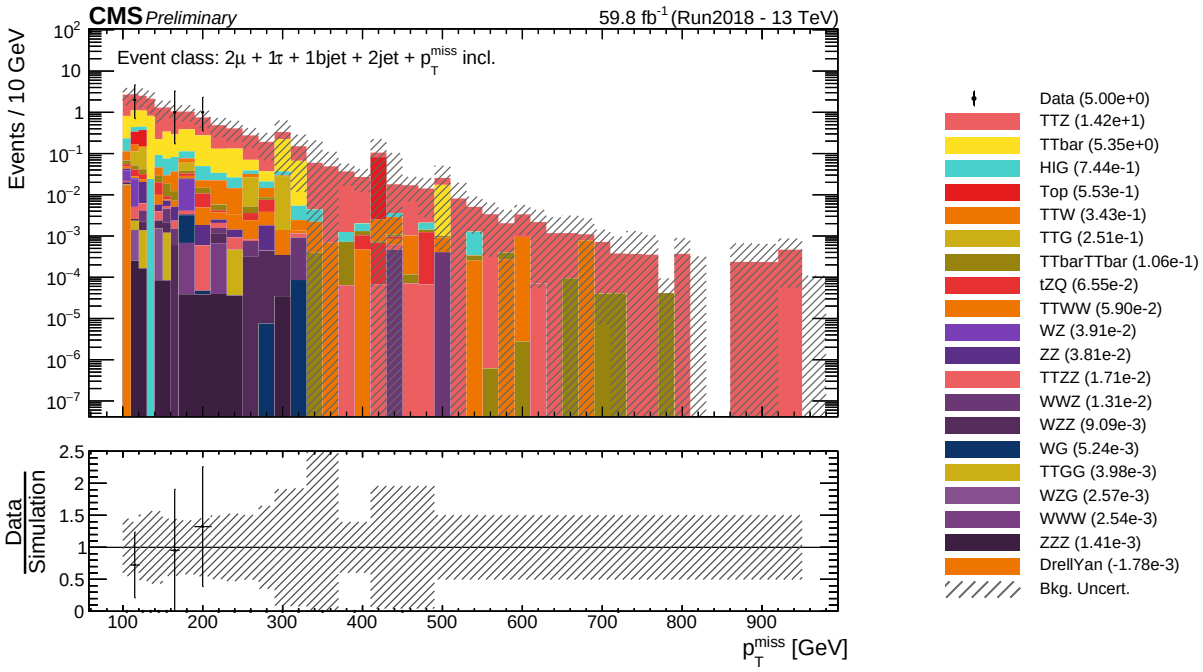

Figure 53: Missing transverse momentum distribution of the $2\mu + 1\tau + 1\text{bjet} + 2\text{jet} + p_T^{miss}$ inclusive event class. The legend is displayed on the right and also shows the total number of counts per process group and Data.

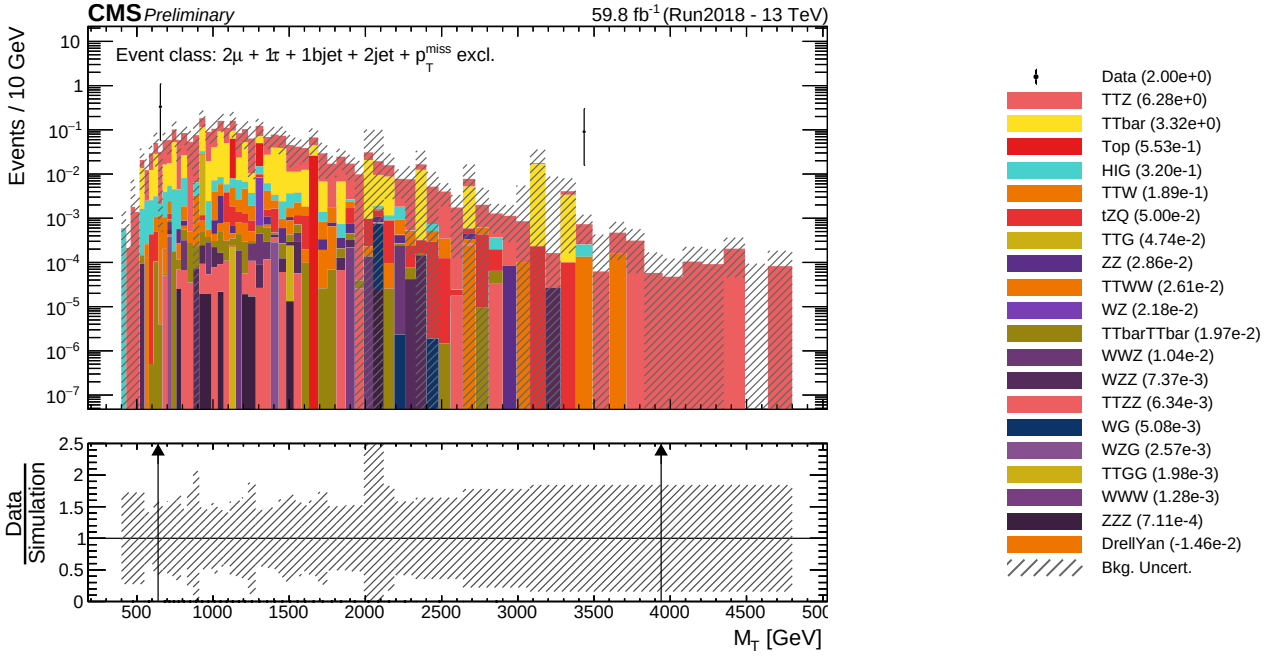

Figure 54: Transverse mass distribution of the $2\mu + 1\tau + 1\text{bjet} + 2\text{jet} + p_T^{miss}$ exclusive event class. The legend is displayed on the right and also shows the total number of counts per process group and Data.

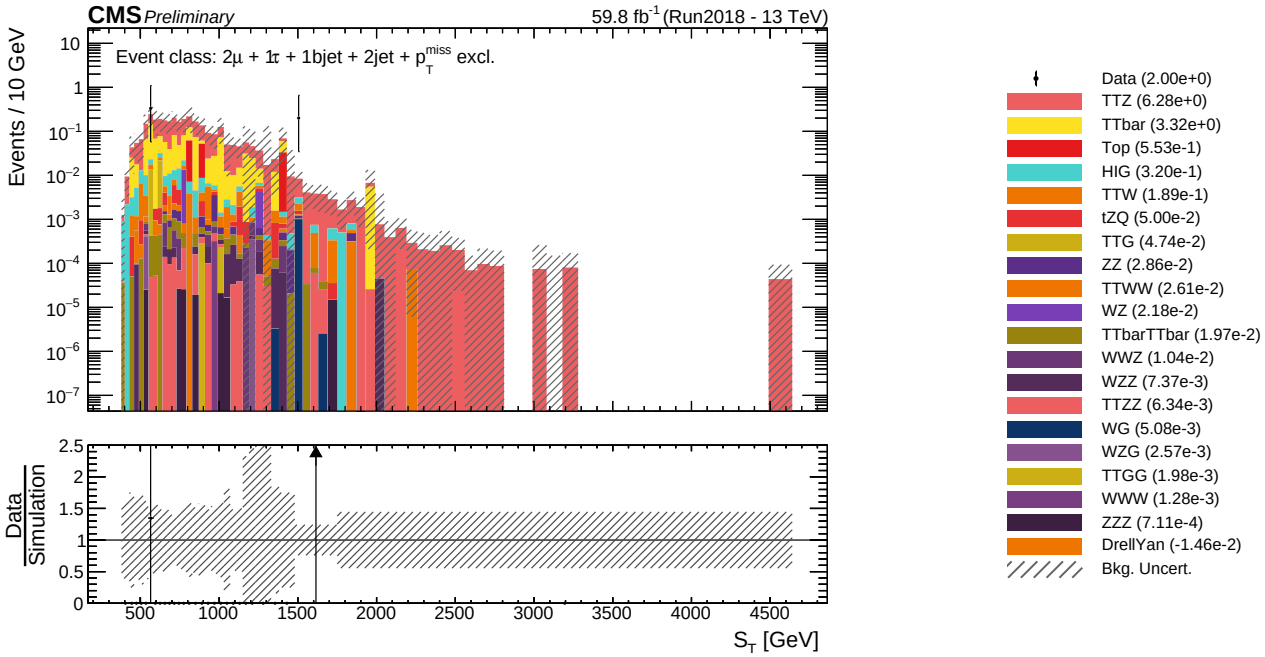

Figure 55: Sum of the transverse momenta distribution of the $2\mu + 1\tau + 1\text{bjet} + 2\text{jet} + p_T^{miss}$ exclusive event class. The legend is displayed on the right and also shows the total number of counts per process group and Data.

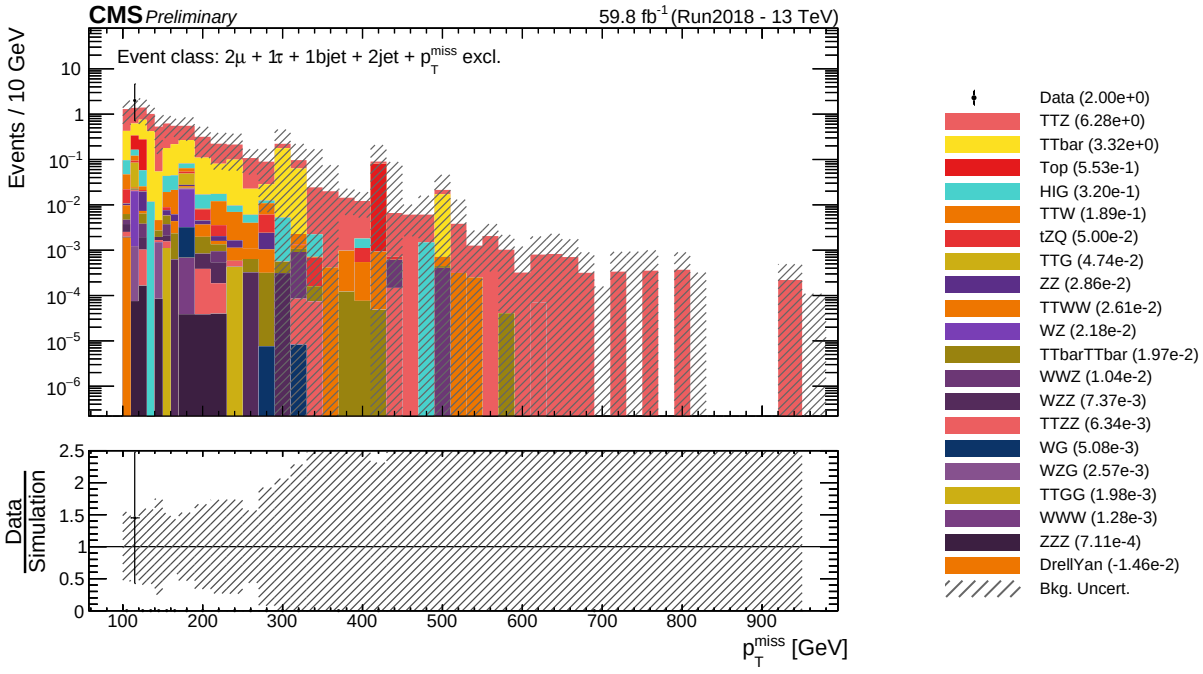

Figure 56: Missing transverse momentum distribution of the $2\mu + 1\tau + 1\text{bjet} + 2\text{jet} + p_T^{miss}$ exclusive event class. The legend is displayed on the right and also shows the total number of counts per process group and Data.

C.6 Inclusive event class: $1\mu + 1\tau + 1\gamma + 1$bjet

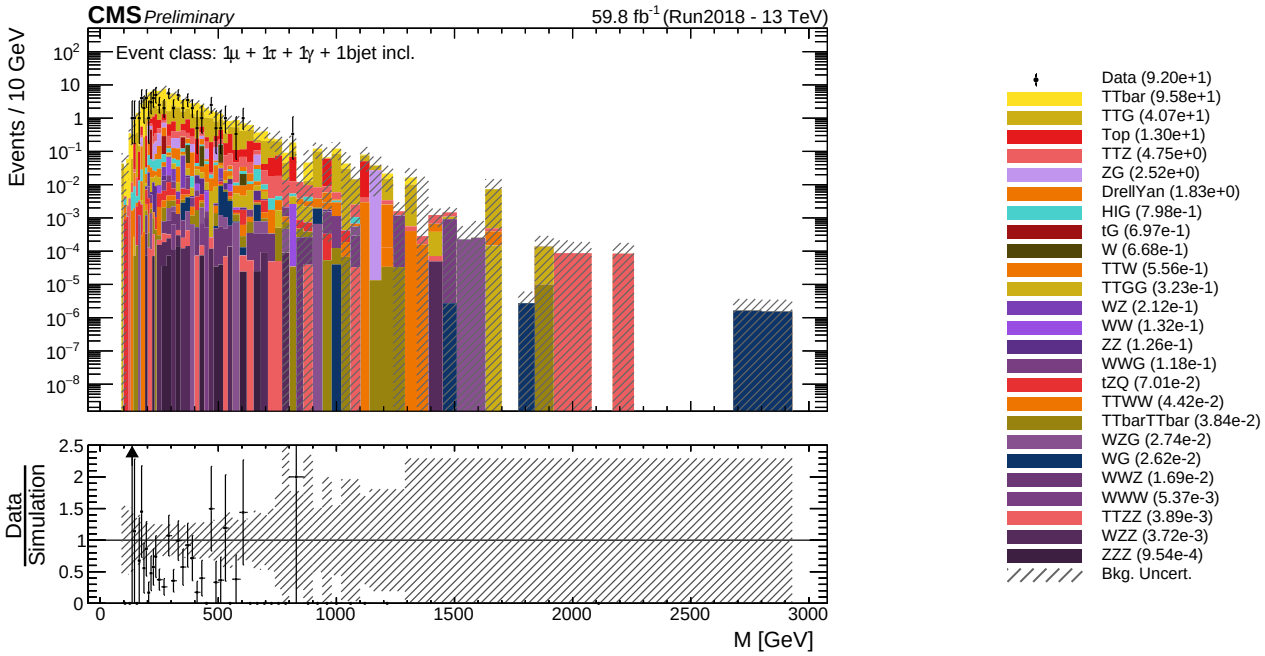

Figure 57: Invariant mass distribution of the $1\mu + 1\tau + 1\gamma + 1$bjet inclusive event class. The legend is displayed on the right and also shows the total number of counts per process group and Data.

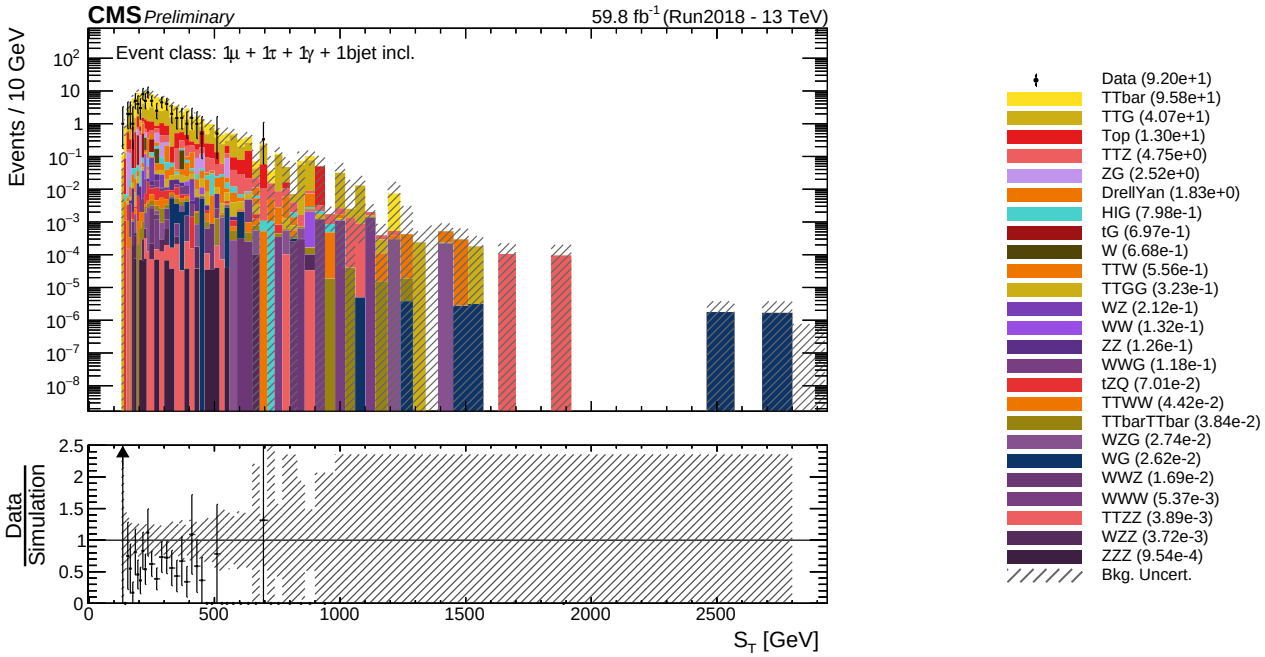

Figure 58: Sum of the transverse momenta distribution of the $1\mu + 1\tau + 1\gamma + 1$bjet inclusive event class. The legend is displayed on the right and also shows the total number of counts per process group and Data.

D Additional plots of the sensitivity study

D.1 Excited taus with a low mass

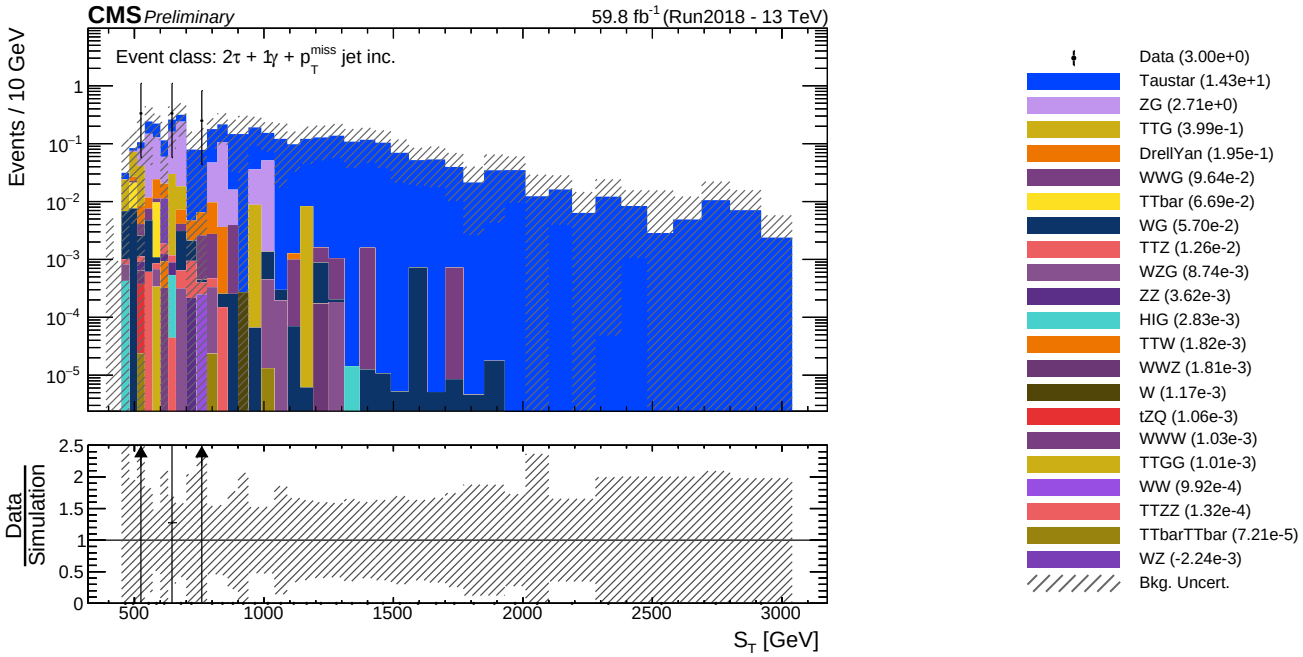

Figure 59: Sum of the transverse momenta distribution of the $2\tau + 1\gamma + p_T^{miss}$ jet inclusive event class when the signal ($m_{\tau^*} = 175\,\text{GeV}$ and $\Lambda = 10\,\text{TeV}$) is included. The legend is displayed on the right and also shows the total number of counts per process group and Data. The signal process group is called "Taustar".

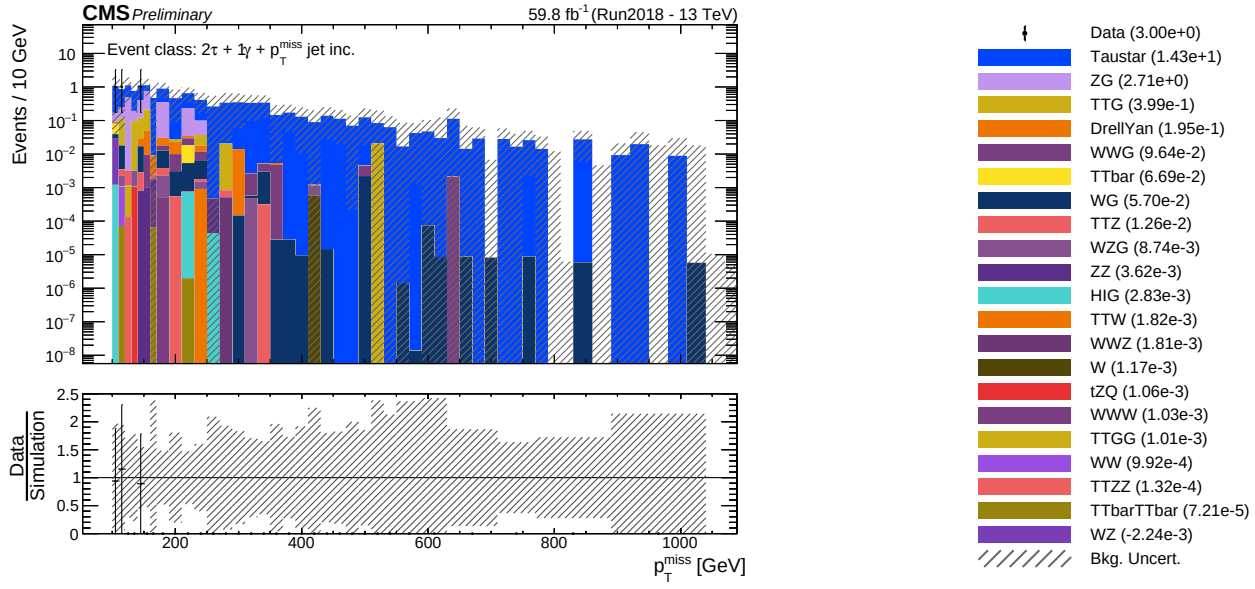

Figure 60: Missing transverse momentum distribution of the $2\tau + 1\gamma + p_T^{miss}$ jet inclusive event class when the signal ($m_{\tau^*} = 175\,\text{GeV}$ and $\Lambda = 10\,\text{TeV}$) is included. The legend is displayed on the right and also shows the total number of counts per process group and Data. The signal process group is called "Taustar".

D.2 Sensitivity to higher masses

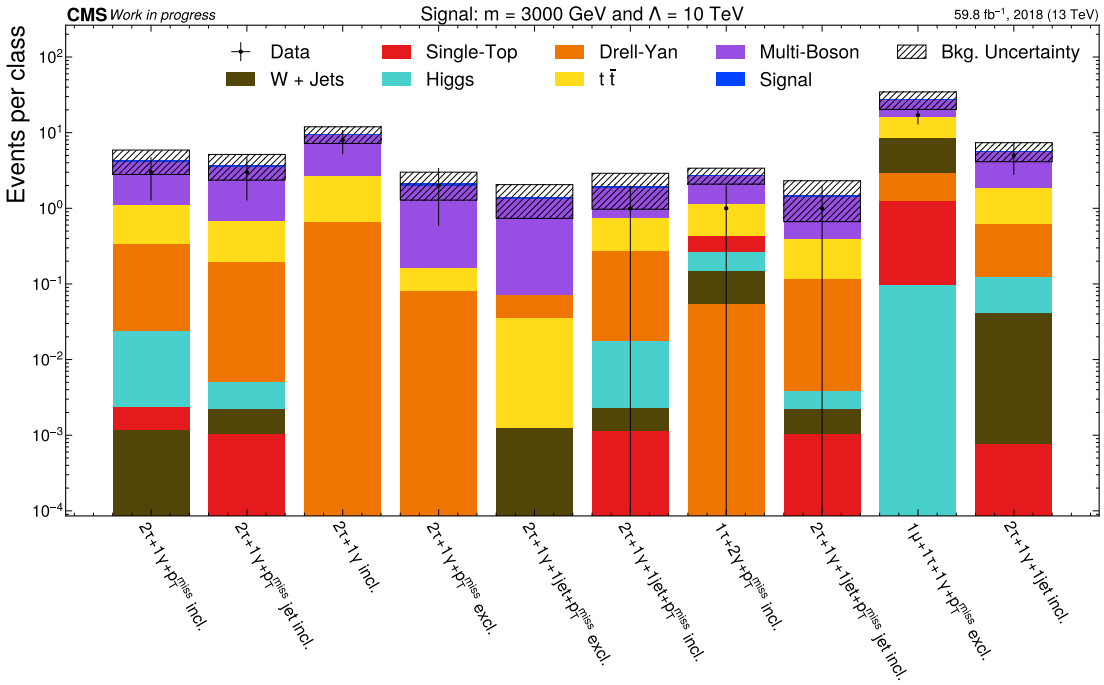

Figure 61: This plot shows the MC yield of the event classes, with the most decreasing p-value when the signal with a mass of 3000 GeV and $\Lambda = 10$ TeV is included.

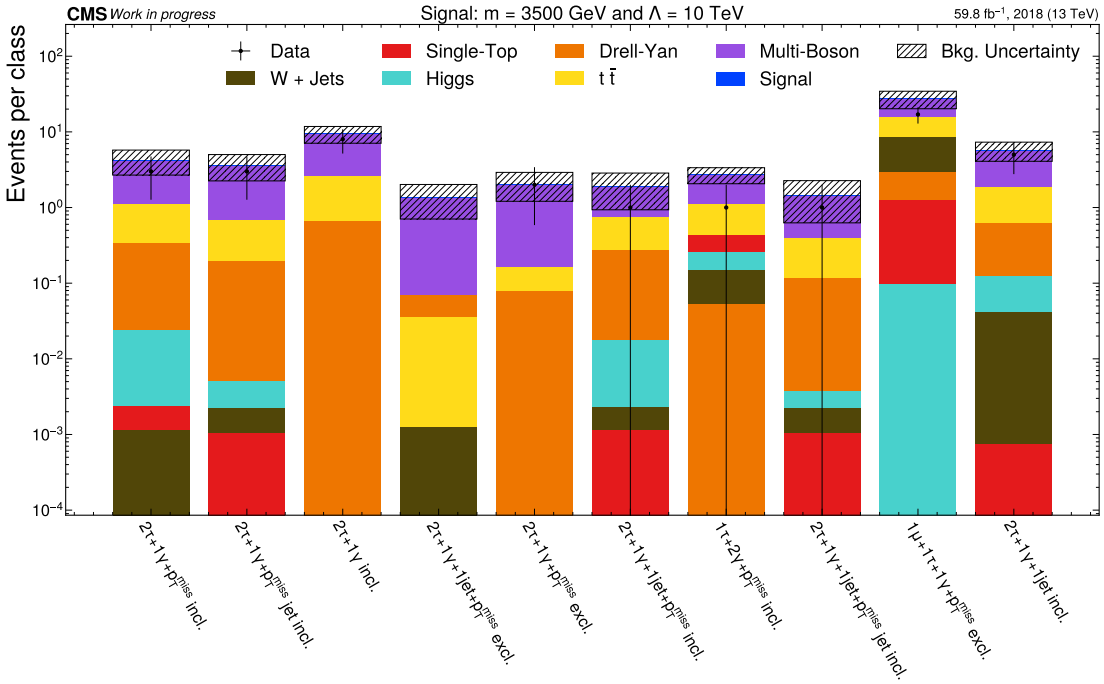

Figure 62: This plot shows the MC yield of the event classes, with the most decreasing p-value when the signal with a mass of 3500 GeV and $\Lambda = 10$ TeV is included.

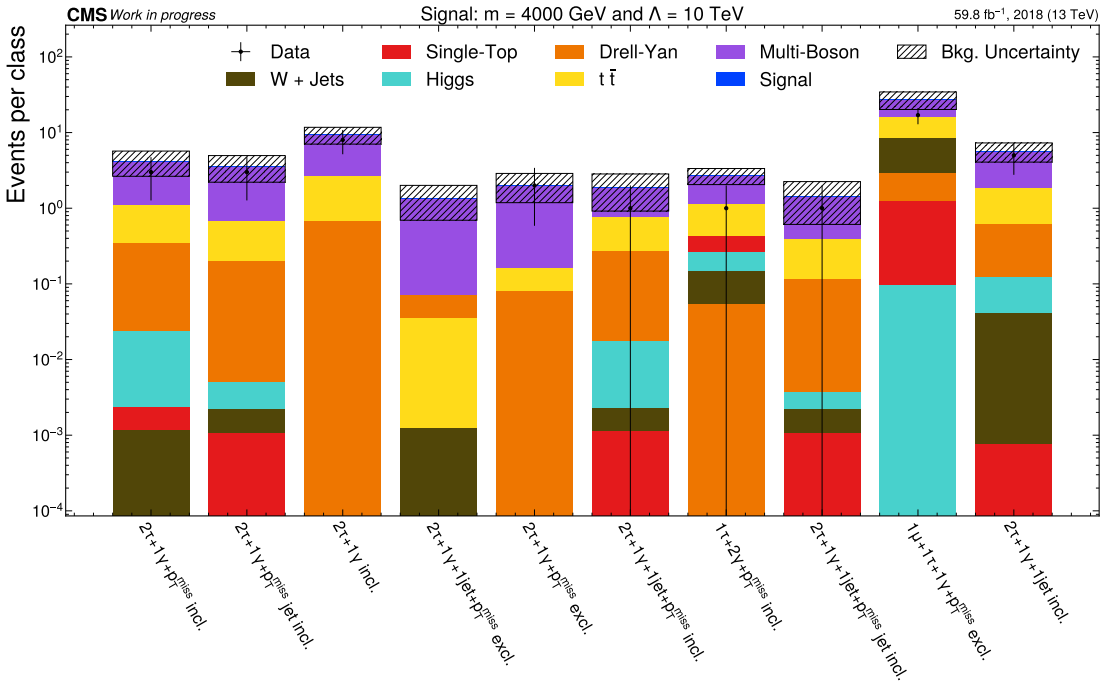

Figure 63: This plot shows the MC yield of the event classes, with the most decreasing p-value when the signal with a mass of 4000 GeV and $\Lambda = 10$ TeV is included.

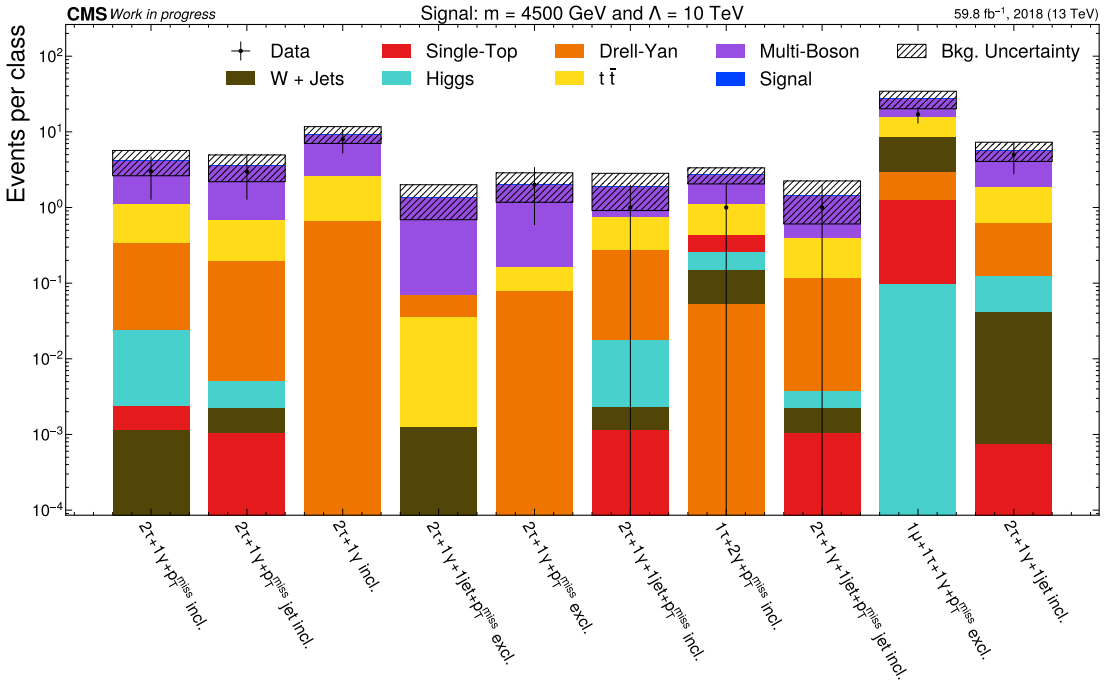

Figure 64: This plot shows the MC yield of the event classes, with the most decreasing p-value when the signal with a mass of 4500 GeV and $\Lambda = 10$ TeV is included.

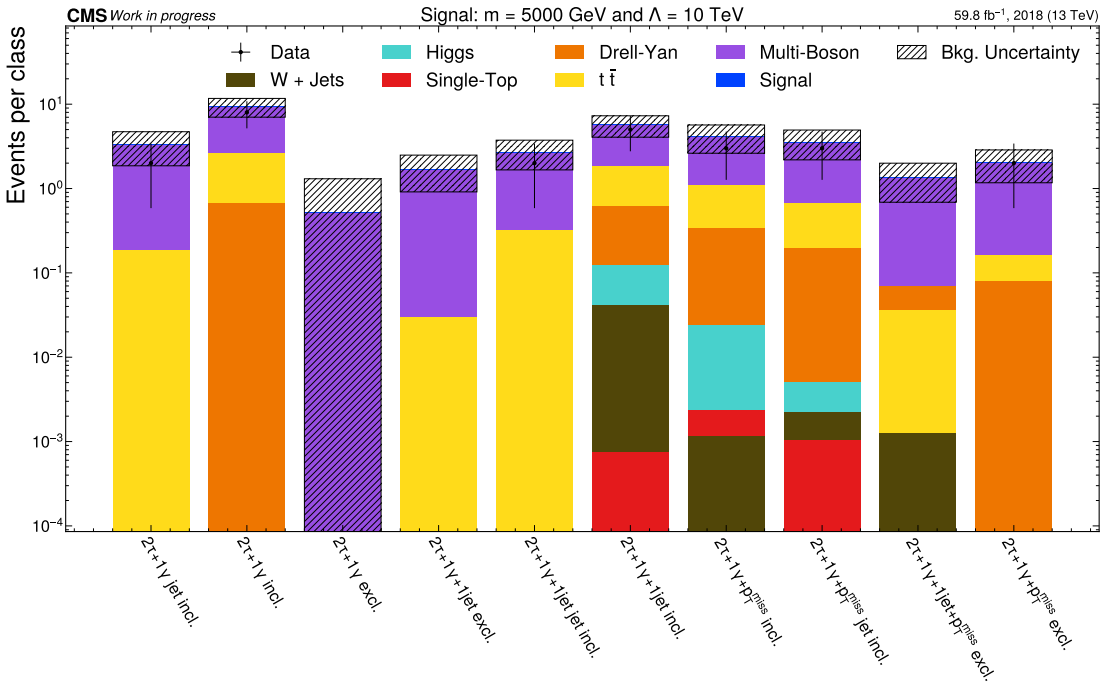

Figure 65: This plot shows the MC yield of the event classes, with the most decreasing p-value when the signal with a mass of 5000 GeV and $\Lambda = 10$ TeV is included.

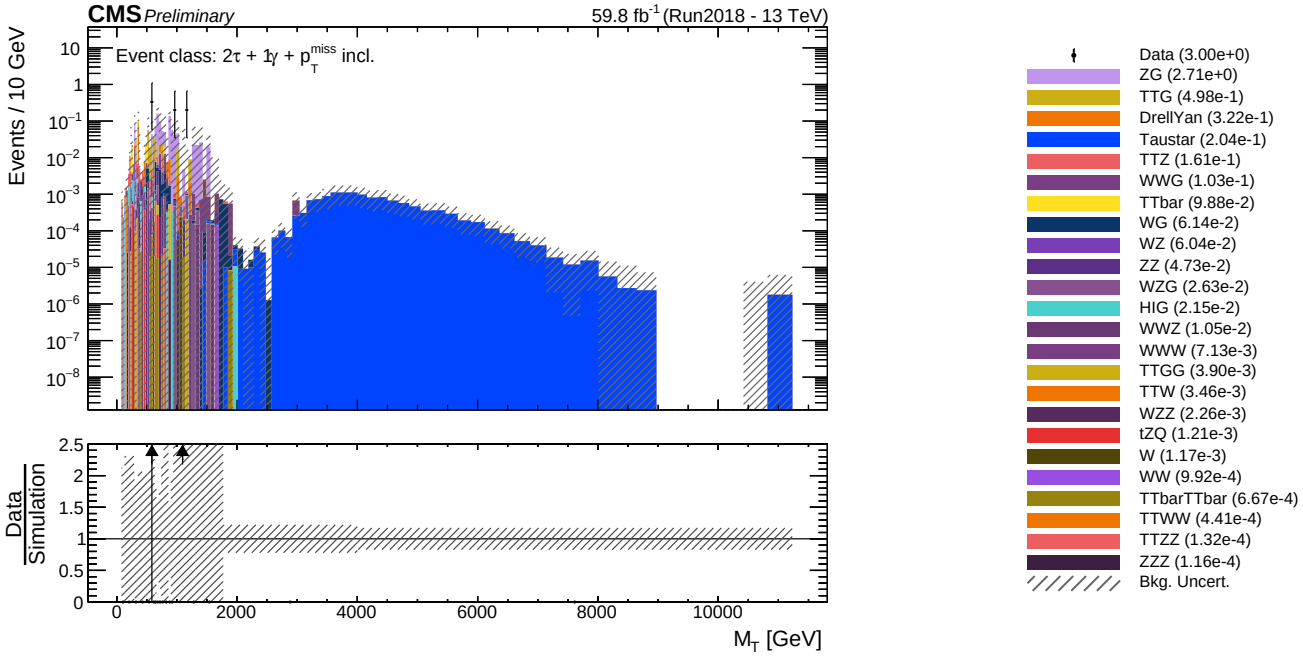

Figure 66: Transverse mass distribution of the $2\tau + 1\gamma + p_T^{miss}$ inclusive event class when the signal ($m_{\tau^*} = 3000$ GeV and $\Lambda = 10$ TeV) is included. The legend is displayed on the right and also shows the total number of counts per process group and Data. The signal process group is called "Taustar".

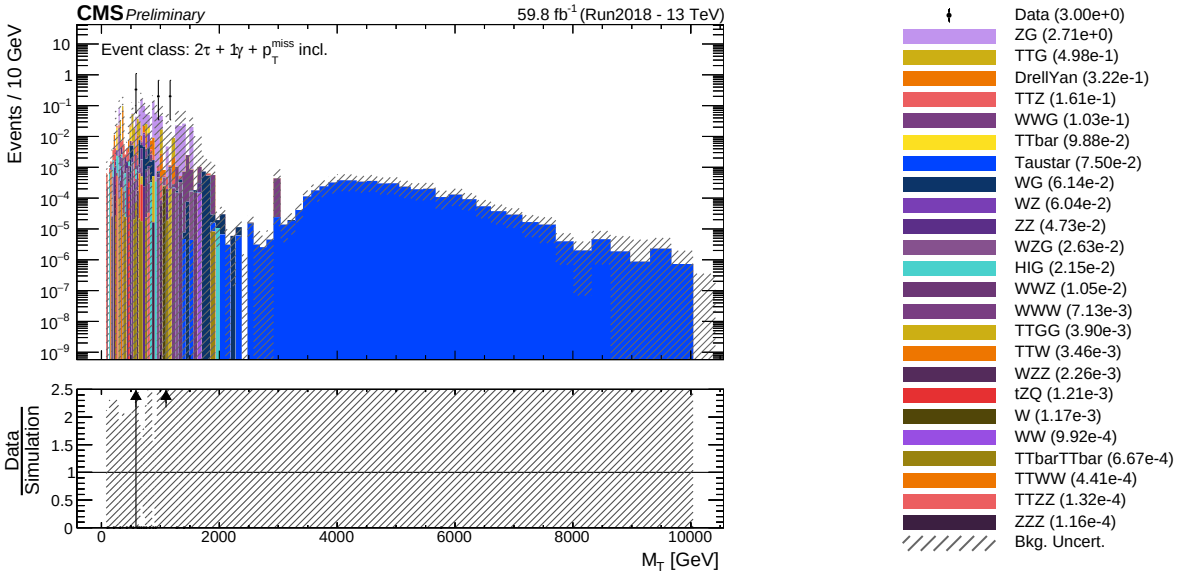

Figure 67: Transverse mass distribution of the $2\tau + 1\gamma + p_T^{miss}$ inclusive event class when the signal ($m_{\tau^*} = 3500\,\text{GeV}$ and $\Lambda = 10\,\text{TeV}$) is included. The legend is displayed on the right and also shows the total number of counts per process group and Data. The signal process group is called "Taustar".

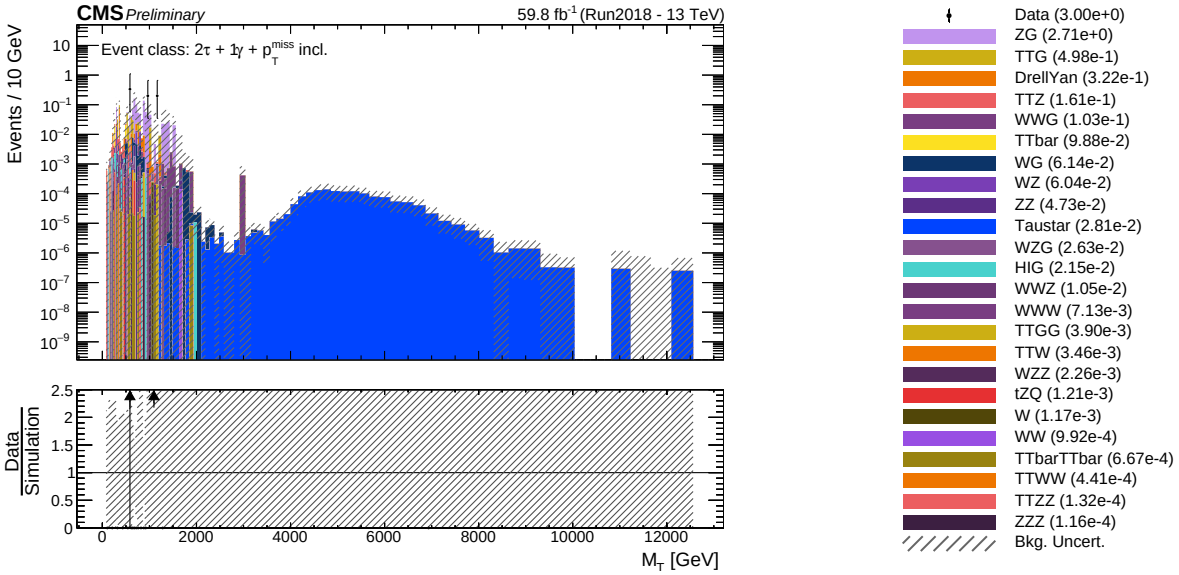

Figure 68: Transverse mass distribution of the $2\tau + 1\gamma + p_T^{miss}$ inclusive event class when the signal ($m_{\tau^*} = 4000\,\text{GeV}$ and $\Lambda = 10\,\text{TeV}$) is included. The legend is displayed on the right and also shows the total number of counts per process group and Data. The signal process group is called "Taustar".

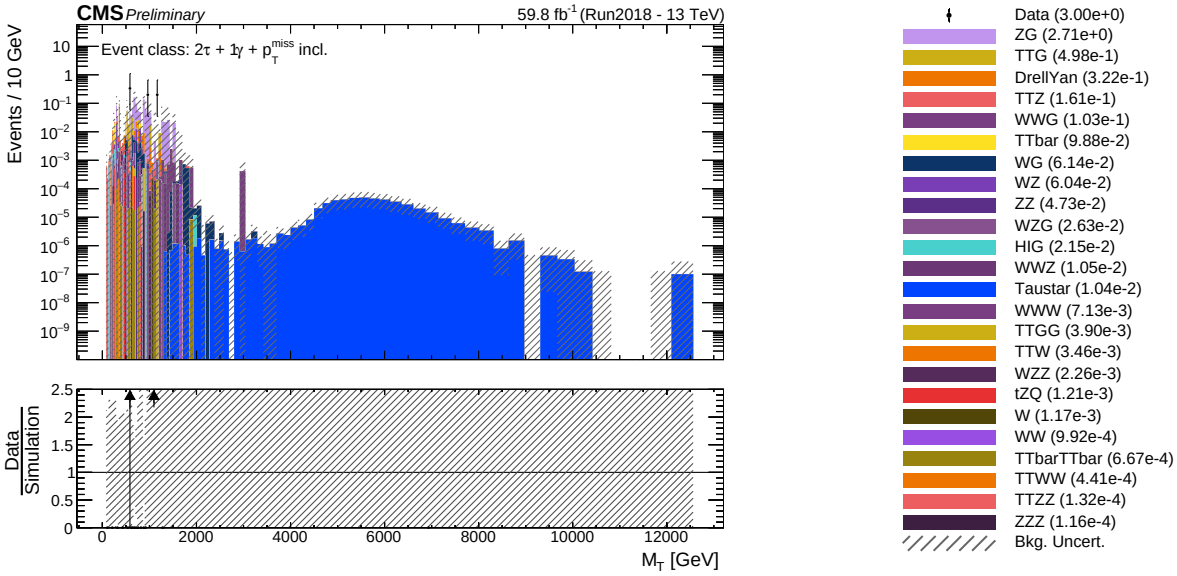

Figure 69: Transverse mass distribution of the $2\tau + 1\gamma + p_T^{miss}$ inclusive event class when the signal ($m_{\tau^*} = 4500\,\text{GeV}$ and $\Lambda = 10\,\text{TeV}$) is included. The legend is displayed on the right and also shows the total number of counts per process group and Data. The signal process group is called "Taustar".

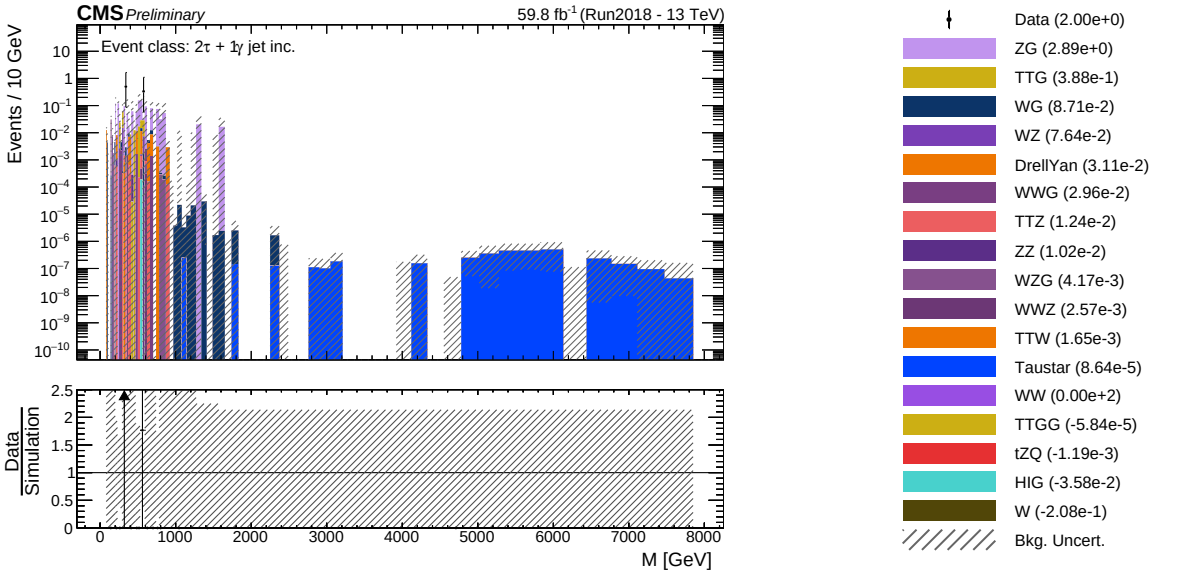

Figure 70: Invariant mass distribution of the $2\tau + 1\gamma$ jet inclusive event class when the signal ($m_{\tau^*} = 5000\,\text{GeV}$ and $\Lambda = 10\,\text{TeV}$) is included. The legend is displayed on the right and also shows the total number of counts per process group and Data. The signal process group is called "Taustar".

E Resulting p-values for higher masses of the signal

This section shows for further regarded mass of the τ^* the 10 classes with the most decreasing p-value.

event class	p^{signal}-value	p^{data}-value	δp [%]
$2\tau + 1\gamma + p_T^{miss} + \mathrm{X}$	0.432	0.443	−2.61
$2\tau + 1\gamma + p_T^{miss} + \mathrm{NJet}$	0.525	0.537	−2.28
$2\tau + 1\gamma + \mathrm{X}$	0.433	0.441	−1.76
$2\tau + 1\gamma + 1\mathrm{Jet} + p_T^{miss}$	0.299	0.304	−1.58
$2\tau + 1\gamma + p_T^{miss}$	0.654	0.664	−1.54
$2\tau + 1\gamma + 1\mathrm{Jet} + p_T^{miss} + \mathrm{X}$	0.463	0.469	−1.31
$1\tau + 2\gamma + p_T^{miss} + \mathrm{X}$	0.270	0.273	−1.18
$2\tau + 1\gamma + 1\mathrm{Jet} + p_T^{miss} + \mathrm{NJet}$	0.575	0.581	−1.13
$1\mu + 1\tau + 1\gamma + p_T^{miss}$	0.130	0.131	−0.83
$2\tau + 1\gamma + 1\mathrm{Jet} + \mathrm{X}$	0.511	0.515	−0.76

Table 14: These are the classes with the most decreasing p-value when the signal with a τ^* mass of 3500 GeV and $\Lambda = 10$ TeV is included.

event class	p^{signal}-value	p^{data}-value	δp [%]
$2\tau + 1\gamma + p_T^{miss} + \mathrm{X}$	0.439	0.443	−0.98
$2\tau + 1\gamma + p_T^{miss} + \mathrm{NJet}$	0.533	0.537	−0.85
$2\tau + 1\gamma + \mathrm{X}$	0.438	0.441	−0.66
$2\tau + 1\gamma + 1\mathrm{Jet} + p_T^{miss}$	0.302	0.304	−0.59
$2\tau + 1\gamma + p_T^{miss}$	0.660	0.664	−0.59
$2\tau + 1\gamma + 1\mathrm{Jet} + p_T^{miss} + \mathrm{X}$	0.467	0.469	−0.5
$1\tau + 2\gamma + p_T^{miss} + \mathrm{X}$	0.272	0.273	−0.45
$2\tau + 1\gamma + 1\mathrm{Jet} + p_T^{miss} + \mathrm{NJet}$	0.580	0.581	−0.41
$1\mu + 1\tau + 1\gamma + p_T^{miss}$	0.131	0.131	−0.31
$2\tau + 1\gamma + 1\mathrm{Jet} + \mathrm{X}$	0.513	0.515	−0.27

Table 15: These are the classes with the most decreasing p-value when the signal with a τ^* mass of 4000 GeV and $\Lambda = 10$ TeV is included.

event class	p^{signal}-value	p^{data}-value	δp [%]
$2\tau + 1\gamma + p_T^{miss} + \mathrm{X}$	0.442	0.443	−0.36
$2\tau + 1\gamma + p_T^{miss} + \mathrm{NJet}$	0.536	0.537	−0.31
$2\tau + 1\gamma + \mathrm{X}$	0.440	0.441	−0.24
$2\tau + 1\gamma + 1\mathrm{Jet} + p_T^{miss}$	0.303	0.304	−0.23
$2\tau + 1\gamma + p_T^{miss}$	0.663	0.664	−0.21
$2\tau + 1\gamma + 1\mathrm{Jet} + p_T^{miss} + \mathrm{X}$	0.468	0.469	−0.19
$1\tau + 2\gamma + p_T^{miss} + \mathrm{X}$	0.273	0.273	−0.17
$2\tau + 1\gamma + 1\mathrm{Jet} + p_T^{miss} + \mathrm{NJet}$	0.581	0.581	−0.16
$1\mu + 1\tau + 1\gamma + p_T^{miss}$	0.131	0.131	−0.12
$2\tau + 1\gamma + 1\mathrm{Jet} + \mathrm{X}$	0.514	0.515	−0.11

Table 16: These are the classes with the most decreasing p-value when the signal with a τ^* mass of 4500 GeV and $\Lambda = 10$ TeV is included.

event class	p^{signal}-value	p^{data}-value	δp [%]
$2\tau + 1\gamma + \mathrm{NJet}$	0.408	0.409	−0.13
$2\tau + 1\gamma + \mathrm{X}$	0.441	0.441	−0.09
$2\tau + 1\gamma$	0.489	0.489	−0.09
$2\tau + 1\gamma + 1\mathrm{Jet}$	0.231	0.231	−0.07
$2\tau + 1\gamma + 1\mathrm{Jet} + \mathrm{NJet}$	0.512	0.512	−0.05
$2\tau + 1\gamma + 1\mathrm{Jet} + \mathrm{X}$	0.514	0.515	−0.04
$2\tau + 1\gamma + p_T^{miss} + \mathrm{X}$	0.443	0.443	−0.02
$2\tau + 1\gamma + p_T^{miss} + \mathrm{NJet}$	0.537	0.537	−0.02
$2\tau + 1\gamma + 1\mathrm{Jet} + p_T^{miss}$	0.304	0.304	−0.01
$2\tau + 1\gamma + p_T^{miss}$	0.664	0.664	−0.01

Table 17: These are the classes with the most decreasing p-value when the signal with a τ^* mass of 5000 GeV and $\Lambda = 10$ TeV is included.

F List of all MC samples

Aggregation group	DAS name	Cross section σ [pb]	k-factor	Order
Drell-Yan	DYJetsToLL_M-10to50_TuneCP5_13TeV-amcatnloFXFX-pythia8	1.861×10^4	1.0	NLO
	DYJetsToLL_M-50_TuneCP5_13TeV-amcatnloFXFX-pythia8	6.104×10^3	0.944	NLO
	DYJetsToLL_LHEFilterPtZ-50To100_MatchEWPDG20_TuneCP5_13TeV-amcatnloFXFX-pythia8	3.617×10^2	1.0	NLO
	DYJetsToLL_LHEFilterPtZ-100To250_MatchEWPDG20_TuneCP5_13TeV-amcatnloFXFX-pythia8	8.497×10^1	1.0	NLO
	DYJetsToLL_LHEFilterPtZ-250To400_MatchEWPDG20_TuneCP5_13TeV-amcatnloFXFX-pythia8	2.906	1.0	NLO
	DYJetsToLL_LHEFilterPtZ-400To650_MatchEWPDG20_TuneCP5_13TeV-amcatnloFXFX-pythia8	4.352×10^{-1}	1.0	NLO
	DYJetsToLL_LHEFilterPtZ-650ToInf_MatchEWPDG20_TuneCP5_13TeV-amcatnloFXFX-pythia8	5.448×10^{-2}	1.0	NLO
	DYToEE_M-120To200_TuneCP5_13TeV-powheg-pythia8	1.932×10^1	1.0	NLO
	DYToEE_M-200To400_TuneCP5_13TeV-powheg-pythia8	2.731	1.0	NLO
	DYToEE_M-400To800_TuneCP5_13TeV-powheg-pythia8	2.410×10^{-1}	1.0	NLO
	DYToEE_M-800To1400_TuneCP5_13TeV-powheg-pythia8	1.900×10^{-2}	1.0	NLO
	DYToEE_M-1400To2300_TuneCP5_13TeV-powheg-pythia8	1.390×10^{-3}	1.0	NLO
	DYToEE_M-2300To3500_TuneCP5_13TeV-powheg-pythia8	8.278×10^{-5}	1.0	NLO
	DYToEE_M-3500To4500_TuneCP5_13TeV-powheg-pythia8	4.135×10^{-6}	1.0	NLO
	DYToEE_M-4500To6000_TuneCP5_13TeV-powheg-pythia8	4.560×10^{-7}	1.0	NLO
	DYToEE_M-6000ToInf_TuneCP5_13TeV-powheg-pythia8	2.066×10^{-8}	1.0	NLO
	ZJetsToNuNu_HT-100To200_TuneCP5_13TeV-madgraphMLM-pythia8	2.805×10^2	1.63	NLO
	ZJetsToNuNu_HT-200To400_TuneCP5_13TeV-madgraphMLM-pythia8	7.836×10^1	1.62	NLO
	ZJetsToNuNu_HT-400To600_TuneCP5_13TeV-madgraphMLM-pythia8	1.094×10^1	1.46	NLO
	ZJetsToNuNu_HT-600To800_TuneCP5_13TeV-madgraphMLM-pythia8	2.559	1.391	NLO
	ZJetsToNuNu_HT-800To1200_TuneCP5_13TeV-madgraphMLM-pythia8	1.179	1.391	NLO
	ZJetsToNuNu_HT-1200To2500_TuneCP5_13TeV-madgraphMLM-pythia8	2.883×10^{-1}	1.391	NLO

Aggregation group	DAS name	Cross section σ [pb]	k-factor	Order
	ZJetsToNuNu_HT-2500ToInf_TuneCP5_13TeV-madgraphMLM-pythia8	6.945×10^{-3}	1.391	NLO
	ZToMuMu_M-120To200_TuneCP5_13TeV-powheg-pythia8	1.932×10^{1}	1.0	NLO
	ZToMuMu_M-200To400_TuneCP5_13TeV-powheg-pythia8	2.731	1.0	NLO
	ZToMuMu_M-400To800_TuneCP5_13TeV-powheg-pythia8	2.410×10^{-1}	1.0	NLO
	ZToMuMu_M-800To1400_TuneCP5_13TeV-powheg-pythia8	1.700×10^{-2}	1.0	NLO
	ZToMuMu_M-1400To2300_TuneCP5_13TeV-powheg-pythia8	1.390×10^{-3}	1.0	NLO
	ZToMuMu_M-2300To3500_TuneCP5_13TeV-powheg-pythia8	8.948×10^{-5}	1.0	NLO
	ZToMuMu_M-3500To4500_TuneCP5_13TeV-powheg-pythia8	4.135×10^{-6}	1.0	NLO
	ZToMuMu_M-4500To6000_TuneCP5_13TeV-powheg-pythia8	4.560×10^{-7}	1.0	NLO
	ZToMuMu_M-6000ToInf_TuneCP5_13TeV-powheg-pythia8	2.066×10^{-8}	1.0	NLO
γ + Jets	GJets_DR-0p4_HT-40To100_TuneCP5_13TeV-madgraphMLM-pythia8	1.575×10^{4}	1.0	LO
	GJets_DR-0p4_HT-100To200_TuneCP5_13TeV-madgraphMLM-pythia8	5.001×10^{3}	1.0	LO
	GJets_DR-0p4_HT-200To400_TuneCP5_13TeV-madgraphMLM-pythia8	1.154×10^{3}	1.0	LO
	GJets_DR-0p4_HT-400To600_TuneCP5_13TeV-madgraphMLM-pythia8	1.272×10^{2}	1.0	LO
	GJets_DR-0p4_HT-600ToInf_TuneCP5_13TeV-madgraphMLM-pythia8	9.346×10^{1}	1.0	LO
Higgs	ggZH_HToBB_ZToNuNu_M-125_TuneCP5_13TeV-powheg-pythia8	1.437×10^{-2}	1.0	NNLO
	ggZH_HToBB_ZToLL_M-125_TuneCP5_13TeV-powheg-pythia8	7.842×10^{-3}	1.0	NNLO
	ggZH_HToBB_ZToQQ_M-125_TuneCP5_13TeV-powheg-pythia8	4.996×10^{-2}	1.0	NNLO
	GluGluHToZZTo4L_M125_TuneCP5_13TeV_powheg2_JHUGenV7011_pythia8	1.212×10^{-2}	1.0	NLO
	ttHTobb_M125_TuneCP5_13TeV-powheg-pythia8	2.953×10^{-1}	1.0	N3LO
	ttHToNonbb_M125_TuneCP5_13TeV-powheg-pythia8	2.118×10^{-1}	1.0	N3LO
	VBF_HToZZTo4L_M125_TuneCP5_13TeV_powheg2_JHUGenV7011_pythia8	9.905×10^{-2}	1.0	NNLO
	VBFHToBB_M-125_TuneCP5_13TeV-powheg-pythia8	2.203	1.0	NNLO
	VBFHToGG_M125_TuneCP5_13TeV-amcatnlo-pythia8	8.585×10^{-3}	1.0	NNLO
	VBFHToTauTau_M125_TuneCP5_13TeV-powheg-pythia8	2.372×10^{-1}	1.0	NNLO
	VBFHToWWTo2L2Nu_M-125_TuneCP5_13TeV-powheg-jhugen727-pythia8	8.579×10^{-2}	1.0	NNLO
	VHToNonbb_M125_TuneCP5_13TeV-amcatnloFXFX_madspin_pythia8	9.425×10^{-1}	1.0	NNLO

Aggregation group	DAS name	Cross section σ [pb]	k-factor	Order
	WminusH_HToBB_WToQQ_M-125_TuneCP5_13TeV-powheg-pythia8	3.675×10^{-1}	1.0	NLO
	WminusH_HToBB_WToLNu_M-125_TuneCP5_13TeV-powheg-pythia8	1.011×10^{-1}	1.0	NNLO
	WplusH_HToBB_WToLNu_M-125_TuneCP5_13TeV-powheg-pythia8	1.593×10^{-1}	1.0	NNLO
	WplusH_HToBB_WToQQ_M-125_TuneCP5_13TeV-powheg-pythia8	5.890×10^{-1}	1.0	NLO
	ZH_HToBB_ZToNuNu_M-125_TuneCP5_13TeV-powheg-pythia8	8.912×10^{-2}	1.0	NNLO
	ZH_HToBB_ZToLL_M-125_TuneCP5_13TeV-powheg-pythia8	4.865×10^{-2}	1.0	NNLO
	ZH_HToBB_ZToQQ_M-125_TuneCP5_13TeV-powheg-pythia8	3.099×10^{-1}	1.0	NNLO
Multi-Boson	DiPhotonJetsBox_M40_80-sherpa	2.993×10^{2}	1.0	LO
	DiPhotonJetsBox_MGG-80toInf_13TeV-sherpa	8.836×10^{1}	1.0	LO
	WGToLNuG_01J_5f_TuneCP5_13TeV-amcatnloFXFX-pythia8	4.120×10^{-2}	1.0	LO
	WGToLNuG_01J_5f_PtG_130_TuneCP5_13TeV-amcatnloFXFX-pythia8	1.031	1.0	NLO
	WGToLNuG_01J_5f_PtG_300_TuneCP5_13TeV-amcatnloFXFX-pythia8	7.110×10^{-3}	1.0	NLO
	WGToLNuG_01J_5f_PtG_500_TuneCP5_13TeV-amcatnloFXFX-pythia8	9.830×10^{-4}	1.0	NLO
	WWG_TuneCP5_13TeV-amcatnlo-pythia8	2.147×10^{-1}	1.0	NLO
	WWTo1L1Nu2Q_4f_TuneCP5_13TeV-amcatnloFXFX-pythia8	4.353×10^{1}	1.149	NNLO
	WWTo2L2Nu_MLL_200To600_TuneCP5_13TeV-powheg-pythia8	1.048×10^{1}	1.162	NNLO
	WWTo2L2Nu_MLL_600To1200_TuneCP5_13TeV-powheg-pythia8	1.048×10^{1}	1.162	NNLO
	WWTo2L2Nu_MLL_1200To2500_TuneCP5_13TeV-powheg-pythia8	1.048×10^{1}	1.162	NNLO
	WWTo4Q_4f_TuneCP5_13TeV-amcatnloFXFX-pythia8	4.531×10^{1}	1.0	NLO
	WWW_4F_TuneCP5_13TeV-amcatnlo-pythia8	2.086×10^{-1}	1.0	NLO
	WWZ_4F_TuneCP5_13TeV-amcatnlo-pythia8	1.651×10^{-1}	1.0	NLO
	WZG_TuneCP5_13TeV-amcatnlo-pythia8	4.123×10^{-2}	1.0	NLO
	WZTo1L1Nu2Q_4f_TuneCP5_13TeV-amcatnloFXFX-pythia8	1.071×10^{1}	1.0	NLO
	WZTo1L3Nu_4f_TuneCP5_13TeV-amcatnloFXFX-pythia8	3.033	1.0	NLO
	WZTo2Q2L_mllmin4p0_TuneCP5_13TeV-amcatnloFXFX-pythia8	5.595	1.0	NLO
	WZTo3LNu_TuneCP5_13TeV-amcatnloFXFX-pythia8	4.430	1.0	NLO
	WZZ_TuneCP5_13TeV-amcatnlo-pythia8	5.565×10^{-2}	1.0	NLO
	ZGTo2NuG_TuneCP5_13TeV-amcatnloFXFX-pythia8	2.804×10^{1}	1.0	NLO
	ZGToLLG_01J_5f_TuneCP5_13TeV-amcatnloFXFX-pythia8	1.238×10^{2}	1.0	NLO
	ZZTo2L2Nu_TuneCP5_13TeV_powheg_pythia8	5.644×10^{-1}	1.0	NLO

Aggregation group	DAS name	Cross section σ [pb]	k-factor	Order
	ZZTo2Q2L_mllmin4p0_TuneCP5_13TeV-amcatnloFXFX-pythia8	3.220	1.0	NLO
	ZZTo4L_TuneCP5_13TeV_powheg_pythia8	1.727	1.0	NLO
	ZZZ_TuneCP5_13TeV-amcatnlo-pythia8	1.398×10^{-2}	1.0	NLO
Multi-Jet	QCD_HT100to200_TuneCP5_PSWeights_13TeV-madgraph-pythia8	2.754×10^{7}	1.0	LO
	QCD_HT200to300_TuneCP5_PSWeights_13TeV-madgraph-pythia8	1.735×10^{6}	1.0	LO
	QCD_HT300to500_TuneCP5_PSWeights_13TeV-madgraph-pythia8	3.668×10^{5}	1.0	LO
	QCD_HT500to700_TuneCP5_PSWeights_13TeV-madgraph-pythia8	2.937×10^{4}	1.0	LO
	QCD_HT700to1000_TuneCP5_PSWeights_13TeV-madgraph-pythia8	6.524×10^{3}	1.0	LO
	QCD_HT1000to1500_TuneCP5_PSWeights_13TeV-madgraph-pythia8	1.064×10^{3}	1.0	LO
	QCD_HT1500to2000_TuneCP5_PSWeights_13TeV-madgraph-pythia8	1.215×10^{2}	1.0	LO
	QCD_HT2000toInf_TuneCP5_PSWeights_13TeV-madgraph-pythia8	2.542×10^{1}	1.0	LO
Single-Top	ST_t-channel_top_4f_InclusiveDecays_TuneCP5_13TeV-powheg-madspin-pythia8	1.360×10^{2}	1.0	NLO
	ST_s-channel_4f_hadronicDecays_TuneCP5_13TeV-amcatnlo-pythia8	7.104	1.0	NLO
	ST_t-channel_antitop_4f_InclusiveDecays_TuneCP5_13TeV-powheg-madspin-pythia8	8.095×10^{1}	1.0	NLO
	ST_s-channel_4f_leptonDecays_TuneCP5_13TeV-amcatnlo-pythia8	3.360	1.0	NLO
	ST_tW_top_5f_NoFullyHadronicDecays_TuneCP5_13TeV-powheg-pythia8	3.809×10^{1}	1.0	NLO
	ST_tW_antitop_5f_NoFullyHadronicDecays_TuneCP5_13TeV-powheg-pythia8	3.251×10^{1}	1.0	NLO
	TGJets_TuneCP5_13TeV-amcatnlo-madspin-pythia8	2.967	1.0	NLO
	tZq_ll_4f_ckm_NLO_TuneCP5_13TeV-amcatnlo-pythia8	7.580×10^{-2}	1.0	NLO
$t\bar{t}$	TT_Mtt-700to1000_TuneCP5_13TeV-powheg-pythia8	7.300×10^{2}	1.139	NNLO
	TT_Mtt-1000toInf_TuneCP5_13TeV-powheg-pythia8	7.300×10^{2}	1.139	NNLO
	TTGG_TuneCP5_13TeV-amcatnlo-pythia8	1.696×10^{-2}	1.0	NLO
	TTGJets_TuneCP5_13TeV-amcatnloFXFX-madspin-pythia8	3.697	1.0	NLO
	TTTo2L2Nu_TuneCP5_13TeV-powheg-pythia8	9.334×10^{1}	1.0	NNLO
	TTToHadronic_TuneCP5_13TeV-powheg-pythia8	3.678×10^{2}	1.0	NNLO
	TTToSemiLeptonic_TuneCP5_13TeV-powheg-pythia8	3.706×10^{2}	1.0	NNLO
	TTTT_TuneCP5_13TeV-amcatnlo-pythia8	9.103×10^{-3}	1.0	NLO

Aggregation group	DAS name	Cross section σ [pb]	k-factor	Order
	TTWJetsToLNu_TuneCP5_13TeV-amcatnloFXFX-madspin-pythia8	2.043×10^{-1}	1.0	NLO
	TTWJetsToQQ_TuneCP5_13TeV-amcatnloFXFX-madspin-pythia8	4.062×10^{-1}	1.0	NLO
	TTWW_TuneCP5_13TeV-madgraph-pythia8	9.103×10^{-3}	1.0	NLO
	TTZToLL_5f_TuneCP5_13TeV-madgraphMLM-pythia8	5.272×10^{-1}	1.0	LO
	TTZToNuNu_TuneCP5_13TeV-amcatnlo-pythia8	1.476×10^{-1}	1.0	NLO
	TTZToQQ_TuneCP5_13TeV-amcatnlo-pythia8	5.297×10^{-1}	1.0	NLO
	TTZZ_TuneCP5_13TeV-madgraph-pythia8	1.386×10^{-3}	1.0	NLO
W + Jets	WJetsToLNu_TuneCP5_13TeV-amcatnloFXFX-pythia8	6.029×10^{4}	1.02	NNLO
	WJetsToLNu_Pt-100To250_MatchEWPDG20_TuneCP5_13TeV-amcatnloFXFX-pythia8	6.778×10^{2}	1.02	NNLO
	WJetsToLNu_Pt-250To400_MatchEWPDG20_TuneCP5_13TeV-amcatnloFXFX-pythia8	2.408×10^{1}	1.02	NNLO
	WJetsToLNu_Pt-400To600_MatchEWPDG20_TuneCP5_13TeV-amcatnloFXFX-pythia8	3.056	1.02	NNLO
	WJetsToLNu_Pt-600ToInf_MatchEWPDG20_TuneCP5_13TeV-amcatnloFXFX-pythia8	4.602×10^{-1}	1.02	NNLO
	WToENu_M-200_TuneCP5_13TeV-pythia8	6.236	1.337	NNLO
	WToENu_M-500_TuneCP5_13TeV-pythia8	2.138×10^{-1}	1.331	NNLO
	WToENu_M-1000_TuneCP5_13TeV-pythia8	1.281×10^{-2}	1.327	NNLO
	WToENu_M-4000_TuneCP5_13TeV-pythia8	3.030×10^{-6}	0.45	NNLO
	WToENu_M-3000_TuneCP5_13TeV-pythia8	2.904×10^{-5}	1.136	NNLO
	WToENu_M-2000_TuneCP5_13TeV-pythia8	5.560×10^{-4}	1.257	NNLO
	WToMuNu_M-200_TuneCP5_13TeV-pythia8	6.236	1.289	NNLO
	WToMuNu_M-500_TuneCP5_13TeV-pythia8	2.138×10^{-1}	1.273	NNLO
	WToMuNu_M-1000_TuneCP5_13TeV-pythia8	1.281×10^{-2}	1.26	NNLO
	WToMuNu_M-2000_TuneCP5_13TeV-pythia8	5.560×10^{-4}	1.173	NNLO
	WToMuNu_M-3000_TuneCP5_13TeV-pythia8	2.904×10^{-5}	1.038	NNLO
	WToMuNu_M-4000_TuneCP5_13TeV-pythia8	3.030×10^{-6}	0.409	LO
	WToTauNu_M-200_TuneCP5_13TeV-pythia8-tauola	6.370	1.0	LO
	WToTauNu_M-500_TuneCP5_13TeV-pythia8-tauola	2.240×10^{-1}	1.0	LO

Aggregation group	DAS name	Cross section σ [pb]	k-factor	Order
	WToTauNu_M-1000_TuneCP5_13TeV-pythia8-tauola	1.370×10^{-2}	1.0	LO
	WToTauNu_M-2000_TuneCP5_13TeV-pythia8-tauola	5.560×10^{-4}	1.0	LO
	WToTauNu_M-3000_TuneCP5_13TeV-pythia8-tauola	3.420×10^{-5}	1.0	LO
	WToTauNu_M-4000_TuneCP5_13TeV-pythia8-tauola	3.030×10^{-6}	1.0	LO
Signals samples				
$\tau^* \to \tau + \gamma$	Taustar_TauG_L10000_m175_CP5_13TeV_pythia8	2.898×10^{-2}	1.0	LO
	Taustar_TauG_L10000_m250_CP5_13TeV_pythia8	2.157×10^{-2}	1.0	LO
	Taustar_TauG_L10000_m375_CP5_13TeV_pythia8	1.557×10^{-2}	1.0	LO
	Taustar_TauG_L10000_m500_CP5_13TeV_pythia8	1.185×10^{-2}	1.0	LO
	Taustar_TauG_L10000_m625_CP5_13TeV_pythia8	9.136×10^{-3}	1.0	LO
	Taustar_TauG_L10000_m750_CP5_13TeV_pythia8	7.068×10^{-3}	1.0	LO
	Taustar_TauG_L10000_m1000_CP5_13TeV_pythia8	4.260×10^{-3}	1.0	LO
	Taustar_TauG_L10000_m1250_CP5_13TeV_pythia8	2.554×10^{-3}	1.0	LO
	Taustar_TauG_L10000_m1500_CP5_13TeV_pythia8	1.529×10^{-3}	1.0	LO
	Taustar_TauG_L10000_m1750_CP5_13TeV_pythia8	9.069×10^{-4}	1.0	LO
	Taustar_TauG_L10000_m2000_CP5_13TeV_pythia8	5.371×10^{-4}	1.0	LO
	Taustar_TauG_L10000_m2500_CP5_13TeV_pythia8	1.869×10^{-4}	1.0	LO
	Taustar_TauG_L10000_m3000_TuneCP5_13TeV_pythia8	1.359×10^{-6}	1.0	LO
	Taustar_TauG_L10000_m3500_TuneCP5_13TeV_pythia8	1.359×10^{-6}	1.0	LO
	Taustar_TauG_L10000_m4000_TuneCP5_13TeV_pythia8	1.359×10^{-6}	1.0	LO
	Taustar_TauG_L10000_m4500_TuneCP5_13TeV_pythia8	1.359×10^{-6}	1.0	LO
	Taustar_TauG_L10000_m5000_TuneCP5_13TeV_pythia8	1.359×10^{-6}	1.0	LO

Table 18: A list of all used MC samples